Design and Construction of a Scintillating Fibre Tracker for measuring Hard Exclusive Reactions at HERMES

Inaugural-Dissertation
zur Erlangung des Doktorgrades der Naturwissenschaften
der Justus-Liebig-Universität Gießen
Fachbereich 07
(Mathematik und Informatik, Physik, Geographie)

vorgelegt von

Matthias Hoek

aus Gießen

II. Physikalisches Institut der Justus-Liebig-Universität Gießen
Juli 2006

Dekan: Prof. Dr. V. Metag

1. Berichterstatter: Prof. Dr. M. Düren
2. Berichterstatter: Prof. Dr. A. Müller

Kenntnisse kann jedermann haben – aber die Kunst zu denken,
ist das seltenste Geschenk der Natur.

Friedrich der Große

Für

Kurt-Jürgen Hoek
und Paul Matern

Zusammenfassung

Im Rahmen dieser Arbeit wird die Planung und der Bau eines Spurrekonstruktionsdetektors aus szintillierenden Fasern (SFT) für den HERMES Recoil-Detektor beschrieben. Dies umfaßt die Festlegung der Entwurfsziele, Entwicklung von Herstellungverfahren, Auswahl der Detektorbestandteile sowie die Durchführung und Auswertung von Komponententests. Abschließend wird eine Einführung in den *Generalised Parton Distribution*-Formalismus (GPD) zur Beschreibung der nicht-perturbativen Nukleonstruktur gegeben. Dieser Formalismus kann auch auf Atomkerne angewendet werden und zu neuen Einsichten in die Kernstruktur und partonische Freiheitsgrade im Kern führen. Anschließend wird die Analyse tiefvirtueller Compton-Streuereignisse an verschiedenen Kernen beschrieben.

Das HERMES-Experiment befindet sich am DESY in Hamburg. Dabei wird der Elektronenstrahl des HERA-Beschleunigers mit einer Energie von 27 GeV verwendet um tief-inelastische Streuereignisse an verschiedenen gasförmigen Targets zu untersuchen. Das HERMES-Experiment bietet dabei die einzigartige Möglichkeit, verschieden Gastargets einzusetzen. Zusätzlich bietet der HERA-Beschleuniger einen longitudinal polarisierten Elektronenstrahl. Der HERA-Beschleuniger bietet ebenfalls die Möglichkeit, einen Positronenstrahl zu erzeugen, der Einfachheit halber wird in dieser Arbeit aber nur von Elektronen gesprochen.

Den idealen Zugang zu den GPDs bietet die tief-virtuelle Compton-Streuung (DVCS). Da das HERMES-Spektrometer in seinem ursprünglichen Aufbau das rückgestreute Nukleon nicht nachweisen kann, wurden bisher indirekte Methoden angewendet, um DVCS-Ereignisse zu separieren. Allerdings lassen sich mit diesen indirekten Methoden nicht alle Untergrundbeiträge eliminieren, insbesondere nicht der Beitrag von Δ-Resonanzen. Um die Untergrundunterdrückung zu verbessern und den gesamten Endzustand exklusiver Reaktionen nachweisen zu können, wurde der HERMES Recoil-Detektor geplant.

Der SFT, als einer der Hauptkomponenten des Recoil-Detektors, dient der Impulsbestimmung für geladene Teilchen im Impulsbereich von $250 - 1400\,\text{MeV/c}$. Außerdem trägt er zur Teilchenidentifikation (PID) von Protonen und geladenen Pionen bei. Bei der Planung des SFT wurde besonderes Augenmerk auf eine geringe Massenbelegung gelegt, um die Ungenauigkeit der Impulsbestimmung durch Mehrfachstreuung der Teilchen zu minimieren. Dies führte zu einer selbsttragenden Konstruktion, wobei besondere Klebstoffe eingesetzt werden müssen, die einerseits die szintillierenden Fasern nicht angreifen und andererseits ausreich-

end Stabilität bieten. Die optische Auslese der Fasern erfolgt mit Sekundär-Elektronen Vervielfachern (SEV), die außerhalb des magnetischen Felds des Recoil-Detektormagneten positioniert werden müssen. Das Szintillationslicht wird mit Hilfe 4 m langer Lichtleiter vom SFT zu den SEVs transportiert. Hierfür wurde eine Steckerverbindung mit hohem Transmissionsgrad entwickelt. Außerdem muß die optische Auslese eine Messung der deponierten Energie im SFT erlauben, um eine Teilchenidentifikation zu ermöglichen. Um die Eigenschaften des gewählten SFT-Designs zu überprüfen, wurde ein Testexperiment an der GSI in Darmstadt durchgeführt. Hierbei wurden vier SFT-Prototypmodule in einem Sekundärstrahl mit variablen Teilchenimpuls getestet. Der Sekundärstrahl bestand hauptsächlich aus geladenen Pionen und Protonen und wurde im Impulsbereich von 300 MeV/c bis 900 MeV/c variiert. Zielsetzung des Testexperiments war die Bestimmung der Nachweiseffizienz der Prototypmodule für geladene Pionen und Protonen, der Energieverlustverteilung dieser Teilchen in den Fasern sowie PID- und Spurrekonstruktionsfähigkeiten. Die Auswertung des Testexperiments ergab, dass alle Entwurfskriterien mit dem gewählten Design erreicht werden konnten. Die modulare Bauweise des SFT wurde zunächst mit Ersatzfasern ausprobiert, um die Machbarkeit zu studieren. Nach erfolgreichem Test, wurde der endgültige SFT zusammengesetzt und in einem weiteren Testexperiment am DESY Hamburg wurde die exakte Positionierung der einzelnen Fasern im SFT bestimmt, wobei lediglich Abweichungen von $150\,\mu m$beobachtet wurden. Diese Ergebnisse bestätigen die hohe Präzision, die mit den entwickelten Konstruktionsmethoden erreicht werden konnte. Abschließend wurde der SFT in den Recoil-Detektoraufbau eingesetzt, wobei ein speziell entwickeltes Werkzeug benutzt wurde, um die korrekte Ausrichtung des SFT zu gewährleisten und Beschädigungen an allen Detektorkomponenten zu vermeiden.

Im letzten Teil dieser Arbeit wird der GPD-Formalismus zur Beschreibung exklusiver Streuprozesse eingeführt und kinematische Variablen, die zur Beschreibung dieser Prozesse notwendig sind. Die GPDs erlauben eine Beschreibung der nicht-perturbativen Nukleonenstruktur und beinhalten Formfaktoren und Partonverteilungsfunktionen (PDF), die auch in inklusiven Streureaktionen zugänglich sind. Allerdings enthalten die GPDs zusätzliche Informationen über die Nukleonenstruktur und so ist z.B. der Zugang zu Informationen über den Bahndrehimpuls von Quarks im Nukleon möglich. Der DVCS-Prozess, bei dem ein virtuelles Photon von einem Quark absorbiert und ein reelles Photon erzeugt wird, spielt eine besondere Rolle bei der Messung von GPDs, da er den theoretisch einfachsten Zugang bietet. Andere exklusive Prozesse, wie z.B. exklusive Mesonproduktion, enthalten weitere nicht-perturbative Elemente, deren Eigenschaften nicht bekannt sind und ebenfalls bestimmt werden müßten. Allerdings ist der Endzustand des DVCS-Prozesses nicht unterscheidbar vom Bethe-Heitler-Prozeß (BH), bei dem das gestreute Elektron durch Bremsstrahlungsprozesse ein reelles Photon erzeugt. Die Ununterscheidbarkeit führt zu quantenmechanischen Interferenzeffekten, die ihrerseits Zugang zu der Amplitude des DVCS-Prozesses bieten. Bei der Messung mit einem longitudinal polarisierten Strahl zeigt sich eine Asymmetrie in der azimuthalen Verteilung des Winkels zwischen der Streuebene des Elektrons und der Produktionsebene des reellen Photons. Die Größe der Asymmetrie ist unter anderem durch die GPDs gegeben.

Der GPD-Formalismus kann auch auf Atomkerne übertragen werden und zu neuen Einsichten in die Kernstruktur und partonische Freiheitsgrade im Kern führen. Allerdings muss bei der Analyse von DVCS-Ereignissen zwischen kohärenten und inkohärenten Prozessen unterschieden werden. Bei kohärenten Prozessen findet die DVCS-Reaktion am gesamten Kern statt und der Kern bleibt intakt, während beim inkohärenten Prozeß die DVCS-Reaktion an einem einzelnen Nukleon stattfindet und der Kern aufgebrochen wird. Im Falle von kohärenten Prozessen gibt es theoretische Modellrechnungen, die eine größere Asymmetrie im Vergleich zum Proton vorhersagen. Da nicht der gesamte Endzustand im HERMES-Spektrometer nachgewiesen werden kann, müssen indirekte Methoden benutzt werden, um die Exklusivität des Ereignisses sicherzustellen. Allerdings kann hierbei nicht zweifelsfrei zwischen kohärenten und inkohärenten Beiträgen unterschieden werden. Einzig eine Beschränkung des Impulsübertrags auf den Kern ermöglicht eine Anreicherung kohärenter Prozesse, wobei ein nicht zu vernachlässigender Anteil inkohärenter Prozesse bleibt.

Zunächst werden aus den vorhandenen Daten verschiedener Targets — H, D, He, N, Ne, Kr und Xe — exklusive DVCS-Prozesse herausgefiltert. Die angewendeten Bedingungen werden detailliert beschrieben und verschiedene Extraktionsmethoden für die Asymmetrie verglichen. Zusätzlich werden systematische Fehlerquellen mit Hilfe von Monte Carlo-Simulationen untersucht und ihr Einfluß auf die Asymmetrie abgeschätzt. Die Asymmetrie wird dann im Hinblick auf den Impulsübertrag auf den Kern untersucht. Die vorhandene Datenmenge erlaubt allerdings nur eine grobe Unterteilung. Im Falle hauptsächlich kohärenter Prozesse — dies entspricht einem kleinen Impulsübertrag — kann zum ersten Mal eine systematische Vergrößerung des Asymmetrie für schwere Kerne (Ne, Kr und Xe) festgestellt werden, die allerdings aufgrund der begrenzten Datenmenge nicht signifikant ist. Für größere Impulsüberträge, bei denen der inkohärente Anteil überwiegt, kann eine solche Veränderung hingegen nicht festgestellt werden. Ein direkter Vergleich mit Ergebnissen am Proton ist jedoch schwierig, da sich die Reaktionskinematik deutlich unterscheidet bzw. der Anteil kohärenter Prozesse vom jeweiligen Target abhängt. Um einen besseren Vergleich zu ermöglichen, müßten Daten bei sehr kleinem Impulsübertrag am Proton gemessen werden. Hierbei kann der HERMES Recoil-Detektor eine entscheidende Rolle spielen, da er einerseits die Akzeptanz des Spektrometers erhöht und andererseits die Auflösung des Impulsübertrags verbessern kann.

Contents

Chapter 1

Introduction

What constitutes the nucleon spin? Although all constituents of the nucleon — quarks and gluons — and their spins are known, the EMC[1] experiment established that only a small fraction of the nucleon's spin can be attributed to the spin of the quarks, a result which became known as the 'spin-crisis'. Other sources like gluons or orbital angular momentum of quarks apparently contribute significantly to the nucleon spin as well. The HERMES experiment was initiated to perform precision measurements of polarised Parton Distribution Functions (PDF) in inclusive and semi-inclusive Deep Inelastic Scattering (DIS), in order to evaluate the contribution of the quark spin to the total nucleon spin. However, the orbital angular momentum is not accessible in inclusive and semi-inclusive DIS measurements.

A possibility to access the orbital angular momentum of quarks inside the nucleon arose with the new theoretical framework of Generalised Parton Distributions (GPD). The GPD formalism was developed for the description of hard exclusive processes and implicitly includes PDFs and Form Factors (FF) — known from inclusive and semi-inclusive measurements — but also embodies additional information, among other things the total angular momentum of partons inside the nucleon. This concept can be applied to nuclei as well, leading to a deeper understanding of the quark and gluon structure of nuclei. The cleanest presently accessible exclusive process to study GPDs is Deeply Virtual Compton Scattering (DVCS), in which a virtual photon interacts with a quark inside a nucleon, which stays intact throughout this process, and produces a real photon. The HERMES experiment is uniquely suited to study DVCS processes on a large variety of targets.

The low momentum recoil nucleon in the final state of the DVCS process is produced at large laboratory angles and escapes detection by the HERMES spectrometer. Nevertheless, DVCS processes were successfully analysed employing indirect methods to establish exclusivity of the data sample. However, background contributions to the exclusive sample due to semi-inclusive DIS and intermediate Δ-resonances are difficult to identify by these indirect methods. Reconstruction of the complete final state would enable the suppression of these background con-

---

[1] European Muon Collaboration

tributions. Therefore, a dedicated Recoil Detector, surrounding the target area, was proposed. Detection of recoiling protons as well as basic Particle Identification (PID) capabilities to distinguish protons and charged pions are essential for this task. The Scintillating Fibre Tracker (SFT) is one of the main components of the HERMES Recoil Detector. It provides not only tracking informations for momentum determination but also PID by measuring the energy loss of traversing particles.

This thesis describes design and construction of the SFT. The first section gives a comprehensive overview of the experimental set-up of HERMES and its components relevant for DVCS analysis. The second section introduces the Recoil Detector and Monte Carlo (MC) studies performed to evaluate the requirements for the individual detector parts. In the third section a detailed description of the design parameters and constraints is given and the chosen materials and assembling methods are discussed. This section is complemented by reporting results of the performance of SFT prototype modules from a test experiment conducted at GSI[2]. Finally, an introduction into the GPD formalism and its application to nuclei is given in the fourth section and pioneering results of DVCS off nuclei are presented in the fifth section.

---

[2] Gesellschaft für SchwerIonenforschung

Chapter 2

The HERMES Experiment

HERMES[1] is one of the four experiments at the HERA[2] electron proton collider at DESY[3]. It uses the longitudinally polarised electron/positron beam of HERA which has an energy of $27.5\,\text{GeV}$, together with polarised and unpolarised gas targets internal to the storage ring. The HERA beam switches between electrons/positrons and although most of the HERMES data has been taken with positrons, electrons are referred to here for expedience. Scattered electrons and particles produced in deep-inelastic electron-nucleon interactions are detected and identified by a forward spectrometer with large momentum and solid angle acceptance. The HERMES experiment was commissioned in early summer 1995. The first phase of HERMES data taking covers the years 1995 to 2000. After a luminosity upgrade of HERA, the second phase of HERMES data taking started in 2002 and will continue until 2007.

2.1 The Polarised Electron Beam at HERA

A schematic drawing of HERA is shown in fig. 2.1, indicating the four experiments with HERMES being located at the eastern experimental area. The HERA electron beam consists of individual bunches, separated by $96\,\text{ns}$. The average beam current at injection is up to $50\,\text{mA}$. The beam current decreases exponentially due to interactions with residual gas, yielding a beam life time of about 10 hours.

In high-energy storage rings, electron beams can become transversely polarised through the emission of spin-flip synchrotron radiation in the arcs due to the Sokolov-Ternov mechanism [1]. This process involves an asymmetry in spin-flip amplitudes, which enhances the population of the spin state anti-parallel to the transverse magnetic bending field. This polarisation develops over time according to

$$P(t) = P_\infty \left(1 - e^{-t/\tau}\right), \tag{2.1}$$

---

[1] **HER**A **Me**asurement of **S**pin

[2] **H**adron **E**lectron **R**ing **A**cclerator

[3] **D**eutsches **E**lektronen **SY**nchrotron

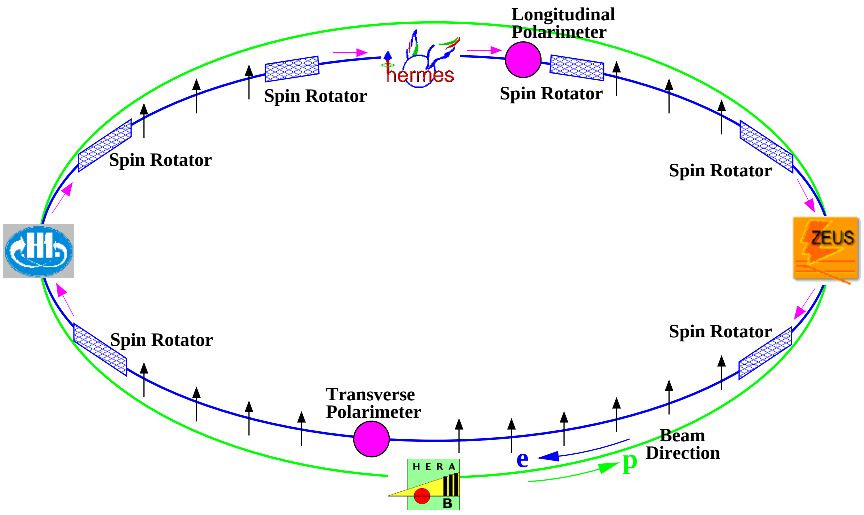

Figure 2.1: *Schematic drawing of the HERA accelerator at DESY indicating the four experimental areas. The positions of the spin rotators for the electron beam is shown as well as the positions of both transverse and longitudinal polarimeters. The arrows denote the direction of the electron beam polarisation.*

where the asymptotic polarisation P_∞ and the time constant τ are characteristics of the storage ring. Depolarising effects can substantially reduce the maximum achievable polarisation. Routinely a polarisation of 40 – 60% was achieved in the first running period [2]. Precise alignment of the machine quadrupoles and fine tuning of the orbit parameters are mandatory to achieve high polarisation. As this is difficult to control, continuous monitoring of the beam polarisation is necessary. Longitudinal beam polarisation is required for high-energy polarised electron scattering experiments since, for a transversely polarised beam, all spin effects are suppressed by m_e/E, where m_e is the electron mass and E is the electron energy. A longitudinal polarisation is obtained by a pair of spin rotators located upstream and downstream of the HERMES experiment in the HERA east straight section. Not only the HERMES experiment employs spin rotators but both collider experiments H1 and ZEUS are now also using spin rotators. The first rotator aligns the spins parallel to the beam direction and the second one rotates them back to the vertical direction before the beam enters the next arc of the storage ring since only a transverse polarisation of the beam is conserved in the arcs. The sign of the beam polarisation can be reversed by inverting fields in the spin rotators and moving the magnets of the spin rotators. The polarisation direction is typically changed every few months to minimise systematic effects in the analysis of beam spin asymmetries. The polarisation of the electron beam is continuously monitored by two polarimeters [3, 4] which use the spin dependent cross section for Compton scattering of circularly polarised laser photons on a polarised electron beam. Transverse polarisation leads to a small up-down spatial asymmetry [2] of the back-scattered electrons with respect to the orbital plane for the two helicity states of the laser beam which is measured by the Transverse POLarimeter (TPOL) in the HERA West section. Longitudinal beam polarisation modifies the energy dependence of the cross section. The corresponding asymmetry in energy deposition of the back-scattered photons for the two helicity states of the laser is measured with the Longitudinal POLarimeter (LPOL) in the HERA east section, downstream of the HERMES experiment. Both polarimeters allow separately the measurement of the polarisation of individual bunches, which is used during beam injection and acceleration for optimisation of beam orbit parameters necessary to achieve high polarisation values. For the later analysis purposes the mean polarisation is used instead.

2.2 The HERMES Spectrometer

A schematic overview of the HERMES spectrometer is shown in fig. 2.2. It is a forward open geometry spectrometer with a dipole magnet surrounding the electron and proton beam pipes, providing an integrated field of 1.3 Tm [5]. Field clamps in front and behind the magnet reduce the fringe field at the position of the drift chambers next to the magnet to below 0.1 T. The magnet gap is divided by a horizontal septum plate shielding both beams from the magnetic field. Consequently, the spectrometer consists of two identical halves mounted above and below the beam pipes. Both beams go through the spectrometer, separated by 72 cm. The coordinate system used by HERMES has the z axis along the beam momentum, the y axis vertically upwards and the x axis horizontal, pointing outwards.

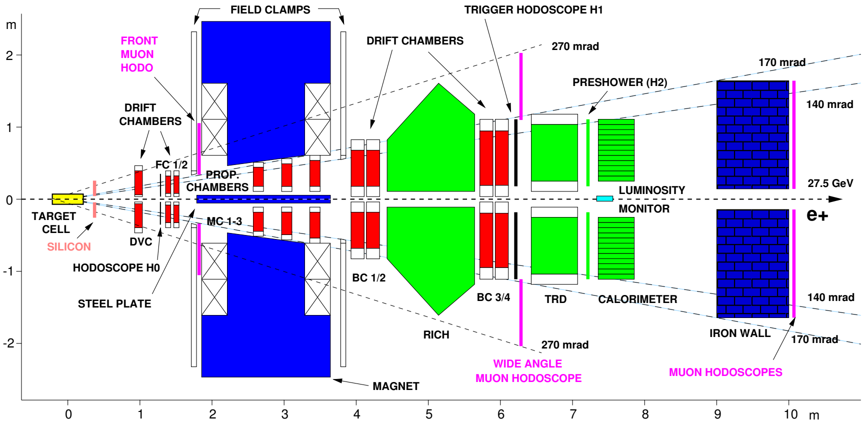

Figure 2.2: *Schematic drawing of the HERMES spectrometer as in 2000 without the Recoil Detector. The tracking system (DVC, FC, MC, BC) is shown in red, the PID detectors (RICH, TRD, Calo) in green. The electron beam enters the spectrometer from the left, first traversing the target cell (yellow) and continuing along the symmetry axis of the top and bottom half of the spectrometer defining the z-axis of the* HERMES *coordinate system. Furthermore, the acceptance of the spectrometer and the back tracking system in the vertical direction is indicated which is the y-axis in* HERMES *coordinates. Finally, the x-axis of the* HERMES *coordinate system points into the plane.*

Particles with scattering angles within $\pm\ 170$ mrad in the horizontal direction and between 40 mrad $< |\theta_y| < 140$ mrad in the vertical direction are accepted by the spectrometer.

In the following section, the spectrometer components important for the analysis of Deeply-Virtual Compton Scattering (DVCS) events are described in detail. A comprehensive overview of all detector components is given in [5].

2.2.1 Target

HERMES uses a gas target internal to the storage ring. Gaseous targets offer the advantage of undiluted targets materials while maintaining upper limits on the target density imposed by the operation of the accelerator. The gas enters a thin-walled cryogenically-cooled storage cell consisting of an open-ended elliptical tube made of ultra-pure aluminium with a uniform wall thickness of $75\ \mu m$ and a length of 400 mm. Compared to a free atomic beam the target density in a storage cell is increased by two orders of magnitude to values of about 1–2$\cdot 10^{14}$ nucleons/cm^2 for H [5]. The gas atoms leak out of the open ends of the cell and are pumped away by a high speed differential pumping system. A set of movable and fixed collimators is used to protect the target cell and the spectrometer from synchroton radiation.

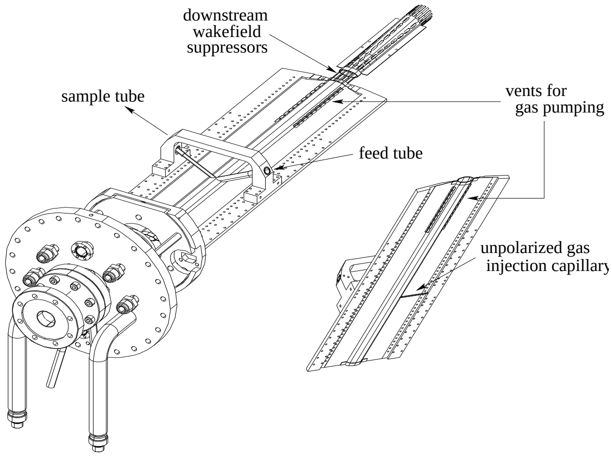

Figure 2.3: The HERMES *storage cell for polarised targets and its support flange.*

Until 2005, the target could be operated in two modes — either injecting polarised hydrogen/deuterium or a variety of unpolarised gaseous targets like H, D, He, N, Ne, Kr and Xe. For the final data taking period the polarised target, consisting of an Atomic Beam Source (ABS), a Breit-Rabi Polarimeter (BRP), a Target Gas Analyser (TGA) and a superconducting magnet to generate the holding field, was removed to install the Recoil Detector. The ABS [6] supplied the target cell with polarised hydrogen or deuterium atoms, while the BRP [7] measured the atomic polarisation of the gas sampled from the cell. The TGA [8] measured the degree of dissociation of the target gas with a quadrupole mass spectrometer. Until 2000 a longitudinal target polarisation was maintained which then was changed to a transversely one. For unpolarised operation the target gas was inserted into the storage cell by the Unpolarised Gas Feed System (UGFS). Typical target densities of 10^{15} - 10^{17} nucleons/cm^2 can be achieved with the UGFS, restricted ultimately by the deadtime of the HERMES Data AcQuisition (DAQ), increasing background due to Møller-electrons in the HERMES front region and beam instabilities at very low life times ($\tau < 1\,\mathrm{h}$). Only unpolarised gaseous targets were used for the analysis of nuclear DVCS events.

2.2.2 Tracking System

The tracking system serves several functions covering vertex reconstruction, measuring scattering angles and particle momentum from track deflection and identifying hits in the Particle IDentification (PID) detectors associated with each track. Determining the event vertex ensures that reconstructed events stem from the sub-mm beam envelope and from a region inside the target cell. The momentum resolution for electrons is limited by Bremsstrahlung in the material of the target cell and beam pipe exit window [5]. Also the resolution in scattering angle, necessary for kinematic reconstruction of an event, is limited by multiple scattering in this material.

The HERMES tracking system consists of drift chambers in front of and behind the spectrometer magnet and proportional chambers mounted inside the magnet opening. A Drift Vertex Chamber (DVC) and two Front Chambers (FC) in front of the spectrometer magnet determine the initial particle track. The Magnet Chambers (MC) within the opening of the magnet are used for reconstruction of particle with low momentum that are deflected out of the spectrometer acceptance. Four drift Back Chambers (BC) provide track reconstruction after deflection of a particle in the magnetic field. All tracking detectors feature the same principle layout with wires oriented either vertically (x-plane) or tilted by ± 30° (u- and v-plane) to determine a space point of the particle track. Each drift chamber is made of six layers of drift cells in three coordinate doublets (uu', xx' and yy'). Each layer consists of a plane of alternating anode and cathode wires between a pair of cathode foils. Two consecutive planes of similar wire orientation are staggered by half the cell size in order to help resolve left-right ambiguities. All drift chambers are operated with an Ar(90%)/CO_2(5%)/CF_4(5%) gas mixture which facilitates a high drift velocity and is non-flammable. The readout of the drift chambers is accomplished by Amplifier-Shaper-Discriminator (ASD) cards connected to FastBus Multihit Time-to-Digital Converters (TDC) with a time resolution of $0.5\,\mathrm{ns}$. The spatial resolution per plane is in the order of $200 - 300\,\mu m$ [5].

Since the MCs have to be operated in a strong magnetic field, Multi-Wire Proportional Chambers (MWPC) were chosen for this purpose. The wire geometry is similar to the drift chambers with each MC consisting of three layers of wire planes (u, x and v). The drift chamber gas mixture was optimised for MWPC operation containing Ar(65%)/CO_2(30%)/CF_4(5%). The MCs provide a spatial resolution of about $700\,\mu m$.

Alignment of all tracking detectors is achieved by special alignment runs in which the magnet is switched off and the straight particle tracks are used to align front and back chambers with respect to each other. An efficient reconstruction code (HRC) using a tree-search algorithm is employed to allow for a very quick determination of particle tracks from a given set of detector hits [9], which is possible due to the similar layout of each drift chamber. Afterwards each track is reconstructed under the assumption that front- and back-partial track have to form a continuous curve (forced-bridging). The momentum of a particle is then calculated from its deflection in the magnetic field, which provides also the particle charge, determined by HRC using a lookup-table. The achieved momentum resolution was between 0.7 and 1.25% over the entire kinematic range of the experiment [5] before the installation of the Ring-Imaging Čerenkov (RICH) counter in the beginning of 1998 and is between 1.5 and 2.5% since then [10]. The uncertainty in the scattering angle is smaller than 0.6 mrad.

2.2.3 Particle Identification Detectors

PID capability is important in the analysis of Deep-Inelastic Scattering (DIS) measurements. The HERMES PID system provides an excellent hadron-lepton separation with a pion rejection factor better than 100 while maintaining a lepton detection efficiency better than 99%. This is accomplished by using different detector types: a RICH counter, a Transition-Radiation Detector (TRD) and an electromagnetic calorimeter combined with a preshower detector (see fig. 2.2).

The RICH — designed for the separation of pions, protons and kaons — contributes to the hadron-lepton separation only for particles with energies below 4 GeV. Since the analysis of DVCS events deals only with particles of higher energies, the RICH is not used. For a detailed description of the RICH, see [11].

The TRD utilises the fact that transition radiation is produced when a relativistic particle traverses the boundary between materials with different dielectric coefficients [12]. The intensity of transition radiation is roughly proportional to the particle energy, thus facilitating PID at highly relativistic energies. The angular distribution of transition radiation peaks in the forward direction with a sharp maximum at $1/\gamma$, where γ is the Lorentz factor. Thus, transition radiation is well collimated along the direction of the radiating particle. The TRD consists of six consecutive modules, each containing a radiator with plastic fibres of about $20\,\mu m$ diameter as radiator material and a Xe(90%)/CH_4(10%) filled proportional chamber with vertical wires separated by 1.27 cm. Both electrons and hadrons deposit energy in the detector due to ionisation, but only electrons produce transition radiation in the kinematic regime of HERMES. Electrons deposit therefore approximately twice the amount of energy compared to pions [5]. Combining the information from several modules and using the truncated mean method, one obtains an average pion rejection factor of about 150 for 90% electron efficiency.

The preshower detector, which is mounted directly in front of the calorimeter, consists of the hodoscope H2 preceded by a 11 mm-thick lead shield (see fig. 2.4) corresponding to two radiation lengths. The lead shield causes the majority of leptons and photons to produce electromagnetic showers before entering the calorimeter. The hodoscope is made of 42 vertical 1 cm-thick scintillator paddles that are staggered with an overlap of 2 – 3 mm to avoid insensitive areas. Each paddle is optically coupled via light guides to a Photo-Multiplier Tube (PMT) at the outside of the detector. Hadron-lepton separation is based on the fact that hadrons mostly lose energy by ionisation whereas leptons start electromagnetic showers. The preshower detector, aside from the calorimeter, is the only detector capable of detecting photons which are crucial for DVCS analysis. However, it does not provide a measurement of the photon energy nor its position that is suitable for analysis purposes. The small amount of energy deposited by electromagnetic showers started in the lead shield is used to separate photon and electron induced showers in the calorimeter.

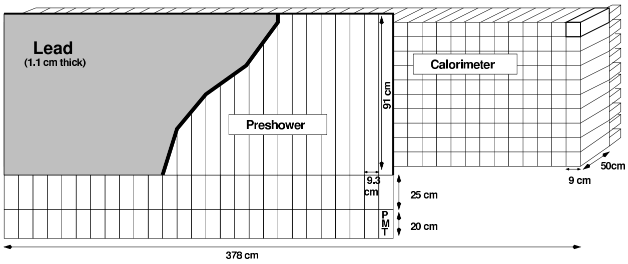

Figure 2.4: Schematic drawing of the lower half of the calorimeter and preshower detectors. The preshower detector is preceded by a $1.1\,cm$ *thick lead shield causing electrons and photons to start electromagnetic showers. The calorimeter consists of lead-glass blocks with a front area of* $9{\times}9\,cm^2$ *and a length of* $50\,cm$ *corresponding to about 50 radiation lengths* X_0.

The electromagnetic calorimeter provides a first level trigger for scattered electrons, based on energy deposition, and aids in PID. As it is the only detector of the HERMES spectrometer able to measure the position and energy of photons it is of great importance for DVCS analysis. Radiation resistant lead-glass[4] blocks with a front area of $9{\times}9\,\text{cm}^2$ and a length of $50\,\text{cm}$, corresponding to about 50 radiation lengths X_0, are stacked in two $42{\times}10$ arrays [13] (see fig. 2.4) above and below the beam. Each block is wrapped with aluminised mylar foil and coupled to a PMT by a silicone glue. The energy response to electrons is linear within 1% over the energy range $1 - 30\,\text{GeV}$ [14] and can be parametrised as

$$\frac{\sigma(E)}{E} = \frac{(5.1 \pm 1.1)\,10^{-2}}{\sqrt{E(GeV)}} + (1.5 \pm 0.5)\,10^{-2}. \tag{2.2}$$

---

[4] Lytcarino F101

Summing up the signal in the hit block and the eight surrounding ones, more than 99% of the electromagnetic shower is contained in this 3×3 array (also called a cluster). The energy contained in a cluster is almost independent of variations of the impact point or of the angle of incidence of the lepton. In order to relate a cluster from a charged particle to its corresponding track, a hit position is determined from the energy distribution inside a cluster. The centroid is calculated as the energy-weighted average position employing a logarithmic energy weight [15]. The obtained spatial resolution of the impact point is about $0.7\,\mathrm{cm}$. Although the spatial resolution of the calorimeter is not too important for charged particles since it is only needed to match the track to its respective cluster, it is of utmost importance to the photon reconstruction as it is the only available position information. The quality of the energy reconstruction for leptons can be checked using the momentum p derived from the tracking system. The ratio E/p has a central value of 1 for electrons since the electromagnetic shower is completely contained within the calorimeter and the electron mass can be neglected in this energy regime. There is no separate energy calibration for leptons and photons, i.e. it is assumed that the shower development is similar (which is at least true for photons converting in the preshower detector into lepton pairs). Photons not converted in the preshower detector exhibit a different behaviour leading to an overestimated photon energy [10].

The responses of the four PID detectors are combined to provide good hadron rejection. Using a probability based approach, the quantity PID_3 defined as

$$\mathrm{PID}_3 = \log_{10}\left(\frac{P^e_{Cal}P^e_{Pre}P^e_{RICH}}{P^h_{Cal}P^h_{Pre}P^h_{RICH}}\right), \tag{2.3}$$

where P^i_j is the probability that a particle of type *i* produced a given response in detector *j*. The P^i_j are determined by comparing the detector responses for each track to a typical response function for each detector. Such functions are referred to as parent distributions [5]. Combining PID_3 with the TRD response yields are very good hadron-lepton separation (see fig. 2.5) with a clean lepton sample at positive PID_3 values and large TRD signals.

2.2.4 Trigger System

The function of the trigger system is to distinguish interesting events from background with high efficiency, and initiate digitisation and readout of the detector signals. While a variety of triggers exist for different physics studies, only the DIS trigger (trigger-21) is of importance for the DVCS analysis. The DIS trigger selects positron events by requiring hits in the three scintillator hodoscopes, H0, H1 and H2, together with sufficient energy deposited in two adjacent columns of the calorimeter in coincidence with the accelerator bunch signal. The hodoscope H0 is located in the front region of the spectrometer and consists of only one scintillator paddle in each detector half, read out by two PMTs. H1 is placed directly in front

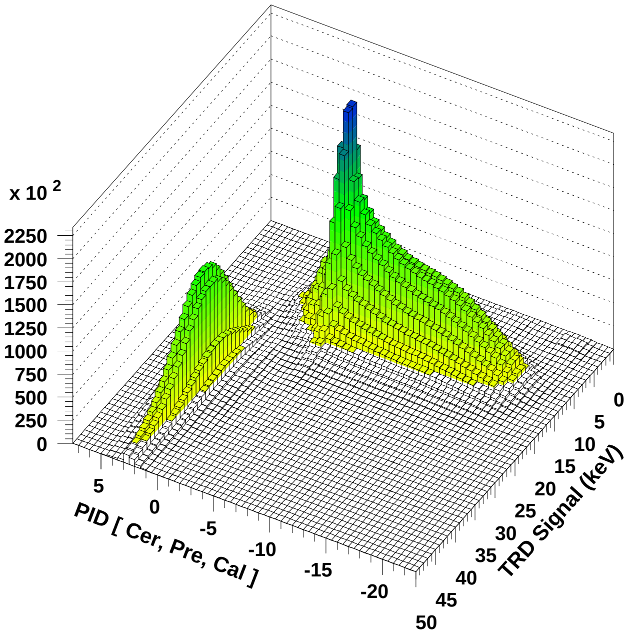

Figure 2.5: *Hadron and lepton separation achieved with* HERMES *PID detectors. Positrons appear at positive* PID_3 *and large TRD signal values.*

of the TRD in the back region of the spectrometer. Its setup is similar to the hodoscope H2 as described previously in sec. 2.2.3. The timing between H0 and H2 is used to reject backward-going particles from the HERA proton beam [5]. The hodoscope thresholds were set below the signal height of Minimum Ionising Particles (MIP). A calorimeter threshold of 3.5 GeV suppresses the charged hadronic background while maintaining a high efficiency for electromagnetic showers. Given the above mentioned conditions, two thirds of the DIS triggers had tracks, 95% of reconstructed tracks came from the target, and one third had accompanying positrons [5].

Chapter 3

The HERMES Recoil Detector

Improving the study of hard exclusive processes, especially DVCS, at HERMES requires a novel detector surrounding the internal gas target. In its original setup only the scattered electron and a real photon are detected by the HERMES spectrometer. A missing mass technique is then employed to extract the sample of exclusive events. But the limited missing mass resolution of the spectrometer is not sufficient to identify non-exclusive events where an intermediate Δ-resonance was created. This type of background contributes to about 10% [16] to the exclusive sample and thus constitutes the main source of background.

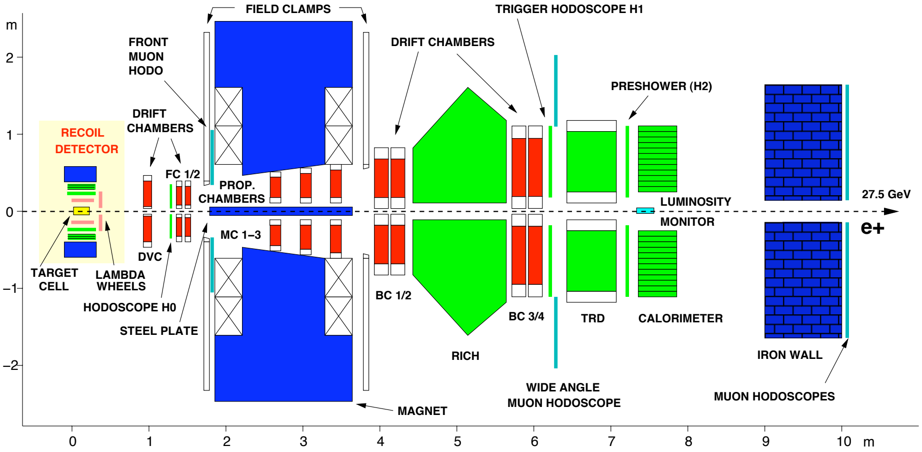

Figure 3.1: *Schematic drawing of the* HERMES *spectrometer indicating the position of the Recoil Detector surrounding the target cell. The electron beam enters the spectrometer from the left.*

The HERMES Recoil Detector [17] was proposed to enhance the acceptance of the main spectrometer in the target region (see fig. 3.1) and detect recoiling target nucleons. The direct measurement of recoiling nucleons will then allow to distinguish exclusive events from the non-exclusive background.

Combining the currently used missing mass technique to remove higher resonances and more sophisticated methods like a coplanarity cut available due to reconstruction of the complete final state by the Recoil Detector will result in a much cleaner sample of exclusive events. A coplanarity cut exploits the fact that the momentum vector of the recoiling nucleon has to coincide with the scattering plane of the electron. Monte Carlo (MC) simulations were used to study the suppression of non-exclusive background events (see fig. 3.2) when employing such a coplanarity cut in addition. These MC studies were used to determine the requirements for the Recoil Detector to reduce the fraction of non-exclusive events to about 1% [17].

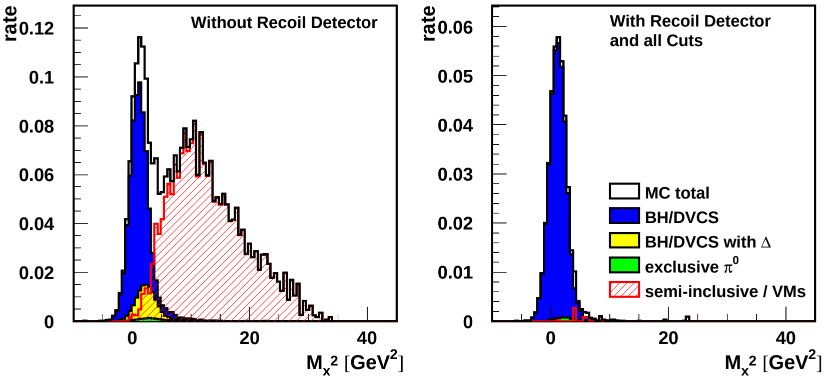

Figure 3.2: *Improved exclusive event selection due to the Recoil Detector according to Monte Carlo studies. The left panel shows the missing mass spectrum with exclusive and semi-inclusive contributions for the* HERMES *spectrometer only. The different background contributions leaking into the exclusive region are indicated. The right panel shows the same missing mass spectrum but using simulated information from the Recoil Detector to suppress non-exclusive events. Note, that imposing all relevant cuts for the Recoil Detector reduces also the numbers of events in the exclusive region.*

3.1 Requirements for the Recoil Detector

The design requirements for the Recoil Detector are defined by the kinematics and the nature of particles involved in the exclusive reactions as well as by the expected background processes. To achieve the anticipated reduction of the non-exclusive background fraction due to intermediate Δ-resonances to below 1%, a rejection of 90% of these events is required. Δ^+-resonances decay either into $p\pi^\circ$ or $n\pi^+$. Hence the Recoil Detector is expected to detect protons, charged pions and photons from π°-decay.

A feature shared by all of the exclusive physics processes of interest is the production of a low momentum recoil proton at large laboratory angles. The distributions of recoil protons for DVCS events and exclusive ρ°-production in terms of momentum p and polar angle θ are shown in fig. 3.3 in comparison with the distribution for protons from Δ-decays.

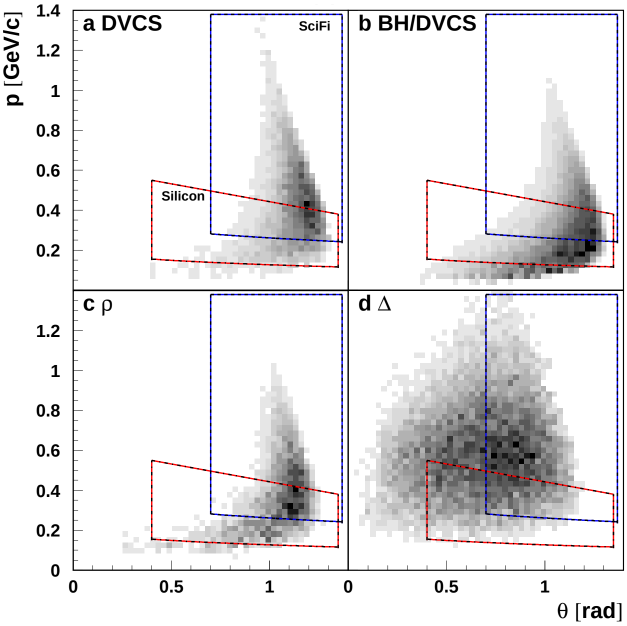

Figure 3.3: *Distribution of recoil proton momentum versus polar angle with respect to beam for exclusive physics processes of interest (a-c) and main non-exclusive background channel (d). The anticipated acceptance of the Recoil Detector are indicated for the Silicon Strip Detector (red) and Scintillating Fibre Tracker (blue).*

The desired coverage of the Recoil Detector is $0.1 - 1.35$ rad in polar angle and up to 1.4 GeV/c in momentum. The low-momentum threshold should be as low as possible and the coverage in azimuthal angle ϕ should be as close to 2π as possible. Charged pions from Δ-decays can be mistaken for a recoiling proton, in particular as the accompanying neutron escapes undetected. The expected distribution in momentum and polar angle of such pions is shown in fig. 3.4 a. The momentum distribution is similar to the one for recoil protons from exclusive processes (see fig. 3.4 b) thus requiring, in addition, Particle IDentification (PID) capabilities for the Recoil Detector below 800 MeV/c to distinguish π^+ from protons.

As pointed out previously, the Recoil Detector must also be able to detect photons from the decay of neutral pions to reject intermediate Δ-resonances. Although the coplanarity cut removes most of this background [17], additional photon detection is mandatory to achieve the envisaged background suppression referred to above.

For a coplanarity cut to be effective, the resolution of transverse momentum of the recoiling nucleon

$$t = (q - q')^2 = (p - p')^2 \quad , \tag{3.1}$$

with q (q') being the momentum of the initial (scattered) electron and p (p') of the initial (recoiling) nucleon, is required to be better than 10% below 500 MeV/c and

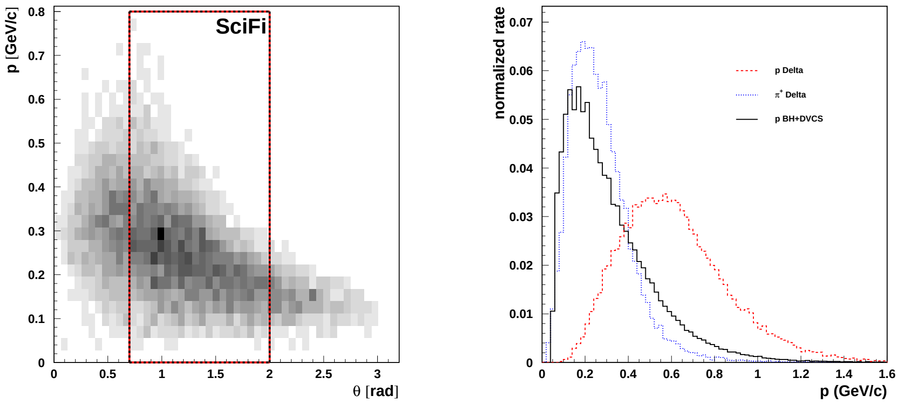

(a) (b)

Figure 3.4: *Momentum distributions for recoiling proton and charged pions:*
(a) Distribution of momentum versus polar angle for π^+ *from* Δ*-decays.*
(b) Projection of momentum distributions for recoiling protons and π^+ *and protons resulting from* Δ*-decays.*

5% for higher momenta. This can be translated into a resolution in terms of the azimuthal angle ϕ requiring a precision of 0.1 rad below 500 MeV/c and 0.05 rad above. The missing mass resolution can not be enhanced by the Recoil Detector as all momenta of the particles detected in the forward spectrometer are much larger than those of the recoiling nucleons. However, a good momentum resolution allows to enhance the resolution of the momentum transfer t as it can be determined from the kinematics of the recoiling nucleon instead of the scattered electron. Currently, the resolution is not sufficient to measure a t-dependence for DVCS events, t being an important parameter of theoretical predictions, especially in the limit $t \longrightarrow 0$, see chap. 5. All requirements for the Recoil Detector in terms of acceptance, resolution and PID are summarised in tab. 3.1.

3.2 Recoil Detector Set-up

The Recoil Detector set-up was optimised to fulfil the specifications listed in tab. 3.1. An overview of the general set-up is shown in fig. 3.5 showing the target cell surrounded by the Silicon Strip Detector (SSD) inside the beam vacuum and continuing outside the scattering chamber with the Scintillating Fibre Tracker (SFT) and the Photon Detector (PD). The Recoil Detector is then surrounded by a superconducting solenoidal magnet with a longitudinal field of 1 T.

A brief overview of the passive detector parts such as target cell, scattering chamber and magnet, as well as a description of the active detector parts will be given in the following section.

Table 3.1: *Overview of ideal and expected detector performance for Silicon Strip Detector (SSD) and Scintillating Fibre Tracker (SFT) according to Monte Carlo simulation [17].*

Parameter	Ideal Performance	Expected Performance
p-acceptance	50 – 1400 MeV/c	135 – 450 MeV/c SSD 250 – 1400 MeV/c SFT
θ-acceptance	0.1 – 1.35 rad	0.4 – 1.35 rad SSD 0.7 – 1.35 rad SFT
ϕ-acceptance	2π	4.8 rad SSD $>$ 4.8 rad SFT
p-resolution	<10% for p <500 MeV/c 5% for p >500 MeV/c	3 – 9% for p <500 MeV/c 13% for p >500 MeV/c
t-resolution	<0.07 GeV^2	0.01 – 0.07 GeV^2 for $t < 0.3$ 0.07 – 0.2 GeV^2 for $0.3 < t < 1.0$
ϕ-resolution	<0.05 rad	0.031 rad SSD 0.008 rad SFT
π/p PID range	50 – 800 MeV/c	135 – 650 MeV/c
π^+ rejection factor	>10	>10 for p <650 MeV/c
Δ suppression	>90%	92%

3.2.1 Passive Recoil Detector Parts

The target cell is located in the centre of the scattering chamber. The target cell consists of a thin aluminium tube with elliptical cross section and a holding structure with cooling circuits. Unpolarised gas is injected into the tube through a small capillary. The target cell thickness has to be the minimum possible as it determines the lower momentum cut-off for recoiling target nucleons. Currently the aluminium tube has a thickness of $75\,\mu m$ corresponding to a lower momentum cut-off of 135 MeV/c for protons.

The scattering chamber is part of the vacuum system of the electron beam line and therefore has to be high-vacuum compatible. On the other hand its contribution to multiple scattering should be kept to a minimum. The scattering chamber consists of two sections. The downstream part surrounding the target cell is made of aluminium with a wall thickness of 1.2 mm, governed only by mechanical constraints. In contrary, the upstream part, where due to kinematics no recoiling nucleons are expected, is a stainless steel service chamber with feedthroughs for electronic and cooling connections for the SSD and the target cell. The two sections are connected by a collar flange with a diameter of 215.5 mm which in turn determines the minimum inner diameter of the SFT. Integrated into the scattering chamber are two collimators protecting the target cell and the SSD from synchrotron radiation.

The whole set-up will be surrounded by a superconducting magnet. The magnetic field serves different purposes. The magnetic field protects the SSD from elas-

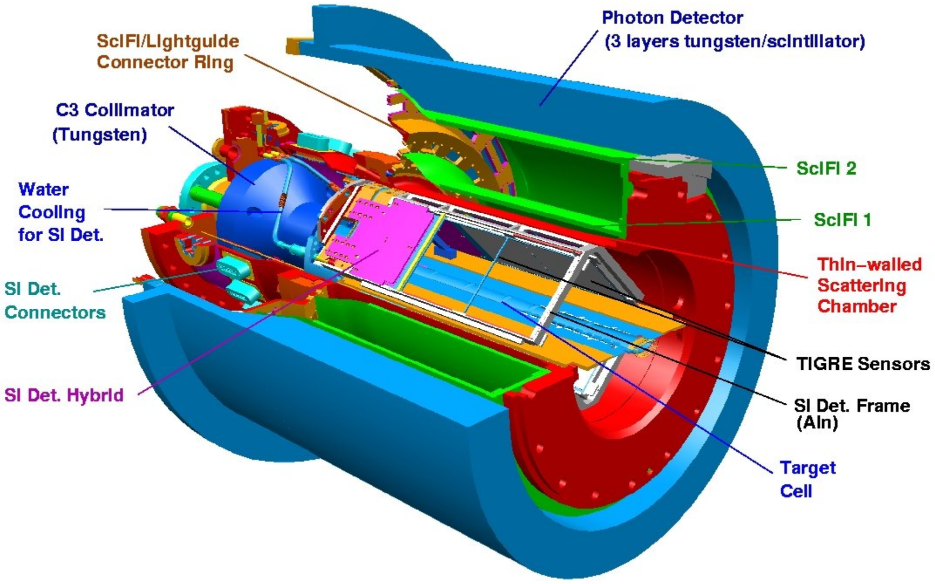

Figure 3.5: *Schematic drawing of the Recoil Detector and support structures. The Silicon Strip Detector (SSD) surrounding the target cell is located within the beam vacuum inside the scattering chamber. Continuing outwards are the two concentric barrels of the Scintillating Fibre Tracker (SFT) and finally the Photon Detector (PD). The surrounding superconducting magnet is not shown. The electron beam enters from the left side, where an additional collimator (C3) protects the Recoil Detector from synchrotron radiation.*

tically scattered electrons (Møller electrons). Secondly, the longitudinal magnetic field causes a deflection of charged particles necessary for the SFT to determine the momentum of the particles. To achieve the envisaged momentum resolution given in tab. 3.1 with the SFT, a magnetic field strength of 1 T is necessary. The homogeneity of the magnetic field has to be better than 20% according to MC tracking studies [17].

3.2.2 Silicon Strip Detector

The SSD is located inside the scattering chamber within the beam vacuum in order to detect low momentum recoil protons that would otherwise be stopped inside the scattering chamber. Momentum determination for low momenta particles is performed using the $\Delta E/E$ technique [18]. The diamond-shaped configuration of the SSD surrounding the target cell is shown in fig. 3.6. Each face of the SSD consists of two layers of double-sided TIGRE detectors[1] of 300 μm thickness covering an active area of 99×99 mm^2. The TIGRE detectors feature 128 channels on each

---

[1] MICRON Semiconductors Ltd.

side with a strip pitch of 758 μm. Strips on either side are perpendicularly oriented to each other thus providing space point reconstruction ability.

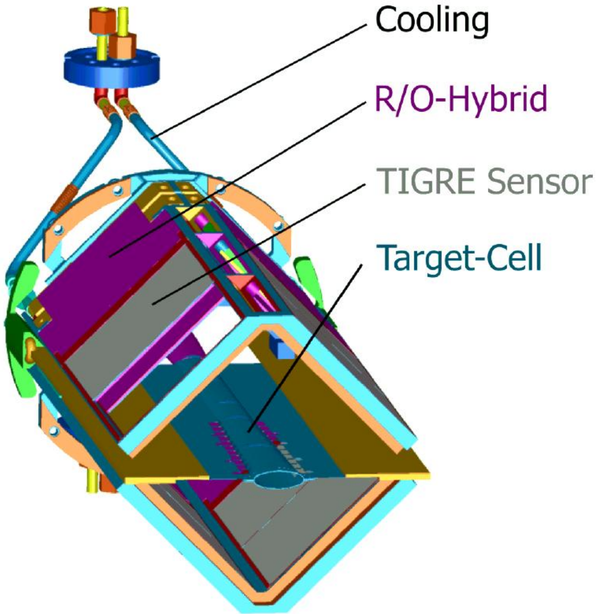

Figure 3.6: *Drawing of the diamond-shaped support structure of the Silicon Strip Detector (SSD) and the target cell in the centre of the SSD.*

The SSD is sensitive to energy depositions from Minimum Ionising Particles (MIP), which pass through the SSD, up to large energy depositions from protons stopping in either silicon layer. To cover the large dynamic range of the expected signals each sensor strip is connected to a high- and low-gain channel. The read-out itself is based on HELIX128 chips [17] that are already used at HERMES for the Λ-wheels [19, 20].

3.2.3 Scintillating Fibre Tracker

Charged particles of higher momenta which escape the scattering chamber are detected by the SFT. Their momentum is determined by the deflection of their track in a magnetic field which also allows the identification of the sign of the charge. Furthermore the SFT has to provide PID for protons and pions in the momentum regime below 650 MeV/c (see tab. 3.1).

The SFT consists of two concentric barrels of scintillating fibres. Each barrel in turn consists of two sub-barrels, but, whereas the inner sub-barrel is oriented parallel to the beam axis, the outer sub-barrel is inclined by 10° in a stereo configuration. This configuration allows the determination of a space point of a particle track for each barrel. Combining the track information from the SFT and the SSD,

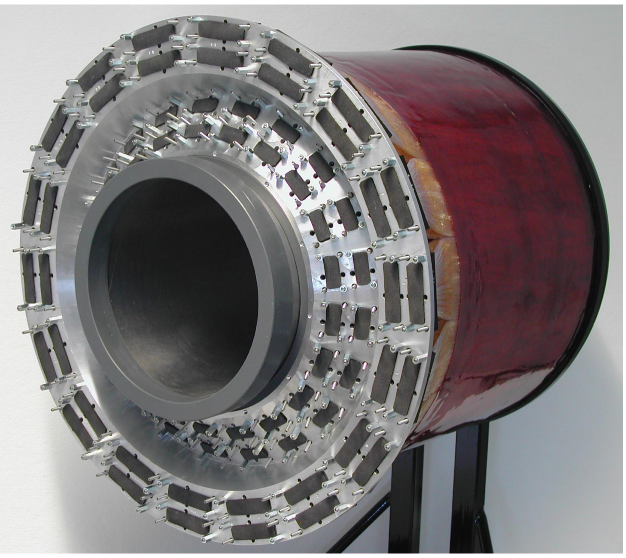

Figure 3.7: *Picture of the completed Scintillating Fibre Tracker (SFT) mounted to a dummy scattering chamber. Protective caps are put onto connectors. Kapton film on outer barrel serves as protection from mechanical influences.*

a particle track can be fully reconstructed and its momentum determined by measuring the bending radius. A maximum distance between inner and outer barrel is desirable in terms of maximising the lever arm for momentum resolution. However, the outer dimensions of the SFT are constrained by the scattering chamber and the PD. Abandoning a separate housing for the SFT ensures the best utilisation of the available space. The SFT has of course to be sealed against the scattering chamber and the PD to ensure light tightness. The momentum determination is deteriorated by multiple scattering of the particles inside the traversed material. Therefore the material budget of the SFT has to be minimised, suggesting a self-supporting structure.

The energy loss in the scintillating fibres, depending on the particle type and its momentum, will be used for PID. Therefore the read-out of the SFT has to provide not only information on the space point of the particle track but also on the deposited energy. The read-out electronics is based on front-end cards using GASSIPLEX chips [18, 21]. The scintillating fibres can only be read out on the upstream end due to tight space requirements because of the HERMES vacuum system and the Λ-wheels [17]. The scintillating fibres are connected via $4\,\mathrm{m}$ long light guides made of clear fibres to Multi-Anode Photo-Multiplier Tubes (MAPMT).

The steps to design and construct a SFT meeting these requirements are described in detail in chapter 4. The ready-made SFT mounted on a dummy scattering chamber is shown in fig. 3.7.

3.2.4 Photon Detector

The PD complements the tracking detectors of the Recoil Detector. Its primary purpose is the detection of photons from neutral pion decays which are not observed in the SSD and SFT. Neutral pions are created in the decay of an intermediate Δ-resonance with a proton in the final state mimicking an exclusive scattering process. The PD thus facilitates the background suppression for hard exclusive scattering events. Furthermore the PD can enhance the PID capabilities of the Recoil Detector. Finally, a cosmics trigger can be provided by the PD using cosmic muons for alignment studies of the assembled Recoil Detector.

To achieve its primary aim, the PD is based on a segmented shower detector design. Three layers of tungsten used as converter for the photons alternate with three layers of plastic scintillator as active detector material. The first tungsten converter layer has a thickness of 6 mm corresponding to two radiation lengths whereas the other converter layers only correspond to one radiation length each [22]. The scintillating layers are segmented to allow the reconstruction of a π° in the case of two detected photons. The innermost layer is oriented parallel to the beam axis and consists of 60 scintillator strips of 2 cm width and 1 cm thickness. The two outer scintillating layers are inclined by $\pm$ 45° with respect to the beam axis thus enabling a coarse spatial resolution of the point of impact of an impinging particle. Each stereo layer consists of 44 scintillator strips of similar dimensions to the innermost layer.

Each scintillator strip is read out via two WaveLength Shifting fibres (WLS) which are connected via clear fibres to MAPMTs outside the magnetic field of the Recoil Detector solenoid. The PD without its light tight supporting shell is shown in fig. 3.8. The outer stereo layer with its 45° inclination and the WLS fibres are clearly visible. The PD will finally be mounted flush with the magnet bore.

Figure 3.8: *Assembling of the Photon Detector. The light tight supporting shell is missing. The scintillator strips of outer stereo layer and wavelength shifting fibres are visible. The picture was taken before the fibres have been cut at the connectors seen in the upper part of the picture.*

Chapter 4

The Scintillating Fibre Tracker

The Scintillating Fibre Tracker (SFT) is one of the key components of the HERMES Recoil Detector. The main purpose of the SFT is to track and identify recoiling protons in the momentum range between 250 – 1400 MeV/c. In addition Particle IDentification (PID) capabilities for distinguishing protons and charged pions with momenta up to 650 MeV/c are required to suppress non-exclusive background processes, e.g. intermediate Δ-production [17]. An overview of all requirements is given in tab. 3.1. In the following, the design and construction demands, and the methods that were developed to cope with them, are discussed. Finally, results of a test experiment with prototype SFT modules conducted at the GSI accelerator facility are presented.

4.1 Design and Construction

Since the late 1980's, large scale scintillating fibre trackers were built for high energy experiments, among them UA2 [23], CHORUS [24] and DØ [25]. This led to massive improvements in scintillating fibre technology, e.g. light yield and radiation hardness. The SFT follows the basic design of the fibre tracker for the DØ experiment which has features in common to the SFT, namely that it surrounds the interaction point and provides tracking inside a solenoidal magnetic field.

Reconstructing particle tracks demands the measurement of a set of space-points along this track. The SFT is intended to deliver two that, combined with information from the Silicon Strip Detector (SSD) or the beam position, yield enough information to reconstruct the particle deflection in the longitudinal magnetic field and thus measure the momentum of the particle. The radius of curvature ρ of a particle track in a magnetic field, given by [26]

$$\rho = \frac{p_\perp}{eB} \tag{4.1}$$

with $p_\perp$ being the transverse momentum with respect to the magnetic field B and e being the particle charge. Additionally, the charge of the particle can be deduced from the curvature of the track. The extraction of spacepoints can be achieved by combining fibre layers parallel to the beam axis with stereo layers, which are tilted by a certain angle with respect to the beam axis as shown in fig. 4.1. The unique correlation between the fibres hit in parallel and stereo layers determines a spacepoint. The SFT consists therefore of two similarly constructed concentric barrels of different diameters. The barrels in turn are divided into two sub-barrels each. The inner sub-barrel is oriented parallel to the beam axis and the outer one is tilted according to the above mentioned reconstruction principle. The tilt angle is constrained by construction demands and the necessity of avoidance of correlation ambiguities.

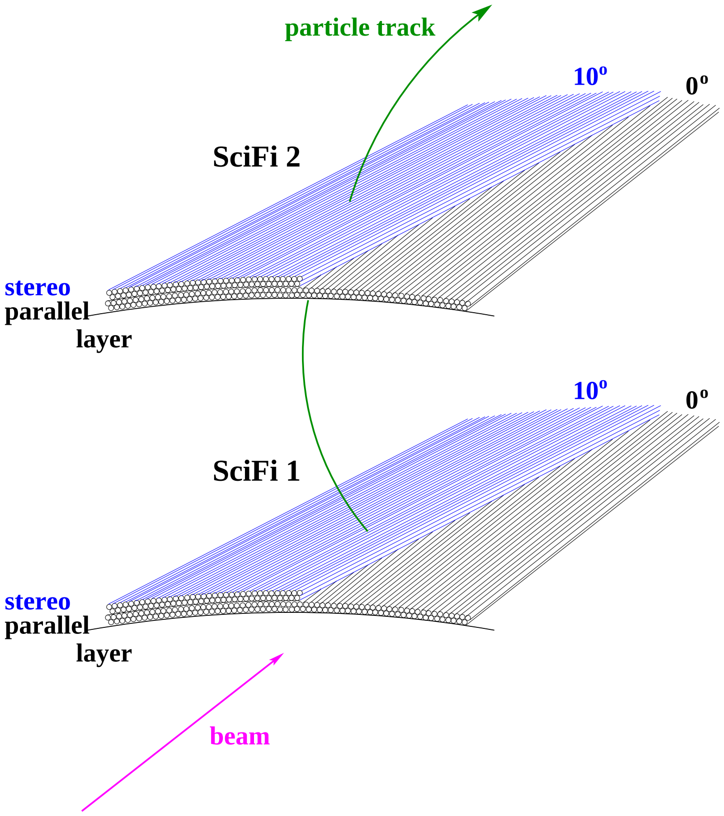

Figure 4.1: *Principle of track reconstruction with Scintillating Fibre Tracker (SFT).*

For the SFT a tilt angle of 10° was chosen, yielding a modest polar angle resolution while still being simple to assemble. The parallel sub-barrel ensures a good azimuthal resolution which is necessary for a high effectiveness of the coplanarity cut. Each sub-barrel in turn consists of two layers of scintillating fibres in dense packing, ensuring a high detection efficiency, even for Minimum Ionising Particles (MIP), which is essential for track reconstruction. The spatial resolution σ of two staggered layers, neglecting contributions from multiple scattering, is given by [27]

$$\sigma \propto \frac{D}{\sqrt{12}} \tag{4.2}$$

with D being the fibre pitch between the staggered layers. In case of a fibre pitch of $0.5\,$mm as anticipated for 1mm fibres, the expected spatial resolution σ is $150\,\mu m$. This determines also the theoretical resolution in the azimuthal angle ϕ, which is then $0.0014\,$rad — well below the limit of $0.05\,$rad given in tab. 3.1 allowing to exploit the advantages of a coplanarity cut.

The spatial resolution is not only determined by the resolution of the SFT barrels but also by contributions from multiple scattering. Recoiling particles of a Deep Inelastic Scattering (DIS) event traversing the Recoil Detector pass through the SSD and, more importantly, the scattering chamber, before entering the inner SFT barrel. Deflection of particles due to multiple scattering is described by Moliere's Theory [28]. The mean projected deflection angle Θ_{rms}^{proj} [26] can be approximated by

$$\Theta_{rms}^{proj} = \frac{13.6}{\beta c p}\sqrt{\frac{x}{X_0}} \tag{4.3}$$

with X_0 being the radiation length of the traversed material, p the particle momentum and βc the velocity of the particle. Θ_{rms}^{proj} can be translated into a lateral displacement as shown in fig. 4.2, given the size of the SFT barrel.

The dashed line in fig. 4.2 corresponds to the expected resolution of two staggered layers of 1mm fibres. The momentum range investigated is determined by DVCS and Δ-decay kinematics, cf. fig. 3.4. For protons the resolution is completely dominated by multiple scattering. Pions are expected at momenta below $800\,$MeV/c where contributions from multiple scattering dominate as well. Taking this into account, a fibre diameter of $1\,$mm was found to satisfy the resolution demands. Employing smaller fibres would not enhance the spatial resolution but increase only the complexity of construction. For the outermost barrel the fibre diameter could be increased without deteriorating the resolution, but for production reasons $1\,$mm fibres are used. Due to already large deflections for low momentum particles because of multiple scattering in the scattering chamber walls, the material budget in the SFT itself has to be kept to a minimum. Therefore the barrels are being built as a selfsupporting structure, avoiding additional scattering in inactive parts of the detector.

The different energy loss ΔE of protons and pions in the fibres is exploited for PID. This method has to be effective for momenta up to $650\,$MeV/c, as the main portion of pions is expected at momenta below this value, cf. sec. 3.1.

4.1.1 Scintillating Fibres

Scintillating fibres consist of a core in which the scintillation light is produced, surrounded by one (single-clad) or two (multiclad) cladding layers. Choosing the index of refraction of fibre core and cladding appropriately (cf. tab. 4.1) light

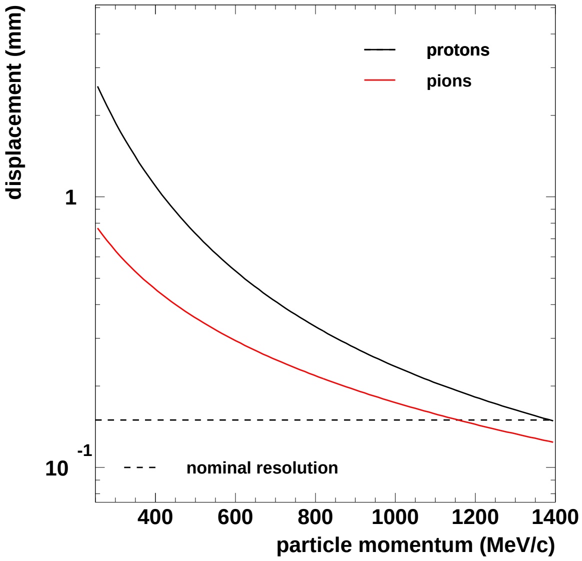

Figure 4.2: *Lateral displacement of a particle track at the innermost Scintillating Fibre Tracker (SFT) barrel due to multiple scattering assuming an aluminium scattering chamber of* 1.2 *mm thickness and neglecting contributions from the Silicon Strip Detector (SSD). The dashed line corresponds to the expected resolution of two staggered layers of 1mm fibres. Data on radiation length taken from [29].*

transport inside the fibre due to total internal reflection becomes possible. The scintillation light contained within the total reflection cones, which are determined by the critical incidence angle θ_c, in case of the fibre core given by

$$\theta_c^{core} = \sin^{-1}\left(\frac{n_{clad}}{n_{core}}\right) \tag{4.4}$$

with n_{core} and n_{clad} being the index of refraction of the corresponding fibre part, is then trapped inside the fibre core and transported along its axis. The modal parameter V given by

$$V = \frac{2\pi}{\lambda}\rho\sqrt{n_{core}^2 - n_{clad}^2} \tag{4.5}$$

with λ being the wavelength, ρ the core radius and n_{core} and n_{clad} as defined in eq. 4.4, is sufficiently large for the considered fibres that light propagation can be described in the approximation of geometrical optics [30].

The fibre core consists of polystyrene (PS)[1] mixed with scintillation dopants, usually organic compounds. These dopants determine the scintillating and optical properties of the fibre and also mechanical ones, e.g. radiation hardness.

---

[1] C_6H_5CH=CH_2

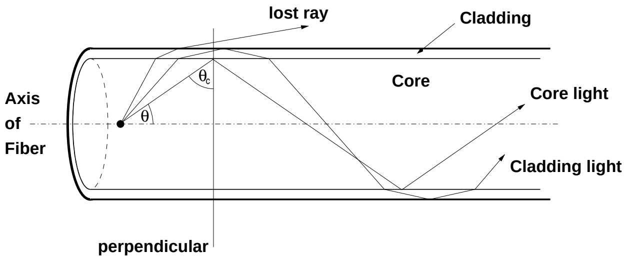

Figure 4.3: *Light propagation in a scintillating fibre for light rays emitted on-axis.*

The fibre cladding consists of polymethylmethacrylate (PMMA)[2] and fluorinated PMMA for the outer cladding in case of multiclad fibres. There are no additional scintillating dopants present in the cladding so that no scintillation occurs within the cladding layer. Also the cladding serves two secondary purposes. It protects the core from mechanical damage thus ensuring perfect surface conditions for total reflections and it also prevents primary scintillation light leaking into neighbouring fibres.

Table 4.1: *Important characteristics of typical materials used in fibre production [31, 32].*

Material	Index of refraction	Density $\rho\ \left[\frac{g}{cm^3}\right]$	Radiation length $X_0\ \left[\frac{g}{cm^2}\right]$
Polystyrene	1,59	1,05	43,8
PMMA	1,49	1,19	40,55
fluor. PMMA	1,42	1,43	40,55

At macroscopic level the scintillator emission is isotropic, leading to a poor trapping efficiency ϵ [30]. For scintillation at a point on the fibre axis, the angle of incidence of a light ray at the reflecting surface is determined solely by the polar angle θ, as depicted in fig. 4.3. This class of rays is called ”meridonial rays” [33]. In order to further discussion of meridonial rays propagating in a fibre, the complementary angle θ_{tr} of the critical angle θ_c, defined by

$$\theta_{tr}^{core} = \cos^{-1}\frac{n_{clad}}{n_{core}}, \tag{4.6}$$

is introduced. A meridonial light ray will then be trapped in the core if $\theta < \theta_{tr}^{core}$. Light not trapped in the core can be refracted into the cladding and trapped there by total internal reflection. For multiclad fibres this can happen at the inner cladding-outer cladding interface as well as the outer cladding-air interface thus enhancing the trapping efficiency. The trapping efficiency ϵ for meridonial rays is described, in case of the core, by

$$\epsilon_{core} = 1 - \frac{n_{clad}}{n_{core}} \quad , \tag{4.7}$$

---

[2] $C_5H_8O_2$

leading to an efficiency for light trapping of only 6.8% for the chosen SFT fibres. Scintillation light emitted away from the fibre axis has an angle of incidence with respect to the reflecting surface which depends on both polar and azimuthal angle of emission. These rays are denoted as skew rays [33] further on. The incidence angle Θ of skew rays is given by

$$(\cos\theta)^2 + \left(\frac{r}{\rho}\sin\theta\right)^2 = (\sin\Theta)^2 \quad , \tag{4.8}$$

with r being the distance of closest approach of the skew ray to the fibre axis and ρ the core radius [30]. Skew rays will be trapped in the core if $\Theta > \theta_c^{core}$ and in the cladding accordingly. Equation 4.8 demonstrates that skew rays can be trapped with polar angles θ larger than the complementary angle θ_{tr}. Adding skew rays to meridonial rays would change the trapping efficiency but these rays suffer many more total reflections and a longer path length than meridonial rays. Therefore for long fibres their contribution can be neglected [30].

Light transported in the outer cladding can be neglected as well due to very short absorption lengths (in the order of few millimeters) because of imperfect surface conditions [30, 34]. Furthermore glue will be applied to the fibre shell suppressing total reflection and thus absorbing the cladding light effectively as shown in fig. 4.4.

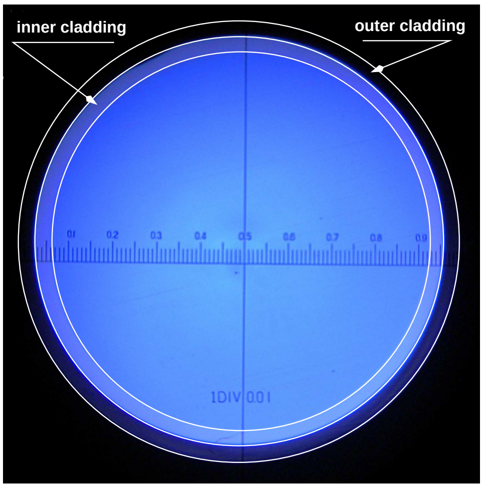

Figure 4.4: *Suppression of light transport in the outer cladding layer. A Pol.Hi.Tec 1mm doubleclad scintillating fibre glued to a SFT connector is shown. The fibre is illuminated by a fluorescent tube from from the left side at a distance of 15cm from the connector. The fibre core and the inner cladding layer are clearly visible whereas in the outer cladding layer basically no light is observed. The small fraction of light in the outer cladding visible in the lower right corner is due to scattering of the initial light.*

The fraction of trapped light is then guided along the axis to the fibre end. Before it reaches the fibre end, some light will be lost. Detracting from the amount of light that reaches the end of the fibre some losses, caused by an overlap of the emission and absorption band of the fibre dopants leading to self-absorption of the scintillation light, do exist. These light losses are increased by Rayleigh scattering on small density fluctuations in the core enhances the light loss, especially for wavelengths below 400 nm [33]. Furthermore, small imperfections at the core-cladding interfaces cause small reductions from unity for the total reflection coefficient and inducing thus further light losses [30]. At the fibre end, Fresnel's losses due to reflections occur depending on the coupling material. Fresnel's losses R are described by [35]

$$R = \left(\frac{n_1 - n_2}{n_1 + n_2}\right)^2 \tag{4.9}$$

with n_1 and n_2 being the refractive indices of the fibre core and coupling material. For an core-air interface, Fresnel's losses amount to approximately 5%.

The scintillation process taking place in the core is depicted schematically in fig. 4.5. An ionising particle traversing the fibre and depositing energy first excites the electronic levels of PS. The fluorescence yield is enhanced by adding an aromatic scintillator. Intermolecular energy transfer between base plastic and scintillator via strong dipole-dipole coupling (Förster transition) [30] requires an overlap of PS emission and scintillator absorption band. If the scintillator emits in the opaque region of PS a WaveLength Shifter (WLS) must be added in order to shift the emission to the transparent region of PS. This WLS ideally features a high quantum efficiency. Its concentration can be small since here a radiative energy transfer is taking place [33, 30], requiring an optical absorption length larger than 150 μm. This radiative transfer represents a possible source of crosstalk between adjacent fibres although this is suppressed by the cladding, as mentioned above.

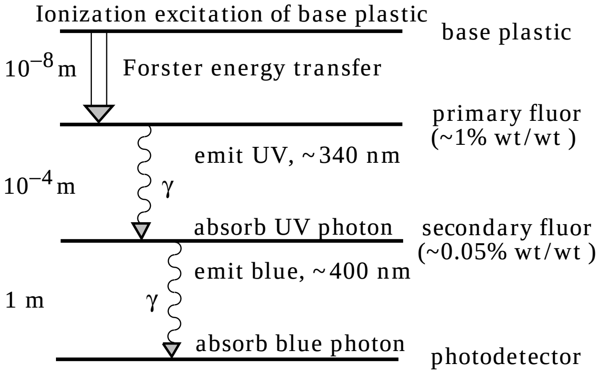

Figure 4.5: *Schematic diagram of scintillation process in organic scintillators [29].*

Previous studies on scintillating fibres [32, 36] indicated that Kuraray SCSF-78M fibres exhibit a superior light yield and radiation hardness. Studies on these fibres performed by DESY Zeuthen [36] indicated that the light yield changes not significantly after the absorption of a radiation dose of about 1 Mrad. A light yield comparison between Pol.Hi.Tec and Kuraray SCSF-78M fibres was performed independently using a Hybrid Photo-Multiplier Tube (HPMT)[3] which offers a superior resolving power for individual photoelectron peaks [37]. A HPMT consists of a light-detecting photocathode and a silicon diode. Photoelectrons emitted by the photocathode are accelerated by an electrostatic potential in the order of a few keV and impinge on the silicon diode. The large number of electron-hole pairs created in the silicon diode by the impinging photoelectrons reduces the statistical fluctuations and accounts for the excellent resolution compared to a standard PMT. The excellent resolution of a HPMT is obtained only at the expense of signal amplification as the typical gain of a HPMT is an order of magnitude less compared to a standard Photo-Multiplier Tube (PMT). A typical ADC spectrum obtained with a scintillating fibre coupled to a HPMT is shown in fig. 4.6 a. Individual photoelectron peaks can be clearly distinguished which enables photon counting for weak light sources like scintillating fibres excited by radioactive sources. The tail on the right hand side of each photoelectron peak can be attributed to photoelectrons being backscattered onto the silicon diode. The contribution of each peak to the total spectrum is distributed according to Poisson statistics, i.e. the mean value of the HPMT spectrum corresponds to mean number of photoelectrons created by the impinging light.

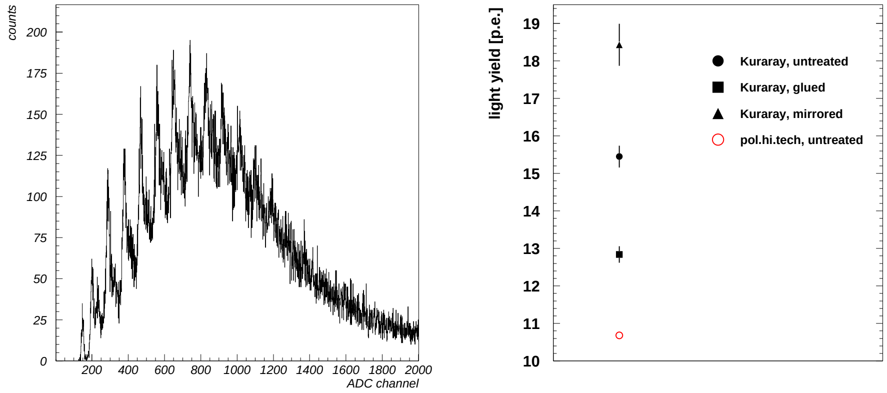

(a) (b)

Figure 4.6: *Measuring light yield of scintillating fibres with Hybrid Photo-Multiplier Tube (HPMT):*
(a) Typical fibre response spectrum obtained with HPMT. Individual photoelectrons are resolved.
(b) Comparison of light yield for 1 mm *double cladded fibres from Pol.Hi.Tec and Kuraray. Scintillating fibres were irradiated by* ^{90}*Sr source and the light yield was determined with a HPMT. Kuraray fibres were also mirrored on one end face and glue was applied to the fibre shell.*

Fibre samples of 15 cm length were placed in a socket and coupled with optical

---

[3] DEP PP0275

grease[4] to the entrance window of the HPMT for this study. A ^{90}Sr source and a small plastic scintillator were then placed at the far end of the fibre. The plastic scintillator was read out with a conventional PMT and served as a trigger detector. Electrons emitted by the source pass through the scintillating fibre and enter the trigger detector, selecting in this way only fast electrons which can be regarded as MIPs since slower electrons will not penetrate the fibre placed between the source and the trigger detector. The light yield was measured with various samples for each manufacturer. In agreement with other studies [32, 36] Kuraray SCSF-78M fibres proved to be superior in light yield compared to Pol.Hi.Tec fibres. The results are shown in fig. 4.6 and are given in tab. 4.2. Moreover, the influence of glue applied to the fibre shell and mirroring of the far end of a fibre were studied for Kuraray fibres. Mirroring of the far end increases the light yield by about 20%. Glue applied to the fibre shell reduces its light yield by 20% which is due to the loss of cladding light. Contributions from cladding light to the total light yield are only important for short fibres as explained above. Later on the cladding light is either lost at the cladding-glue interface or absorbed by glue in the connectors as will be explained in the following section. The fraction of cladding light contributing to the results given in tab. 4.2 has to be considered of course, when estimating the light yield for MIPs of the final SFT set-up.

Table 4.2: *Results of light yield measurements for different scintillating fibres. All fibres are doubleclad with a diameter of* 1 mm. *Light yield is given in units of photo electrons (p.e.). Measured with Hybrid Photo-Multiplier Tube (HPMT).*

Manufacturer	Light Yield (p.e.)		
	pure	mirrored	glued
Pol.Hi.Tec.	10.68 ± 0.07	–	–
Kuraray	15.45 ± 0.29	18.43 ± 0.56	12.84 ± 0.22

Previous studies on Kuraray fibres indicated an enhanced sensitivity to irradiation with ultraviolet (UV) light [38], affecting the absorption length and consequently the light yield. This effect could not be confirmed for the selected Kuraray fibres of the SFT. In contrast to the SCSF-78M fibres which employ a two-component system [39] with PTP[5] as primary scintillator and TPB[6] as WLS, the fibres studied in [38] use an one-component system with 3HF[7] as scintillator. Nevertheless, exposure of the fibres to daylight was restricted to a minimum and careful handling, e.g. wearing gloves when touching fibres, was obligatory.

After performing these studies and reading the available literature, Kuraray SCSF-78M with a diameter of 1mm were chosen as active material for the SFT.

---

[4] Baysilon 300

[5] p-terphenyle

[6] 1,1,4,4-Tetraphenyle 1,3-Butadiene

[7] 3-hydroxyflavone

The basic characteristics of this fibre type are given in tab. 4.3.

Table 4.3: *Properties of Kuraray SCSF-78M multiclad scintillating fibres of 1mm diameter [31].*

characteristic	value
peak emission	$450\,\mathrm{nm}$
att. length	$> 4\,\mathrm{m}$
decay time	$2.8\,\mathrm{ns}$
cladding thickness	$30\,\mu m$
trapping efficiency	10.8%

The cladding thickness amounts to 3% of the overall diameter for inner and outer cladding each, i.e. the active fibre core has a diameter of $0.94\,\mathrm{mm}$. The tolerance in diameter is specified by the manufacturer to be below 2% [31].

4.1.2 Optical Read-Out

The read-out of the scintillating fibres faces several difficulties. First of all, the Recoil Detector is surrounded by a solenoidal magnet with a field strength of 1 T. Secondly, the available space in the upstream area is very limited because of pump stands for the vacuum system and cabling of the other subdetectors. A combination of clear fibres acting as light guides and Photo-Multiplier Tubes (PMT) is used to accomplish the read-out of the scintillating fibres.

As the total number of read-out channels amounts to 4827 (cf. tab. 4.5) a compact light detecting device is mandatory. In addition, a linear response and a large dynamic range are required as the deposited energy ΔE will be used for PID purposes. Multi-Anode Photo-Multiplier Tubes (MAPMT) H7546 from Hamamatsu, employing a metal channel dynode structure with 64 channels, fulfil all demands. With compact outer dimensions (cf. fig. 4.7 a) the 64 channels are arranged in an 8 × 8 array with a pixel size for each channel of $2 \times 2\,\mathrm{mm}^2$. A schematic overview of the photocathode layout and pixel size is shown in fig. 4.7 b. The metal channel dynode structure is an array of small linear focused dynodes, which leads to negligible crosstalk in the dynode structure itself [40]. The MAPMT housing is made of black POM[8] and accommodates the voltage divider, as well. The spectral response of the employed bialkali photocathode ranges from 300 – 650 nm with a maximum sensitivity at 420 nm which is close to the peak emission wavelength of the selected SCSF-78M fibres (cf. tab. 4.3). Given the fast signals from scintillating fibres (cf. tab. 4.3) a fast rise time of $1.5\,\mathrm{ns}$ of the H7546 MAPMT suits these needs. The typical gain for the envisaged working voltage is of the order of 10^5 – 10^6. Gain uniformity across all anodes of a MAPMT is typical 1:3 [41] and is improved to

---

[8] Polyoxymethylene

1:2 for MAPMTs preselected by Hamamatsu [18] which is important for an application of advanced analysis algorithms and measurement of the deposited energy ΔE (since the working voltage defining the gain cannot be adjusted for each channel individually but only in common for all channels). Individual calibration of each pixel allows to account for possible gain variations.

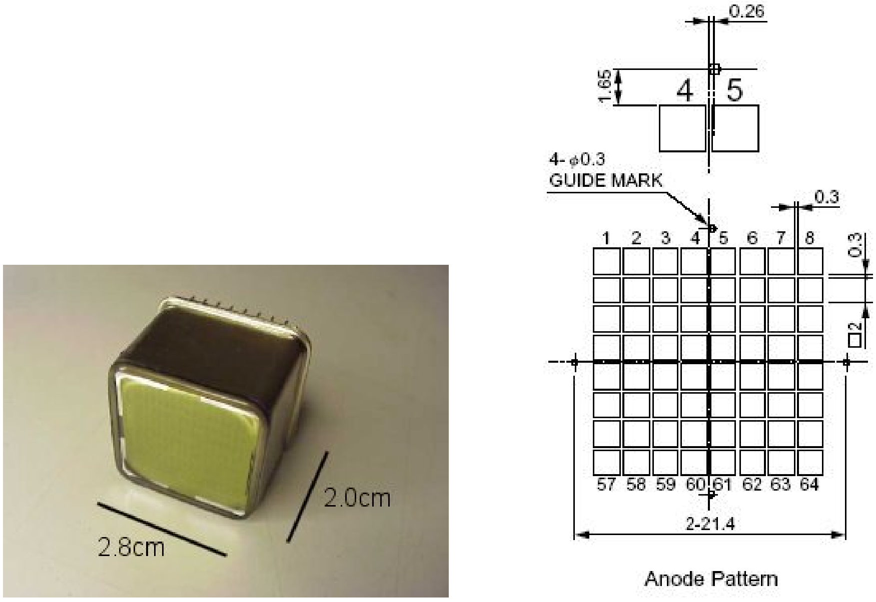

(a) (b)

Figure 4.7: *(a) Hamamatsu R5900-00-M64 Multi-Anode Photo-Multiplier Tube (MAPMT) without housing and voltage divider;*
(b) Layout of PMT cathode plane and correlation to reference marks.

The readout electronic for the MAPMTs uses the design of the HADES[9] Ring Imaging Čerenkov (RICH) Preprocessing Frontend Module (PFM) [21]. In order to adapt the fast MAPMT signal to the PFM, a Charge Divider Circuit (CDC) was integrated on the Photo-Multiplier Board (PMB) [42]. A sketch of this CDC is shown in fig. 4.8. The ADC on the PFM is designed such that large charge signals correspond to low ADC values. Given the PMB circuit layout, a higher capacity in the CDC leads to a smaller charge signal on the PFM. The final value for the capacitor of the CDC has to satisfy the demands for energy resolution while limiting the total charge transmitted to the PFM. The behaviour of different capacities in the CDC was studied in a test experiment at GSI and a value of 68 pF was chosen.

The MAPMTs are sensitive to magnetic fields, especially along the dynode axis. Variations in gain of up to 10% for a field of 35 Gauss are reported by Hamamatsu [43], which excludes mounting these MAPMTs close to the active SFT components inside the Recoil Detector magnet as fringe fields of several hundred Gauss

---

[9] High Acceptance DilEpton Spectrometer

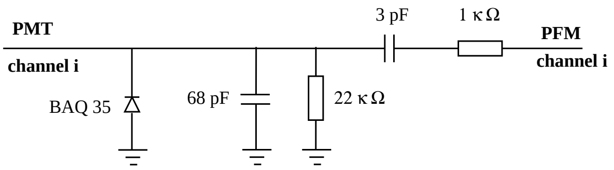

Figure 4.8: *Scheme of Charge Divider Circuit (CDC) on Photo-Multiplier Board (PMB). The 68pF-capacitor was subject to studies in a test experiment at GSI.*

are expected given model calculations of the magnetic field. Additional shielding with μ-metal and soft iron allows for a maximum field strength of the fringe fields of 50 Gauss which can be achieved by a distance of 2.5 m between MAPMT and solenoid axis.

The scintillation light has therefore to be transported from the active SFT part to the MAPMTs. Clear fibres constitute the best solution since they possess similar optical properties as the scintillating fibres and can be shaped to fit the available space. In order to minimise optical crosstalk on the MAPMT cathode the Light Guide (LG) fibres have to be centred on the corresponding pixel. Optical crosstalk is typically in the order of 2% for a 1 mm fibre centred on the pixel within 0.2 mm [40]. Unfortunately, the centre position of the cathode is not exactly correlated with the MAPMT housing. Therefore the centre position of each MAPMT cathode with respect to the housing has to be determined. Measuring the position of three of the guide marks on the MAPMT cathode (see fig. 4.7) with a precision of approximately $10\,\mu m$ allows to determine the cathode centre position with sufficient accuracy to achieve the above mentioned optical crosstalk level. Fig. 4.9 shows the offset of the cathode centre position found for a sample of 40 MAPMTs. Deviation up to 0.5 mm had to be taken into account for the actual connection between the LG and the respective MAPMT.

The connection of LG fibres to the active SFT part at one end and to the MAPMTs at the other imposes several conditions on the LG design. Firstly, the number of channels of MAPMT fixes the number of fibres in a LG. Sharing of fibres between different MAPMTs is not practical as the whole set-up has to be light tight and each LG should, in principle, be mountable individually for easy inspection and testing. Furthermore, each light guide needs to be centred precisely on the corresponding MAPMT. The connection of the LG to the individual scintillating fibres of the SFT has to be precisely aligned as well in order to avoid additional light losses at the connection [44]. To ease restrictions, a slightly larger diameter of 1.1 mm for the LG fibres is chosen in comparison to 1 mm for the scintillating fibres. A similar design was proposed for the DØ fibre tracker [45]. 1.1 mm clear multiclad Kuraray fibres were chosen due to their superior attenuation length and radiation hardness [36]. The values for the attenuation length given by the manufacturer [31] and obtained in studies by DESY Zeuthen [36] and by J. Streit-Lehmann from our group [47] are given in tab. 4.4. The large difference between the obtained values can be explained by different measuring techniques

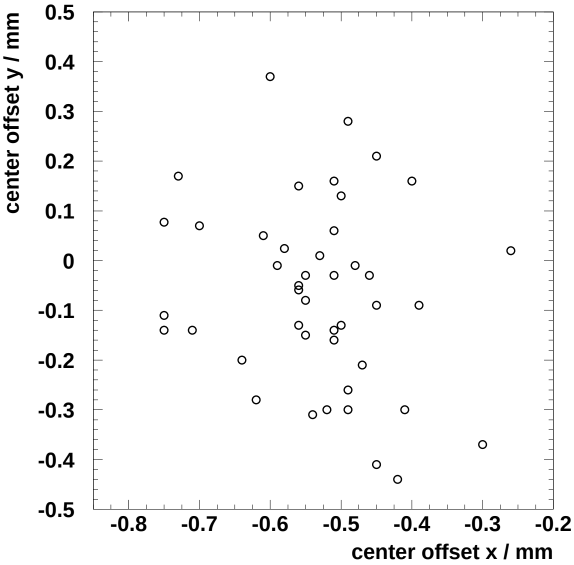

Figure 4.9: *Variation of Hamamatsu H7546B Multi-Anode Photo-Multiplier Tube (MAPMT) cathode centre position.*

and depends strongly on the length of the employed fibre sample [46].

Table 4.4: *Absorption length for clear Kuraray fibres from different studies.*

	Absorption length (m)
Kuraray [31]	9
Zeuthen [36]	6.50 ± 0.72
J. Streit-Lehmann [47]	5.70 ± 3.70

Kuraray produces a special version of clear fibres called S-type where the PS core has a molecular orientation along the fibre axis [31]. S-type fibres are mechanically stronger against cracking at the cost of transparency according to the manufacturer. As the available space in experimental area of the Recoil Detector demands a circuitous layout of the LGs, S-type fibres were chosen. The minimum bending diameter without significant light losses was determined to be to 2 cm [47]. Radiation damage deteriorates the absorption length and accordingly decreases the amount of light transmitted to the MAPMTs. A decrease in absorption length of up to 40% for an absorbed dose of 1 Mrad was found [49] which is tolerable as the expected integrated dose for the Recoil Detector is estimated to about 300 krad.

The transmission efficiency between scintillating and clear fibre depends, apart from precise alignment, on the distance of their end-faces. The gap width was varied up to 2 mm and the change in transmission recorded. The decrease in light yield is approximately linear to the gap width and was found to be 12% for a 100 μm wide gap which is in agreement with results of the D0 collaboration [45]. The use of optical grease as couplant was discarded as it enhances crosstalk at the corresponding connection and introduces a time dependent behaviour of the coupling efficiency [50]. This implies the necessity of precisely processed fibre surfaces for the LG and scintillating fibres of the SFT. The best surface quality was achieved with a two-step procedure, first using a standard ten-blade cutter for coarse machining and then employing a diamond fly-cut tool yielding optical quality surfaces. Transmission efficiencies of 90 – 95% are reported for this kind of coupling [36, 45, 50] and are achieved within SFT connector design constraints as well.

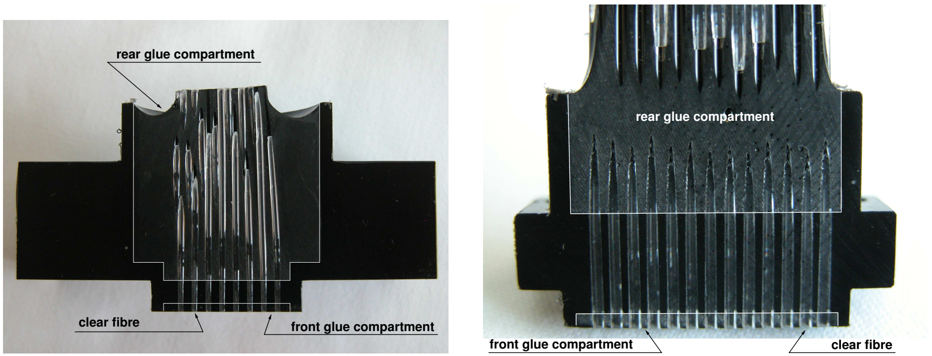

(a) (b)

Figure 4.10: *Details of SFT connector design:*
(a) Cross section of LG MAPMT-connector. Both glue compartments indicated by white lines;
(b) Cross section of LG SFT-connector, outer type. Both glue compartments indicated by white lines.

All SFT connectors are made of black POM, the same material as the MAPMT housing. POM offers similar thermal characteristics as the fibre material (PS, PMMA) and can easily be machined with high precision. Black POM is also light tight and thus suppresses crosstalk inside the connectors. Detailed construction drawings are given in appendix A.1. The connectors need to be precisely machined as any misalignment introduces additional losses [45]. The high precision necessary was achieved using CNC[10] milling machines [51]. The fibres will finally be glued to the connectors which imposes several difficulties. Multiclad fibres are difficult to glue because the outer cladding is made of a smooth, Teflon-like material [45]. In addition, the glue may not corrode the cladding and cause deterioration of the optical characteristics. A slow curing solvent-free epoxy resin[11] was chosen [52] which is mixed with black dye to prevent crosstalk in the connectors and absorb any remaining cladding light. The cured epoxy also allows for a precise

---

[10] Computerised Numerical Control
[11] Vosschemie Epoxy BK

machining of its surfaces necessary for achieving high transmission efficiencies.

All connector types of the SFT follow a similar design principle (fig. 4.10); A large rear glue compartment which serves as mechanical support and ensures a solid fibre fit and a small front glue compartment facilitating the fibre end-face machining as the glue encloses the fibre and protects the cladding from damage during milling. In between the glue compartments is the guiding section, comprising of precisely drilled holes for every fibre, thus determining the fibre alignment. The position of the fibre holes is controlled within $100\,\mu m$ [51] with respect to the alignment pins. For the MAPMT-connector, which matches the cathode pattern of the pixels, a special mapping scheme was devised allowing the disentanglement of signals from crosstalk. The SFT-connector has to be as compact as possible as hardly any space is available for reading out the scintillating fibres. Two scintillating fibres of the outer SFT barrel will be merged onto one MAPMT pixel, reducing the amount of readout channels considerably. This will be achieved by merging two separate LG fibres onto the same pixel, which necessitates a small change of the MAPMT-connector design and leads to LGs comprising of 128 fibres instead. The spatial resolution, although considerably reduced by this arrangement, is still governed by multiple scattering as explained in sec. 4.1.

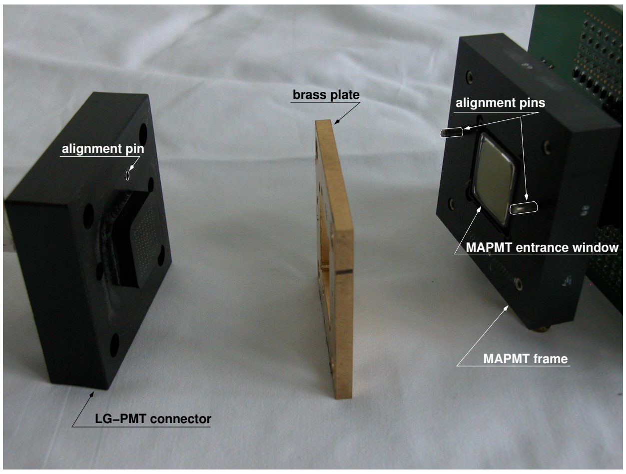

Figure 4.11: *Overview of LG-MAPMT connection. Alignment pin positions of LG-MAPMT and MAPMT frame are indicated. The brass plate in between MAPMT and LG-MAPMT connector ensures a precise alignment of the LG on the MAPMT cathode.*

Eventually, the LG-MAPMT connection consists of three pieces: a MAPMT glued into a frame, a brass plate and a LG furnished with connectors. The MAPMT-frame and the LG MAPMT-connector feature a set of two alignment pins each, the positions of which are precisely controlled. The corresponding brass plate has four precisely positioned guiding holes into which the alignments pins fit. The position of the guiding holes takes the MAPMT cathode offset into account and centres thus the LG-MAPMT connector position on the MAPMT cathode. The advantage of such an arrangement is the possibility to mass-produce LG connectors and

MAPMT frames as well as brass plate blanks. Only the guiding holes of the brass plate have to be set according to the individual MAPMT-cathode position. This, in turn, means that for each MAPMT an individual brass plate has to be manufactured which cannot be exchanged with another MAPMT. The LG-MAPMT connectors are pressed onto the MAPMT entrance window via four springs screwed to the MAPMT frame, yielding a perfect contact of the LG-MAPMT connector to the MAPMT. No optical couplant is used for the same reasons as for the scintillating fibre-to-LG connection.

The SFT-LG connection is designed in a similar way using a set of two alignment pins for precise positioning of the connectors, see fig. 4.17 b. Notwithstanding the LG-MAPMT connection a brass plate is redundant as the connectors are already machined to the necessary precision. Due to the limited space available, only four screws in the corners of a connector are used to ensure a tight contact of scintillating and LG fibres.

All alignment pin positions are placed such that an accidental permutation of the connector orientation, which would alter the correlation of scintillating fibres to readout channel, is prevented.

4.1.3 Barrel Construction and Integration

The basic design requirements for the SFT barrels are already explained in sec. 3.2. A schematic cross section of the Recoil Detector setup is shown in app. A.2.

The SFT consists of two barrels of scintillating fibres, a downstream endcap and a connector ring on the upstream end of the barrels. The endcap provides mechanical support of the SFT barrels and is used to seal the barrels light tight to the pump cross flange. Black POM was chosen as material for the endcap because of light tightness and background considerations. The development of electromagnetic showers inside the endcap material should be avoided which requires a low Z-material. Two sealings of foam rubber are therefore used (see fig. 4.12). The endcap is divided into an inner and outer part as the two barrels will be assembled and fitted with the corresponding endcap separately and only combined at the end. The connector ring on the upstream end serves for the connection of the SFT to the scattering chamber determining thus the alignment of the SFT with respect to the target cell and the SSD. Furthermore, it provides mechanical support for the LG-SFT connection to relieve the barrels from the forces exerted during installation of the LGs and the weight of the LGs themselves. Thus the connector ring, which is made of aluminium, has to accommodate openings for all LG-SFT connectors (fig. 4.17 a). The connector ring is constructed such that the fibre axis of inner barrel modules at the connector position is inclined by 30° with respect to the barrel axis due to LG assembling demands. Outer barrel modules' connectors are oriented parallel to the barrel axis.

A modular assembly of each sub-barrel is to be preferred due to production reliability. Each fibre of the SFT has to be machined on both ends by milling machines posing thereby a danger of destroying individual fibres. This threat can be

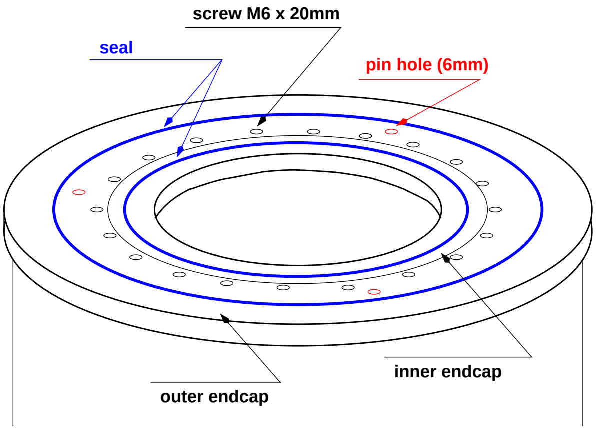

Figure 4.12: *Drawing of the SFT barrel endcap indicating inner and outer barrel endcap. Both endcaps are secured by 20 plastic screws. The endcap is equipped with two foam-rubber seals to facilitate light tightness of the SFT in the Recoil Detector set-up.*

Table 4.5: *Number of fibres and corresponding readout channels per Scintillating Fibre Tracker (SFT) sub-barrel.*

sub-barrel	inner barrel		outer barrel	
	fibres	readout	fibres	readout
parallel	1318	1318	2198	1099
stereo	1320	1320	2180	1090

avoided by machining all fibres before actually assembling the sub-barrels. The fibre modules then have to exhibit certain features allowing, finally, the assembly of sub-barrels. First of all, the glue, apart from not corroding the fibre cladding, has to be flexible in order to allow the possibility of adjustment of the module curvature to the desired barrel dimensions. Furthermore the modules have fit tightly to each other to avoid acceptance gaps. Overall, the barrel assembly procedure needs to yield barrels manufactured precisely to the desired dimensions without introducing additional support structures as this would lead to a degraded momentum resolution.

Prior to assembling SFT modules, all scintillating fibres are roughly cut to length, grouped into bundles of 200 fibres and one end is machined with a standard ten-blade cutter. Then the cut end faces are aluminised [53] to enhance the light yield.

An inner barrel module is comprised of 64 fibres, matching the number of pixels of a MAPMT, in two staggered layers (see fig. 4.13 c). An outer barrel module consequently consists of 128 fibres in the same configuration with two fibres being merged onto one MAPMT pixel as explained previously. For production reasons, the outer barrel modules are assembled from two inner barrel modules. Precast moulds made of polyethylene (PE) (see fig. 4.13 a) are used for assembling the fibre modules — defining thus the curvature of the modules, i.e. the moulds are differently shaped for inner and outer barrel modules. This precasting is especially important for the stereo sub-barrel modules whose shape follows a helical pattern. PE was chosen for the moulds, since its smooth surface prevents glue adhering which is important for a simple removal of the modules from the mould. In addition, the moulds are lined with mould release to further ease the removal of glued modules. The moulds feature precisely machined v-shaped grooves to control the fibre orientation. The grooves have a pitch of 1.04 mm accounting for production tolerances of the fibres [31]. The length of the grooves amounts to 260mm, which constitutes the ordered part of a module inside the design acceptance used for tracking. The overall length of a module is 340 mm as the remaining 80 mm are necessary to guide the fibres to the corresponding connector position without falling short of the minimum bending radius of 50 mm [31].

The DØ fibre tracker, employing a similar scheme for assembling fibre modules, used a polyurethane (PU) resin [54] which was adopted for the SFT modules. Main features of the PU resin important for module production are its viscosity, allowing the resin to fill all interspaces of a module, and pot lifetime, limiting ultimately the modules' size. Based on the results from an investigation, the two-component PU resin Ureol 5073A/6414B was chosen. A slightly modified mixing ratio of 7:1 enhances the pot lifetime to 30 minutes (this being necessary to complete a module). After mixing the two PU components, the resin is put into a vacuum chamber to remove small air bubbles that otherwise disturb the stability of a module. Then a layer of PU resin is cast into the grooves of the PE mould and the first layer of fibres is inserted. After surveying the accurate orientation of the fibres, another layer of PU resin is cast onto the fibres and the second layer of fibres is inserted into the grooves of the first layer thus aligning both layers. The module is completed by another layer of resin on top of the second fibre layer, enhancing the mechanical stability of the final module. A silicone spacer is applied to the last resin layer and a top cover is screwed to the mould (see fig. 4.13 a) to exert some pressure and thus ensure a precise orientation of the fibres. After curing the PU resin for 24 hours, the top cover is removed and the raw module carefully removed from the mould. Especially the edge fibres are at risk of being ripped off the module during this procedure. Before a raw module (see fig. 4.13 b) can be processed further, the PU resin has to cure for another week.

The raw modules are inspected optically for misplaced or missing fibres. During the first production phase a large fraction of modules exhibited misplaced fibres which necessitated a limit on the amount of PU resin used during assembly to approximately 4 g. Most modules with misplaced fibres were rejected since only detached edge fibres could be fixed with a cyanoacrylate based glue[12]. After inspection, excessive glue at the raw module edges is carefully removed with a piece

---

[11] RenLease QZ5111

[12] Patex Blitzkleber flüssig

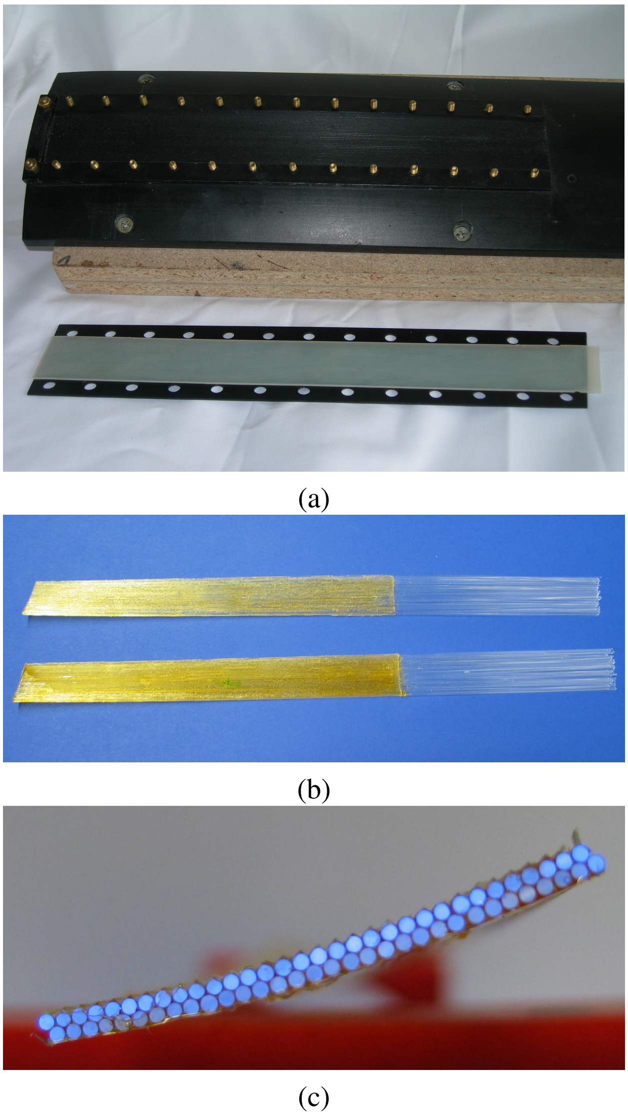

(a)

(b)

(c)

Figure 4.13: *Tools for production of Scintillating Fibre Tracker (SFT) modules and raw modules:*
(a) Precast mould for SFT module production mounted on supporting shell for correct curvature. In front cap and silicone spacer;
(b) Overview of two SFT prototype modules after removal from mould;
(c) Cross section of a SFT prototype module without mirrored end-face.

of rubber to allow a smooth assembly of the modules in the final barrel.

A prototype module was cast into epoxy resin and cut into ten pieces along the fibre axis to inspect the achievable precision of fibre orientation and pitch. The position of all fibres was measured by optical means to a precision of $15\,\mu m$ for four of these pieces. The measured fibre pitch in the lower and upper layer is

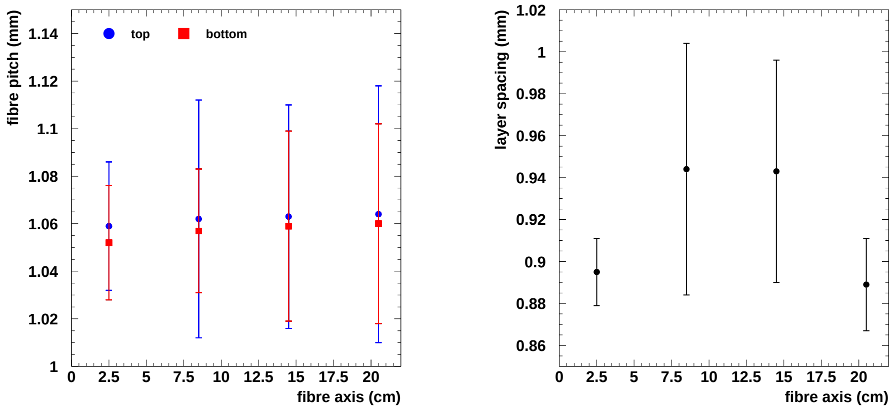

(a) (b)

Figure 4.14: *Measurement of fibre spacing inside SFT module:*
(a) Fibre pitch for inner and outer layer of a SFT module measured along module axis;
(b) Distance between inner and outer layer of a SFT module measured across module axis.

constant within error bars, see fig. 4.14 a. Moreover, the upper layer exhibits a systematically larger pitch, which is anticipated for a curved geometry. The distance between upper and lower layer varies along the fibre axis by about $50\,\mu m$, but the precision of the measurement is rather limited, cf. 4.14 b. Nonetheless, all deviations observed are smaller than the expected spatial resolution of $150\,\mu m$ which is due to the fibre diameter. Thus the mechanical assembly procedure for the SFT modules is proven to meet the design parameters.

The open fibre ends are fed into connectors (cf. fig. A.5 and A.6) similar to the LG connectors. The mapping of the fibres in a connector is surveyed by injecting light into the top fibre layer and inspecting the corresponding pattern at the connector end. The raw modules are then mounted on a supporting shell emulating the module position in the final barrel and thus adjusting the length of a module and fixing the position of the connector with respect to the connector ring, i.e. inner barrel modules need to be bent by 30° upwards (see fig. 4.15 a) to fit into the connector ring. After glueing the connector to a module only small corrections to its position are possible as the fibre bundle close to the connector obtains a high rigidity. The fibres are then glued to the connector with the same procedure as the LG fibres and the end-faces are machined to optical quality as in case of the LGs. 42 inner and 36 outer modules are necessary to assemble both barrels, however each outer module consists of two inner ones as described previously. In total, 114 modules were assembled, inspected and fitted with connectors.

Before assembling the final SFT barrels, the basic applicability of the assembling scheme needs to be proven. Therefore 36 inner modules, 18 of parallel and stereo type respectively, were assembled from 1mm clear fibres[13] in the above de-

---

[13] Toray PGR-FB1000

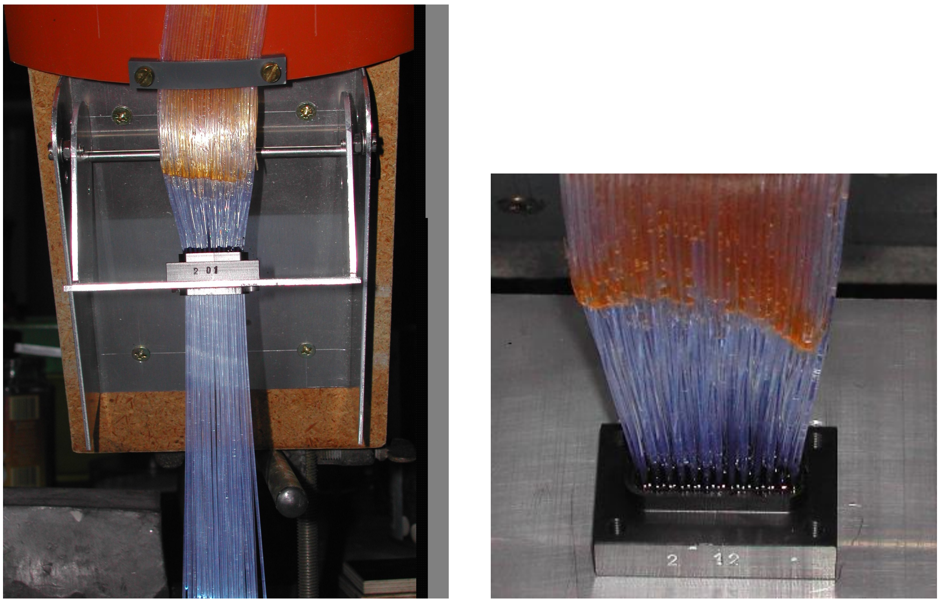

(a) (b)

Figure 4.15: *Glueing of connector to a Scintillating Fibre Tracker (SFT) module:*
(a) Fibre module attached to supporting shell with connector being bend upwards to fit in the connector ring;
(b) Close-up view of the rear glue compartment. The dense packing of the fibres leads to high rigidity which prevents corrections of the connector position after glueing.

scribed manner but without attaching a connector. For the actual barrel assembly a supporting shell determining the barrel dimensions was constructed which can be removed after completion of the barrel. Scale paper is then applied to the supporting shell to control the orientation of the parallel layer with respect to the barrel axis to better than 2 mrad. The scale paper is covered by a 0.125 mm thick Kapton film which ensures a safe removal of the supporting shell later on and serves as mechanical protection for the fibres. The parallel fibre modules are glued onto the Kapton film with a slow curing epoxy resin[14] allowing small corrections of the module orientation. During the curing period of the resin, the position of the modules is secured by two rubber rings. The stereo modules in turn are directly glued to the parallel modules and an additional layer of epoxy resin is applied to the barrel surface enhancing the stability. The $10°$ inclination of the stereo modules is controlled by a special gauge, see 4.16 a. With the construction of such a dummy barrel the assembling scheme could successfully be proven. Moreover, the gap width between adjacent modules was determined to be below $200\,\mu m$ which is well below the fibre radius, meaning that no artificial acceptance gaps are introduced and a complete coverage of the azimuthal angle ϕ is achieved.

After verification of the assembly scheme, the final barrels are assembled. For

---

[14] Vosschemie Epoxy BK

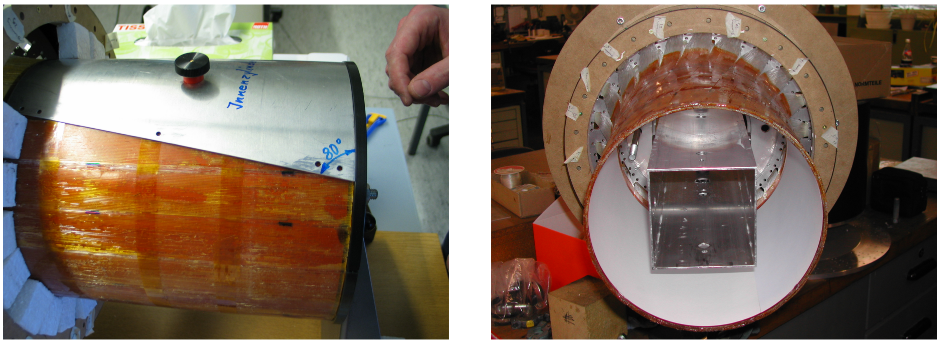

(a) (b)

Figure 4.16: *Assembly of a dummy barrel to prove assembly scheme:*
(a) Adding of the stereo modules to the dummy barrel. The custom-made gauge to control the stereo angle of 10° is shown;
(b) Dummy barrel after removal of the supporting shell. Scale paper is still attached to the Kapton film.

the inner barrel the connector ring needs to be integrated already as the upwards bent connectors can only be fitted into the corresponding opening during assembly. Therefore the orientation of each fibre module with respect to its corresponding connector opening is inspected and, if necessary, edge fibres are removed to centre the connector to its opening, see fig. 4.17 b.

After complete assembly of the inner barrel, the inner part of the endcap is attached. The endcap adds stability to the barrel and preserves its sphericity. Then the outer barrel is assembled on its correspondingly larger supporting shell. At this the connector ring is not integrated during assembly as the outer barrel connector can be fitted into their openings later on. After removal of the supporting shell both barrels are merged (see fig. 4.18) and the outer part of the endcap is attached. Finally, a Kapton film is applied to the outer barrel surface as mechanical protection. The completed SFT is shown in fig. 3.7.

A schematic drawing of the SFT cross section is shown in fig. 4.19 indicating the Kapton films at the inner and outer barrels. The nominal values of all relevant radii are given as well.

The completed SFT was then transferred to DESY Hamburg for final measurements. Outer and inner dimensions of the barrels were measured at DESY[15] with high precision devices [55]. The results are given in tab. 4.6. Deviations below 0.5 mm are observed compared to the nominal values, confirming the high accuracy obtained with the devised assembly scheme. In addition, the centre offset of the outer barrel with respect to the inner one was determined as well being below 0.2 mm.

Since the position and orientation of the fibres are not precisely enough known with respect to external reference marks, a dedicated alignment procedure using the

---

[15] DESY Fertigungskontrolle

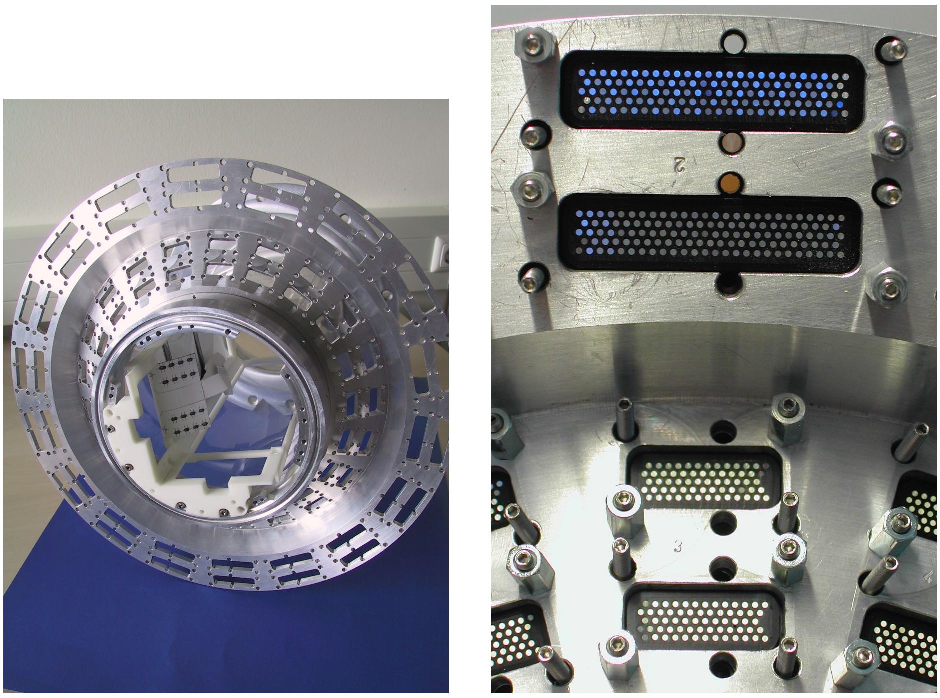

(a) (b)

Figure 4.17: *Overview of connector ring and fitted connectors:*
(a) Connector ring with dummy scattering chamber attached. Tilted connector plane for inner barrel recognisable;
(b) Fibre connectors for inner and outer barrel fitted to connector ring. Four threaded rods are attached to each connector for the connection to the Light Guide (LG). Two guiding holes per connector for precise alignment of connector and LG. The connector ring does not provide any alignment for this connection.

Table 4.6: *Precision measurement of barrel dimensions conducted at DESY.*

barrel	barrel diameter		centre offset	
	nominal value (mm)	actual value (mm)	x (mm)	y (mm)
inner	218.00	218.425	0.0	0.0
outer	374.70	375.115	0.176	-0.145

electron beam line at DESY T22 was devised [56]. Utilising an existing reference tracking system consisting of three silicon microstrip detectors, fibre positions can be determined with a spatial resolution of $80\,\mu m$ to $130\,\mu m$ depending on the barrel orientation. Each fibre position is then reconstructed and parametrised by a fourth order polynomial. A modest displacement of the fibres in the centre of a module of $100\,\mu m$ with respect to the endpoints was found [56], which can be accounted for in later tracking applications with the parametrised fibre position.

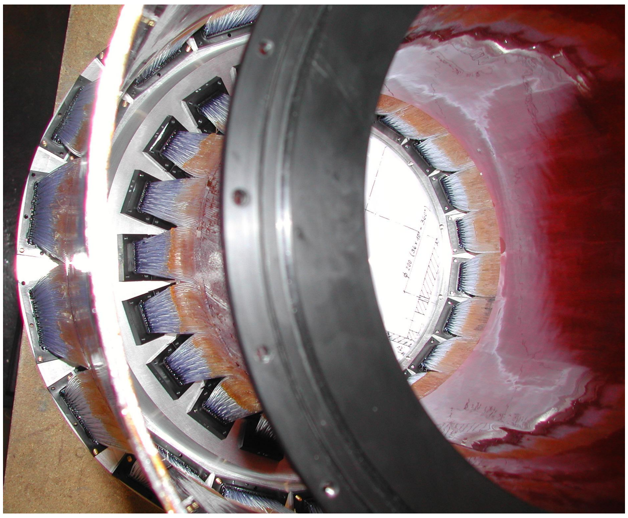

Figure 4.18: *Integration of outer barrel. Inner barrel already fitted with endcap.*

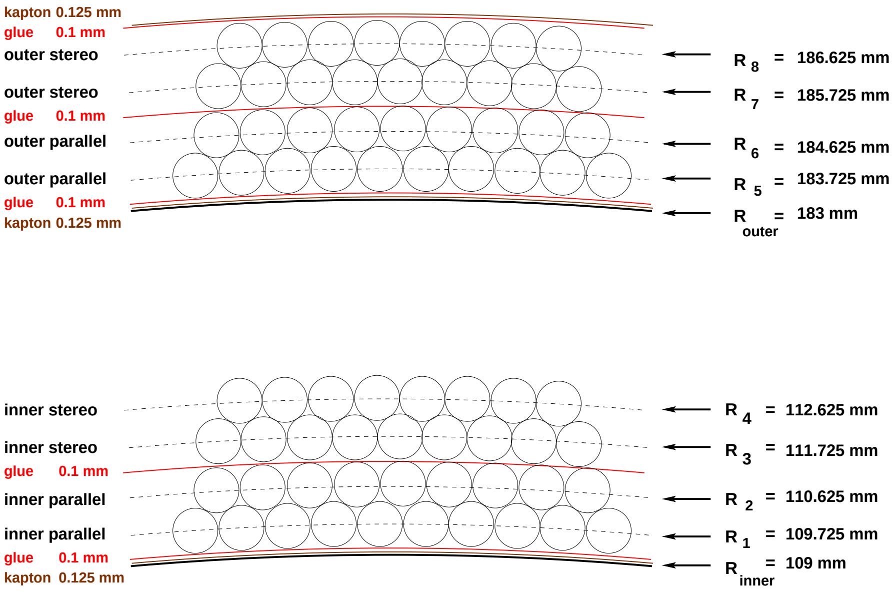

Figure 4.19: *Schematic cross section of SFT barrels and corresponding nominal values.*

The SFT was finally equipped with a Gain Monitoring System (GMS) (see fig. 4.20) to monitor LG and MAPMT characteristics over time. The GMS consists of a light source utilising Light Emitting Diodes (LED) [47] and clear fibres guiding the light to the SFT and injecting it into the scintillating fibres. The resulting signal is used to monitor the MAPMT performance [55].

As a last step, the SFT has to be integrated into the Recoil Detector setup. This requires custom-made tools as space and accessibility are limited in the ex-

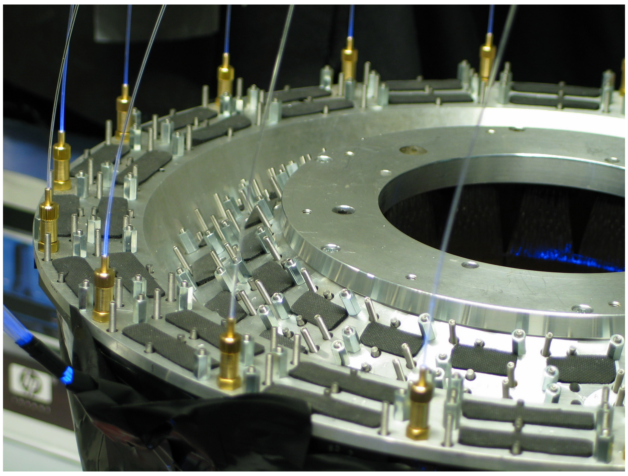

Figure 4.20: *Gain Monitoring System (GMS) fibres connected to SFT.*

perimental area. The SFT is mounted only after the magnet including the Photon Detector (PD) is installed and aligned with respect to the scattering chamber. A special mounting tool was designed to accommodate the SFT, align it with respect to the scattering chamber and slide it into position, see fig. 4.21 a, inside the PD. After dismantling the mounting tool, the SFT is screwed to the scattering chamber retaining its centred position, see fig. 4.21 b. The SFT endcap rests on a downstream pump cross flange recess. The SFT is then sealed light tight with foam rubber against the PD from up- and downstream end.

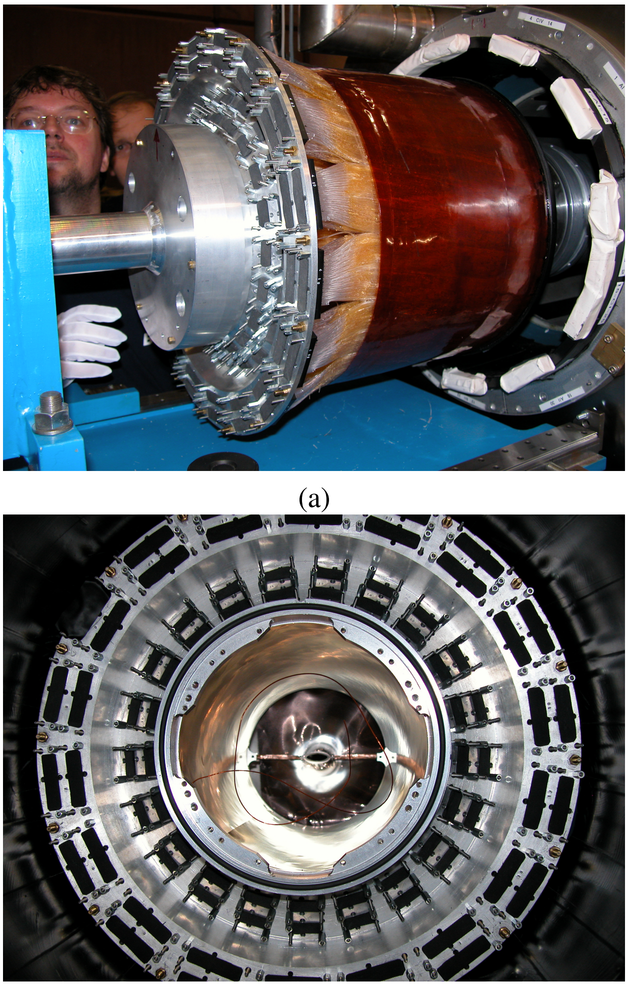

(a)

(b)

Figure 4.21: *Final installation of the Scintillating Fibre Tracker (SFT) into Recoil Detector setup:*
(a) SFT mounted to installation mounting tool which is aligned with respect to the scattering chamber;
(b) SFT integrated into Recoil Detector setup and screwed to scattering chamber. Interior of scattering chamber visible, Silicon Strip Detector (SSD) not yet installed. Protective caps put on SFT connectors, therefore no fibres visible.

4.2 Performance of SFT Prototype Modules

In the following section a test experiment is described, which was conducted at the GSI accelerator facility at Darmstadt to verify that the design of the SFT meets the requirements.

A secondary beam-line was set up at the SIS 18 Tm synchrotron at GSI [57] which enables experiments with mixed particle beams of either polarity over a wide momentum range. The secondary beam is produced in the collision of a primary proton or heavy-ion beam from the SIS with a production target. Throughout the test experiment period a B_4C production target with a thickness of 120 mm was employed.

The beam line optics allows for a selection of discrete momenta by varying its $B\rho$ value. The momentum acceptance window is in the order of 10% [57]. During the test experiment 4 different $B\rho$ settings were used, corresponding to central momenta of 300, 450, 600 and 900 MeV/c. The polarity of the beam-line is chosen to select positively charged particles. Thus the delivered beam consisted mainly of pions and protons, the fraction of other particles including kaons, deuterons and ^{4}He is negligible [57]. The SFT test experiment setup was located at Cave A, see fig. 4.22.

The main focus of this test experiment was the study of detection efficiencies for different particle types and the extraction of energy response functions in the face of PID capabilities. Basic tracking studies are performed as well, but with limited precision only because an independent high-precision tracking system was lacking. In addition, different settings in the front-end electronic were tested to determine its final lay-out. Moreover the noise and crosstalk conditions are studied to determine a proper threshold for a following data analysis.

4.2.1 Test Experiment Setup

A schematic drawing of the setup in cave A is shown in fig. 4.23. The setup consists of three plastic scintillators (S0, S1 and S2) providing a trigger for the readout electronics and timing information for an independent PID, a Multi Wire Proportional Chamber (MWPC) for beam position monitoring and a small plastic scintillator bar (S3) for efficiency measurements. Additionally to the SFT, prototype modules of the other sub-detectors of the Recoil Detector were installed. Results from the PD and the SSD are not discussed in this work. For this test experiment, 4 SFT prototype modules were mounted in one holding frame, see fig. 4.24. Two of the modules had a parallel orientation whereas the other two were crossed under an angle of 10° with respect to fibre axis of the parallel modules. A parallel and a stereo module were combined to a unit, emulating the inner and outer barrel of the SFT. The distance between these two units is approximately 6 cm similar to the final SFT configuration.

Each SFT module was coupled to a MAPMT via 4 m long LG, which were made of Kuraray clear fibres. The module setup and connection to the MAPMT

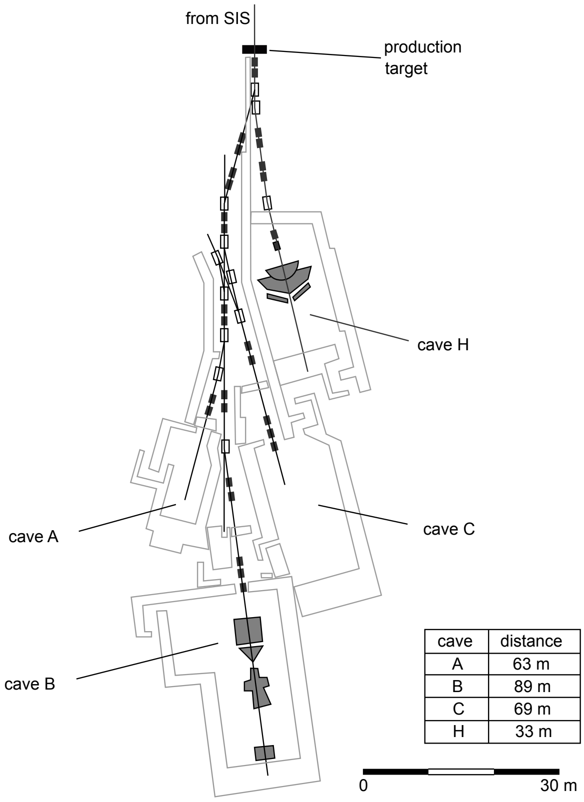

cave	distance
A	63 m
B	89 m
C	69 m
H	33 m

Figure 4.22: *Floor plan of GSI target hall. The B_4C production target is indicated at the top. The secondary beam is transferred via beam lines, which enable a momentum selection, to the individual experimental areas. The SFT test experiment setup was located at Cave A.*

resembles the final detector arrangement in as much detail as possible.

Concerning the readout electronics this test experiment was used to determine the capacity setting of the CDC.

Altogether 4 different CDC configurations were tested, such that each MAPMT had its unique CDC. The PMTs were operated at different high voltages, to set the gain of each MAPMT to a comparable ADC value (cf. tab. 4.7). In any case, no hardware threshold on the MAPMT signal was introduced in order to study the dependence of the SFT performance on an applied threshold later on in the following analysis.

The necessary Low Voltage (LV) for the PFMs was provided by an alternative power supply since the final system was not operational at that time. In contrast to the final system, no stabilisation and continuous monitoring of the LV output was possible. A changing LV output, which was observed during the test experiment, may cause pedestal drifts but does not influence the linearity nor the calibration of the ADC [58]. The LV was distributed to the four PFMs via two backplanes.

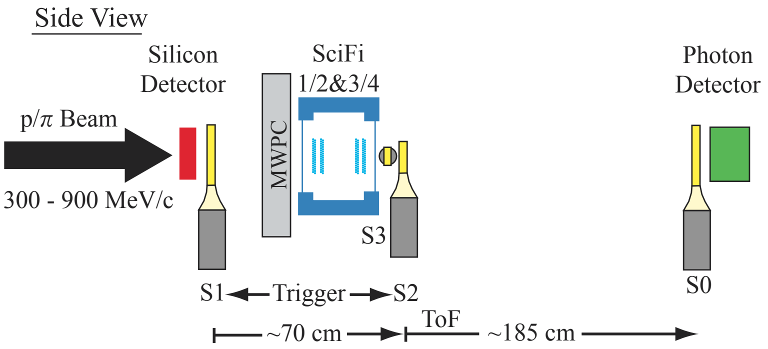

Figure 4.23: Schematic drawing of the GSI test experiment setup indicating the position of all subdetector prototype modules. The secondary beam enters from the left. The scintillators (S0, S1 and S2) are used for triggering and Time-Of-Flight measurement. Scintillator S3 is employed for efficiency determination of the Scintillating Fibre Tracker (SFT) prototype modules. The Multi-Wire Proportional Chamber (MWPC) provides position measurements.

Figure 4.24: Holding frame with mounted SFT modules, side walls removed. For final operation, side open side walls are covered by light-tight black tape.

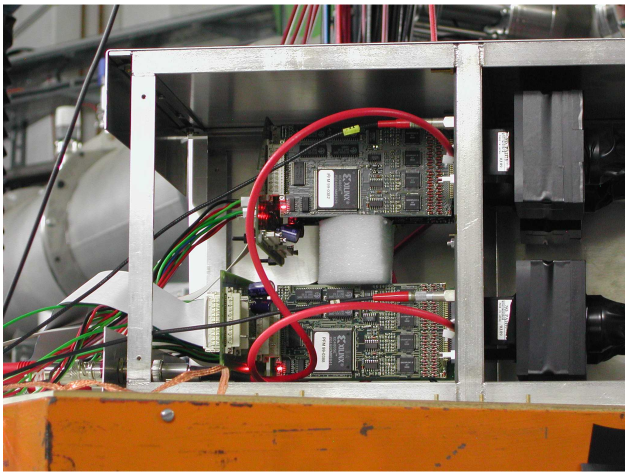

Figure 4.25: Multi-Anode Photo-Multiplier Tube (MAPMT) holding frame with 4 MAPMTs and attached Preprocessing Frontend Module (PFM) cards.

The main trigger system consisted of the plastic scintillators S1 and S2, see fig.4.23, which were read out by fast PMTs. A coincidence between S1 and S2

Table 4.7: *Mean gain factor G_{mean} given in ADC channel, for each Charge Divider Circuit (CDC) and High Voltage (HV) setting of the four Multi-Anode Photo-Multiplier Tubes (MAPMT) used during the GSI test experiment. Averaging over all 64 channels of a MAPMT yields G_{mean}.*

PM no	G_{mean}	CDC capacity (pF)	high voltage (V)
1	20.15 ± 0.56	100	880
2	19.29 ± 0.55	220	940
3	20.07 ± 0.56	330	970
4	13.99 ± 0.50	470	1000

was used to trigger the readout electronics, cf. fig. 4.26.

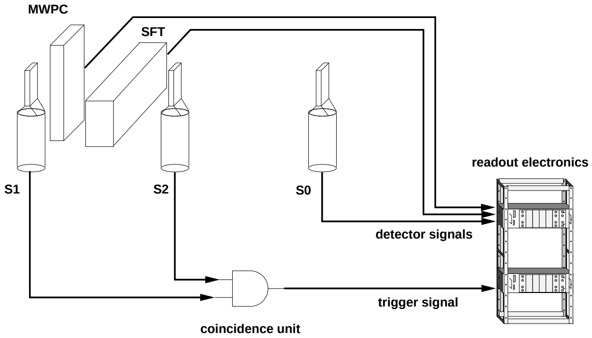

Figure 4.26: *Test experiment trigger scheme. The scintillators S1 and S2 are used to form the trigger. Scintillator S0 is used in addition to maximise the path length for Time-Of-Flight (TOF) measurements.*

Apart from providing a trigger, the scintillators had to supply sufficient information to separate pions and protons present in the beam. PID is achieved via Time-Of-Flight (TOF) measurement between the trigger scintillators S1 and S2 and the energy loss dE in these scintillators. Scintillator S2 provided the timing reference for TOF measurements. For momenta above 300 MeV/c also scintillator S0 could be integrated into the TOF measurements, thus enhancing the PID. For a beam momentum of 300 MeV/c, S0 could not be employed since the protons are stopped inside S2.

Especially for extracting detection efficiencies, a scintillator bar (S3) with a thickness of 5 mm was installed immediately behind the SFT modules (see fig. 4.27). The acceptance of S3 is smaller than the geometrical size of the SFT modules, therefore no correction needs to be applied when the efficiencies are extracted. This scintillator is only employed for protons above 300 MeV/c, since otherwise

---

[16] path length $0.9m$

Table 4.8: *Time-Of-Flight (TOF) for pions and protons between first (S1) and last (S0) trigger scintillator (path length $3\,m$) for all central momentum settings.*

momentum [MeV/c]	$\mathrm{TOF}_{\mathrm{pion}}$ [ns]	$\mathrm{TOF}_{\mathrm{proton}}$ [ns]
300^{16}	3.31	9.88
450	10.48	23.14
600	10.27	18.58
900	10.13	14.46

they are stopped inside S3 and no trigger will be formed.

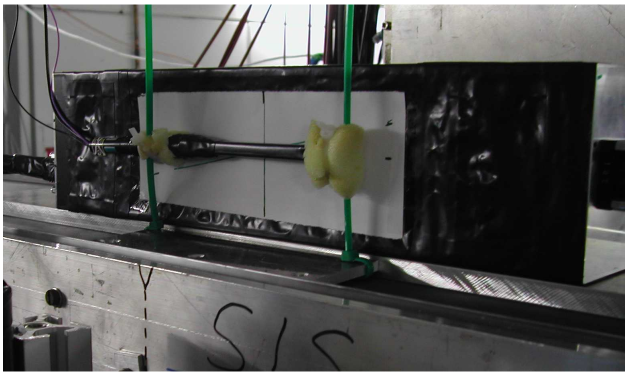

Figure 4.27: *Installation of scintillator S3 behind Scintillating Fibre Tracker (SFT) module frame. S3 was used to determine the detection efficiency of the SFT modules.*

A MWPC was installed in front of the SFT setup . The gas mixture of the MWPC consisted of 86% Argon and 14% CO_2. The MWPC served as beam position monitor. The wires of each plane are read out via a delay-line. This readout mode limits the particle rate to about 100 kHz but enables the selection of single particles traversing the set-up.

4.2.2 Preparing Raw Data

In order to analyse the test experiment data, the raw data need to be processed. This includes calibration of readout channels, applying advanced algorithms to cope with crosstalk and noise and to apply cuts. The necessary procedures are described in this section.

PMT Calibration

All MAPMT channels were calibrated according to their Single Photo Electron (SPE) peak. This was achieved by flashing the MAPMT cathode with low intensity blue light emitted by a LED. The obtained spectra are then fitted with calibration functions (see fig. 4.28) similar to the procedure described in [59]. It has to be noted that, due to the PFM readout logic, the spectra are reversed; i.e. high ADC values correspond to a small MAPMT signals.

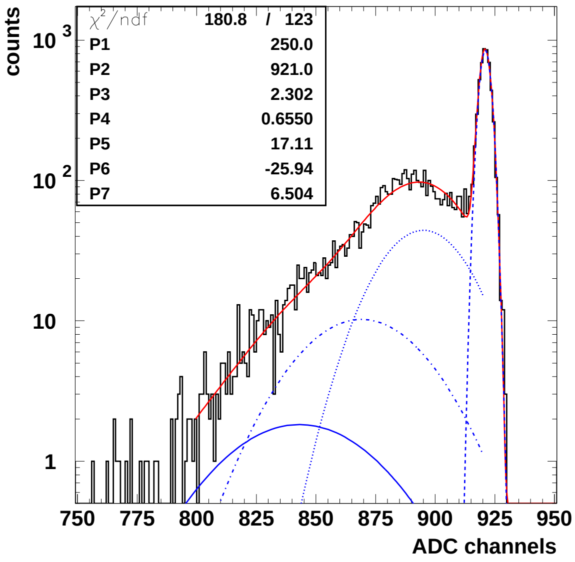

Figure 4.28: *Fit of the calibration function to a single Multi-Anode Photo-Multiplier Tube (MAPMT) channel spectrum obtained by low level LED illumination. Due to the readout logic high ADC values correspond to low MAPMT signals. The blue curves display the pedestal and the 1-, 2- and 3-photo electron (p.e.) contributions of the spectrum.*

This initial calibration was then cross-checked with test experiment data and corrected, if necessary. The accuracy of this calibration method was estimated to be approximately 10%. Additionally, it was found that the signal overflow handling was erroneous (see fig. 4.29 a), possibly due to the Data AcQuisition (DAQ) software or unstable LV supply [60, 61], leading to electronic crosstalk. On this account an overflow cut was introduced into the analysis software, rejecting signals of 50 ADC channels above the lower ADC boundary. A finally calibrated single MAPMT channel spectrum is shown in fig. 4.29 b.

Cluster Algorithm

Since optical crosstalk in MAPMTs cannot be avoided, it is necessary to correct for this effect since it may lead to wrong tracking information from the SFT modules and alters the energy response. Due to this crosstalk adjacent MAPMT channels, also called pixels, share the incident light of a single fibre channel and form a so-called cluster. The aim of a Sophisticated Cluster Algorithm (SCA) is to find these clusters and characterise them by their size (i.e. the number of pixels they contain) and their total energy information. Should there be no other light source (i.e. a

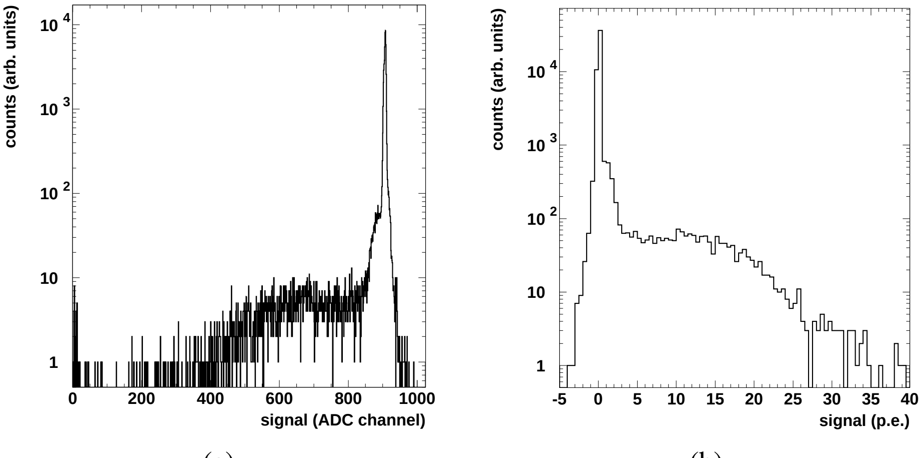

(a) (b)

Figure 4.29: Comparison of uncalibrated and calibrated Scintillating Fibre Tracker (SFT) channel:
(a) Uncalibrated spectrum of a single SFT channel. On the lower ADC boundary the effect of erroneous overflow handling can be seen;
(b) Spectrum of same SFT channel employing Single Photo Electron (SPE) calibration and including overflow suppression.

second hit fibre close by) the cluster size is solely determined by the amount of optical crosstalk.

To avoid the problem of clusters overlapping, this algorithm does not apply a fixed cluster template, but seaches for areas of adjacent MAPMT pixels (see fig. 4.31 b) which show a signal above a certain threshold which can be set by the analysing software. These areas are then grouped into a cluster and the characteristics of this cluster are calculated. The SCA starts its cluster search at the MAPMT channel with the largest signal, continuing in a descending order until all channels above threshold are processed.

The MAPMT pixel initiating the cluster search (red pixel in fig. 4.31 b) is defined as cluster centre. The cluster centre determines the fibre channel hit in a SFT module. The total cluster energy is then assigned to this fibre channel. The information on which fibre channel is hit and energy deposition is utilised further in the data analysis.

Large clusters may lead to inaccurate tracking information, since both fibres hit may be contained in one cluster and only the position information of the larger signal is used. The advanced feeding scheme used for the MAPMT connector (see fig. 4.31 a and appendix A.1) minimises the probability of merging the clusters of 2 adjacent fibres. But in the case of large amounts of crosstalk this behaviour can be observed (cf. fig. 4.32) altering the energy response and degrading the tracking information. Thus he SCA was complemented with a routine to disentangle merged clusters. For clusters consisting of more than two pixels, an average background value $\langle S_{BG} \rangle$ is calculated from all but the highest two signals and compared to to

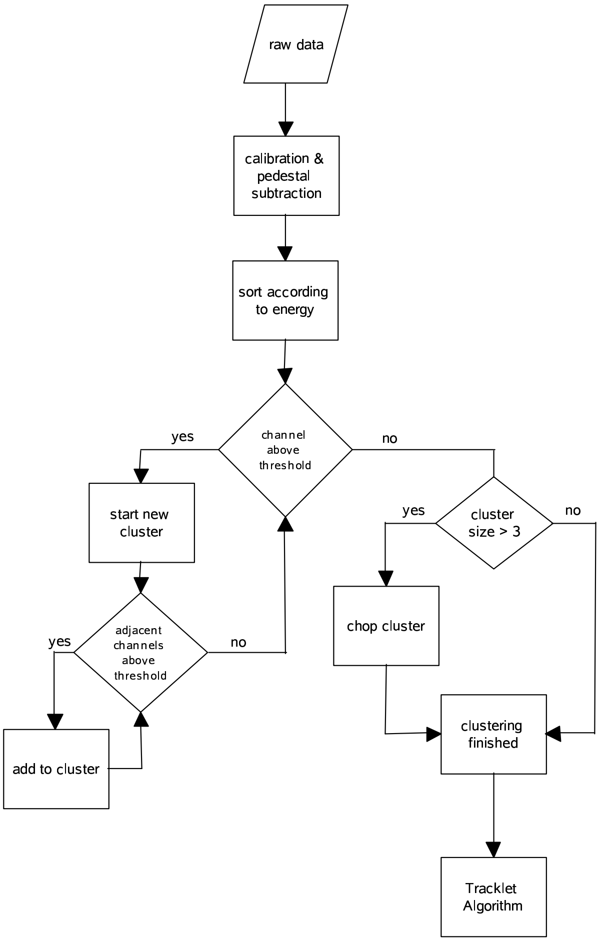

Figure 4.30: *Flowchart of the Sophisticated Cluster Algorithm (SCA).*

the second largest signal S_2 in the cluster. From the ratio

$$R = \frac{S_2}{\langle S_{BG} \rangle} \tag{4.10}$$

a threshold for the cluster splitting can be determined after contributions from ordinary cross talk have been subtracted. The effectiveness of this routine is shown in fig. 4.32.

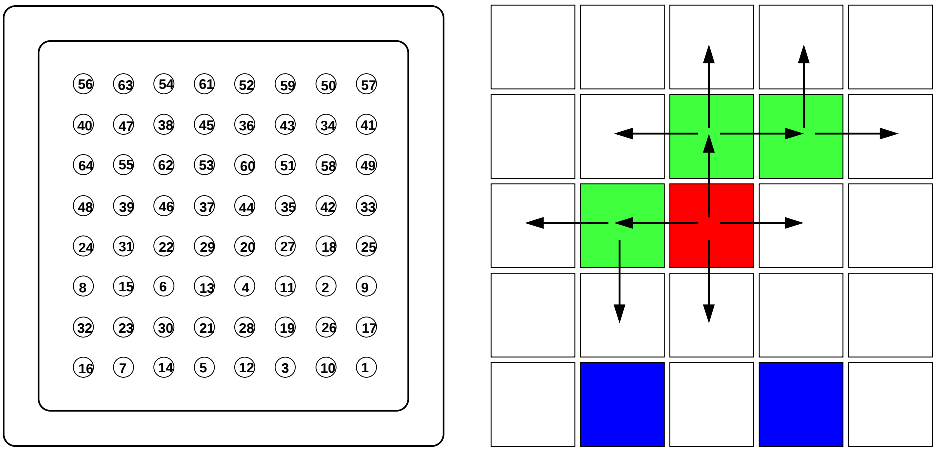

(a) (b)

Figure 4.31: *Ingredients of the Sophisticated Cluster Algorithm (SCA):*
(a) Mapping of Scintillating Fibre Tracker (SFT) channels on Multi-Anode Photo-Multiplier Tube (MAPMT) cathode. Odd (even) numbers correspond to fibres in the lower (upper) layer of a module;
(b) Cluster algorithm search principle on MAPMT cathode. The pixel in the central position (red) denotes MAPMT channel corresponding to hit fibre, the surrounding, coloured pixels (green) denote crosstalk channels. The marked pixels (blue) in the bottom row are neighbouring SFT fibre channels, cf. part (a) of this figure.

Tracklet Algorithm

After a particle traversed a SFT module, the SCA is used to accommodate crosstalk on the MAPMT cathode. The fibres indicated by this algorithm as being hit are then grouped into tracklets by a Tracklet Algorithm (TA) if they were adjacent in the SFT module. The TA search starts at the fibre with the largest signal and processes all fibres indicated by the SCA in a descending order. A fibre which initiates the TA search is called a tracklet centre. An important quantity of a tracklet is its size in terms of fibre channels, since crosstalk between fibres can enhance the tracklet size. As depicted in fig. 4.33, the ideal tracklet consists of two fibres, one from each layer. But it is of course possible for tracklets with two fibres, to have both fibres located in one layer. This can be attributed to crosstalk inside an SFT module. These two kinds of tracklets need to be distinguished for tracking purposes. Since only basic tracking studies can be performed with the given set-up, this tracklet distinction is neglected.

Tracklets consisting of only a single fibre can occur when a particle hits the module near a fibre centre. Due to the staggered configuration, such a particle would not enter a fibre from the other layer or penetrate only its edge and therefore produce merely a signal below threshold. Also tracklets of this size can be the result of crosstalk inside the light guide connectors or the SFT module.

The next step after finding and combining hit fibres into tracklets, is to deter-

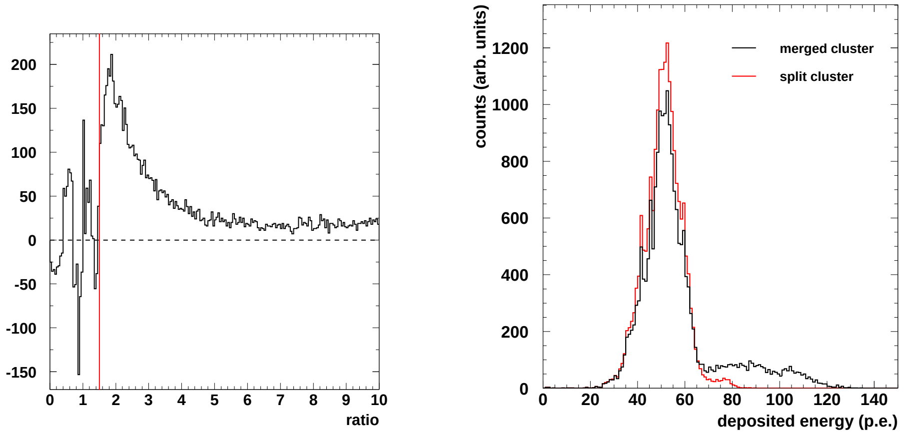

(a) (b)

Figure 4.32: *Determination of basic parameters for the cluster splitting routine and its impact on the energy response function.*
(a) Determination of cluster splitting threshold. Ratio is determined by the signal in the second largest signal in the cluster and the averaged background in the remaining channels of the cluster. After subtraction of real crosstalk, an excess due to cluster merging becomes visible, starting at a ratio of 1.5;
(b) Impact of merged cluster onto energy response and effectiveness of cluster splitting routine.

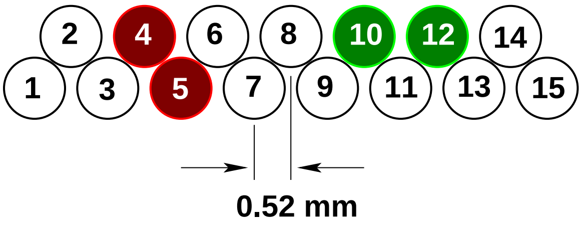

Figure 4.33: *Tracklet algorithm scheme. Red fibres display an ideal tracklet, whereas the green tracklet, a so called partial tracklet, is due to crosstalk.*

mine the overall deposited energy, which is essential for applying PID algorithms [62]. For space point reconstruction it is necessary to know the deposited energy per fibre.

4.2.3 Data Analysis

In the following, event selection cuts based on trigger scintillator informations are described. Furthermore the optimal threshold setting for cluster and tracklet algorithms is determined and sources of electronic crosstalk investigated.

Event Selection

Event selection is based on the PID information of the trigger scintillators and reconstructed beam position, employing the MWPC. The necessary cuts for achieving this are described in the following:

For the trigger scintillators S1 and S2 in addition to TOF, the deposited energy dE was recorded as well. Whenever possible, the TOF information of S0 was included to maximise the flight path length. To use the energy information of the trigger scintillators together with TOF for particle identification, the sum of the deposited energy in both trigger scintillators was calculated. A strong correlation between the deposited energy in S1 and S2 was observed.

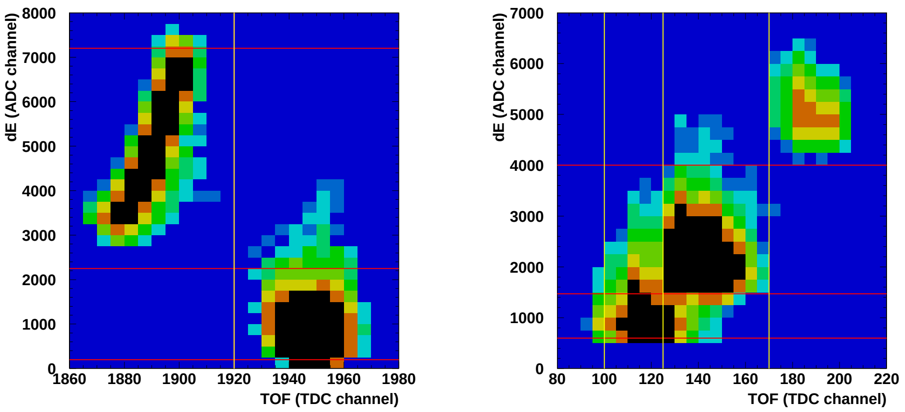

(a) (b)

Figure 4.34: *Particle IDentification (PID) cuts for trigger system. Shown are the cuts applied to the Time Of Flight (TOF) measurement (yellow) and to the deposited energy dE (red);*
(a) at 300 *MeV/c pions and protons are well separated, protons in the upper left corner and pions in the lower right corner;*
(b) at 900 *MeV/c pion and proton signals are close by, pions in the lower left corner and protons in the middle. In addition contributions from heavier particles are recognised in the upper right corner.*

Cuts on TOF and dE are applied to separate pions from protons. Additional heavier particles present are neglected. As an example, the applied cuts for the lowest and highest momentum setting of the test experiment are shown in fig. 4.34. Obviously, the separation of protons and pions depends heavily on the momentum, e.g. the difference in TOF is reduced significantly (cf. tab. 4.8) even for a flight path of approximately 3 m. For a beam momentum of 300 MeV/c, pions and protons are well separated, whereas at 900 MeV/c a distinct overlap is present. In addition, contributions of heavier particles can be observed which are missing at the lower momentum settings. This simple box cut is nevertheless sufficient to obtain pure particle samples. The accompanying loss of statistics is acceptable, since sufficient statistics for each particle type were accumulated.

A reasonable particle track position as reconstructed by the MWPC is required to accept an event. Since a delay-line readout was employed the track position is determined by the different timing information on any given wire of the MWPC. The delay-line technique is based on the fact that each wire is connected to delay-lines on both ends and the signals propagate through a left and right delay-line and deliver a stop signal for a Time-to-Digital Converter (TDC). The start signal for the TDC is derived from the MWPC anode. The time difference between the left and right side of the delay-line yields the position whereas the sum of both sides should be constant (being determined by the total length of the delay-line).

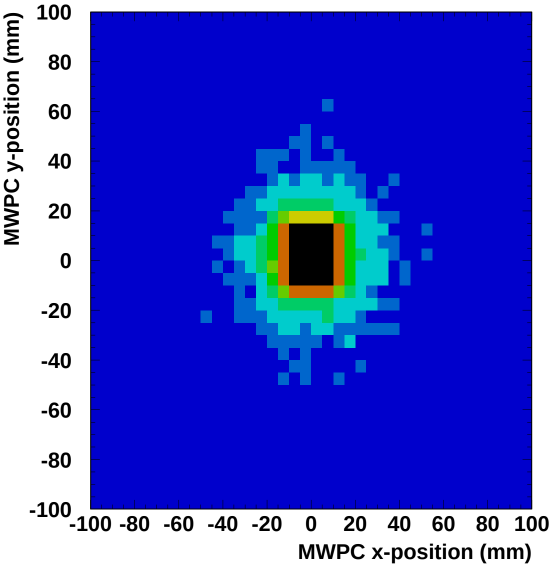

Figure 4.35: *Particle track position measurement with Multi-Wire Proportional Chamber (MWPC) with all selection cuts applied.*

Events with high particle multiplicities, i.e. at least two particles hit the MWPC at the same time, thus rendering any position information useless. Therefore a reconstructed MWPC space point in x- and y-coordinates above -2000 mm is required. This also ensures that only one particle traverses the set-up, which is essential for the following efficiency and tracking studies. The resulting beam profile is shown in fig. 4.35, the spot size corresponding to the size of the trigger scintillator S2.

During the analysis of cluster sizes for various momentum settings, a strange behaviour of all four MAPMTs at 300 MeV/c and 600 MeV/c was noticed, namely an accumulation of events with large clusters ($\geq$ 40 pixels) (see fig. 4.36 a) regardless of the PID information. The energy of such clusters corresponds to approximately 1 p.e. per pixel. Since crosstalk seems to be very unlikely, it was investigated whether there might be a correlation of such events.

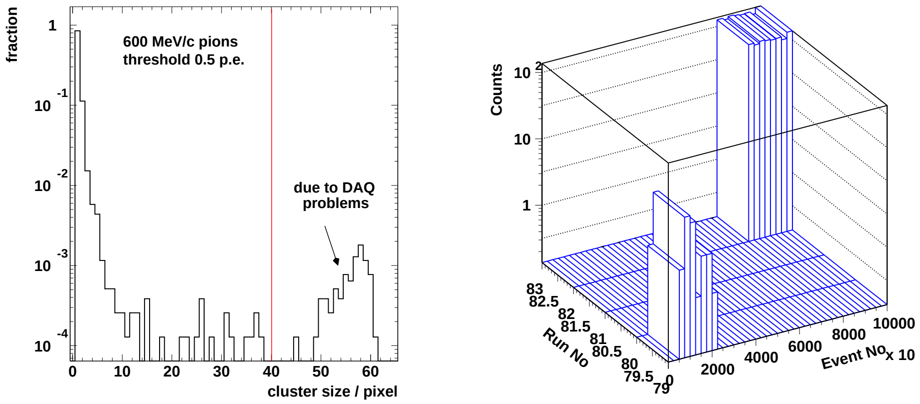

(a) (b)

Figure 4.36: *Correlation of Data AcQuisition (DAQ) problems to large cluster events:*
(a) Example of large cluster sizes due to DAQ problems, pions of 600 *MeV/c, threshold corresponding to* 0.5 *p.e., SFT 1 ;*
(b) Distribution of events with large clusters ($\geq$ *40 pixels) for* 300 *MeV/c for different runs.*

In the case that such events occurred during a run, all were found either at the beginning or at the end of a run (see fig. 4.36 b) implying problems with the DAQ software. In total three runs exhibiting such problems were found and accordingly excluded from further analysis.

The total accumulated statistics after applying all event selection and data quality cuts, are shown in tab. 4.9.

Table 4.9: *Accumulated statistics for all beam momenta.*

P$_{beam}$ [MeV/c]	total no of events pion	total no of events proton	ratio $\frac{N_\pi}{N_{proton}}$
300	172,316	30,823	5.59
450	69,462	9,897	7.02
600	21,807	125,818	0.17
900	10,564	129,553	0.08

Determining the Threshold

The data were analysed with different threshold settings equivalent to 0.2, 0.5, 1.0 and 1.5 photo electrons (p.e.). This was possible since the data were taken without any imposed hardware threshold. It is of particular interest to find a suitable threshold for all beam momenta, suppressing any optical as well as electronic crosstalk and noise to an acceptable level. Apart from noise, all crosstalk sources should depend on the deposited energy and thus on beam momentum and particles species.

Cluster reconstruction can be influenced by crosstalk on the MAPMT cathode or by electronic noise, increasing the size of a cluster. The multiplicity of clusters might be enhanced due to crosstalk inside the SFT modules or the light guides (see fig. 4.37). The next step after reconstruction of all clusters, is forming tracklets out of the cluster information. As shown in fig. 4.37 crosstalk may contribute to trackletmultiplicities and size. By analysing the four variables shown in the last line of fig. 4.37, it might be possible to disentangle the sources of crosstalk.

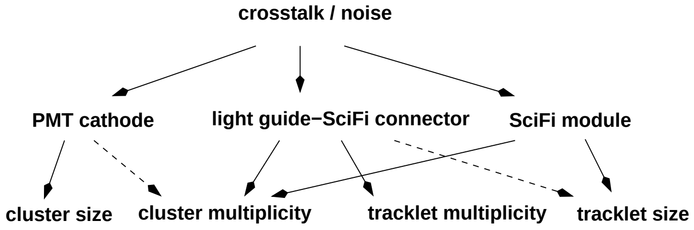

Figure 4.37: *Crosstalk and noise sources and their relation to cluster and tracklet properties, influence of secondary importance indicated by dashed line.*

Between the individual SFT modules no coincidence was demanded, therefore the total number of events registered for each module can differ slightly. Throughout this section mostly plots for PMT 1 will be shown as examples, if all PMTs behave similar. Results for all PMTs can be found in [64].

Studying the cluster size provides a unique possibility to access crosstalk and noise on the PMT, since only this variable is unbiased by any algorithm used during analysis. The cluster multiplicity, for instance, can be suppressed in case of large cluster sizes. The ideal cluster size would be 1 MAPMT pixel, but can be influenced by crosstalk and noise. A cluster size of ≥ 4 pixels might influence tracklet reconstruction and should therefore be suppressed by the imposed threshold.

As shown in fig. 4.38, the fraction of events with large cluster sizes (≥ 4) depends on the applied threshold. For pions this fraction is independent of the beam momentum, as anticipated for Minimum Ionising Particles (MIP), but for protons a distinctive correlation even for a threshold of 1.5 p.e. is visible.

For pions a threshold of 0.5 p.e. already reduces the fraction of events with large clusters to about 1%. Raising this threshold above 1.0 p.e. does not yield any substantial reduction. The situation for protons is quite different. First of all, the fraction of large cluster events depends strongly on the beam momentum, and due to the larger energy deposition (see fig. 4.49) a crosstalk enhancement is anticipated. The momentum dependence can be observed for any of the applied thresholds, save for momenta above 450 MeV/c the difference between a 1.0 p.e and 1.5 p.e threshold is negligible. For a momentum of 300 MeV/c at least 5% of the events include large clusters and this fraction rises rapidly for thresholds lower

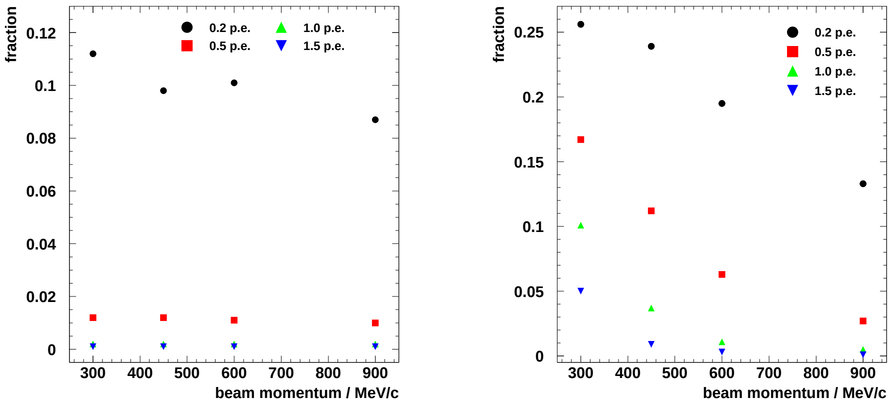

(a) (b)

Figure 4.38: *Fraction of events with cluster sizes* ≥ 4 *for different beam momenta, extracted for all thresholds, PMT 1 only;*
(a) in case of pions and (b) in case of protons.

than 1.5 p.e.

Another important figure is the maximum cluster size, since very large clusters ranging up to 64 pixels are expected to originate from noise, which should be suppressed by a suitable threshold.

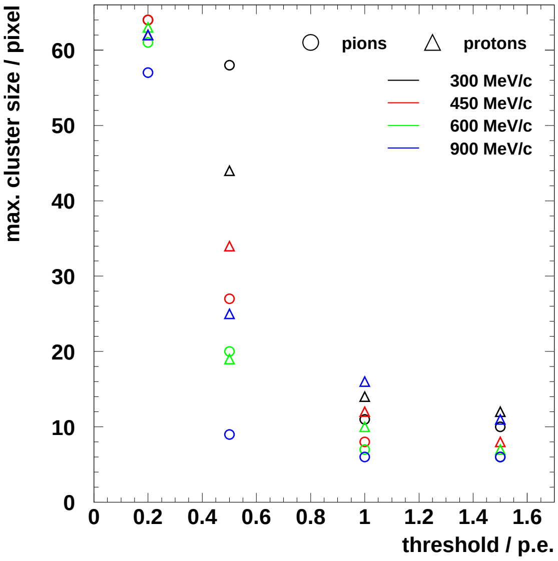

Figure 4.39: *Maximum cluster size in pixel for pions and protons for various thresholds, momentum setting indicated by colour, PMT 1 only.*

In fig. 4.39 the variation of the maximum cluster size observed for pions and protons at various momenta for different thresholds is shown. For a 0.2 p.e. threshold cluster containing more than 55 pixel are found for both particle types at all momenta, indicating large noise contributions to the cluster size. Raising the threshold to 0.5 p.e. already reduces the maximum cluster size, but depends heavily on the beam momentum for pions and protons which still indicates noise contributions (although they are already largely suppressed for pions, cf. fig. 4.38). It may be that the momentum dependence of the maximum cluster size for pions stems from a proton contamination of the pion sample. Increasing the threshold obviously prevents large cluster sizes completely, indicating a thorough noise suppression. Again increasing the threshold further to 1.5 p.e. does not yield a substantial improvement. Therefore an appropriate noise threshold most probably has to be set between 0.5 p.e. and 1.0 p.e.

Studying cluster multiplicities might shed some light on crosstalk inside the SFT modules and the SFT-light guide connection. Without crosstalk, a cluster multiplicity of 1 – 2 clusters is anticipated. As mentioned previously, large cluster sizes influence the multiplicity distribution. Regarding the results obtained by analysing the cluster size, only thresholds above 0.2 p.e. are taken into account. For a proper comparison the data are normalised such that the number of events with at least one cluster correspond to each other.

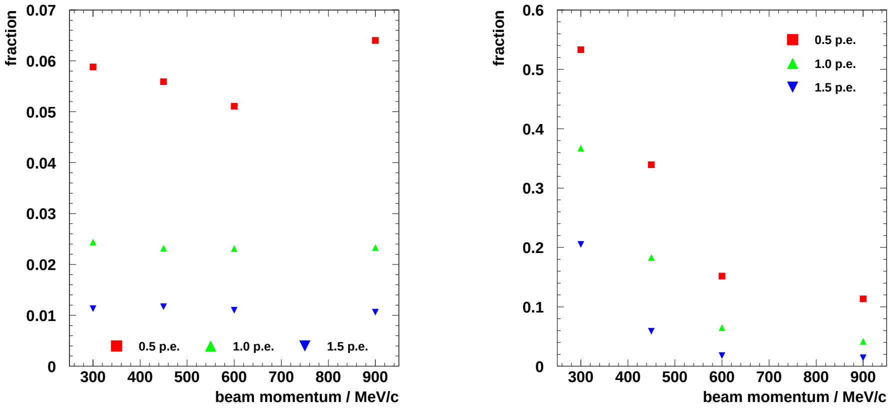

(a) (b)

Figure 4.40: *Dependance of large cluster multiplicities ($\geq$ 4 clusters) on momentum, extracted for various thresholds, PMT 1 only;*
(a) for pions and (b) for protons.

The class of events with large cluster multiplicities, i.e. more than 3 clusters, is analysed. The fraction of these events is shown in fig. 4.40 for pions and protons. The result is similar to the cluster size analysis, pions exhibit no dependence on momentum, whereas protons again show a strong correlation. The strange behaviour of pions for a 0.5 p.e threshold is probably due to large clusters leading to a suppression of higher multiplicities (cf. fig. 4.38 and 4.39). In general, the abundance of events with large multiplicities is enhanced compared to events with large clusters, indicating a larger fraction of crosstalk inside the SFT modules or light guides. Even for the highest threshold, for approximately 20% of the events 4 or more clusters are reconstructed for protons at 300 MeV/c, pointing to a substantial crosstalk well above this threshold.

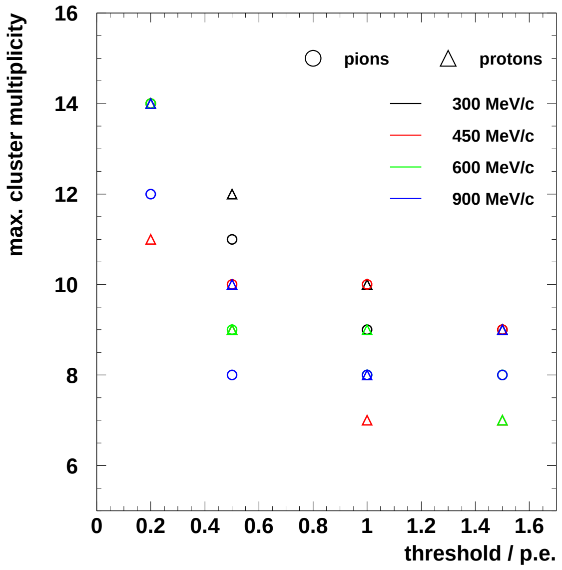

Figure 4.41: *Variation of maximum cluster multiplicity with threshold for all momenta (momentum indicated by colour), PMT 1 only.*

It is also of interest to study the dependence of the maximum observed cluster multiplicity on the beam momentum and the applied threshold. Any event with more than two reconstructed clusters is due to crosstalk, since the MWPC cut ensures that only single particles traverse the modules. Results are shown in fig. 4.41, but in contrary to the cluster size, the cluster multiplicity is only weakly correlated with the threshold, at least above 0.2 p.e. Again the difference between 1.0 p.e. and 1.5 p.e. does not justify increasing the threshold to this level.

The tracklet multiplicity is mainly connected with crosstalk in the light guide-SFT connector. To discriminate between crosstalk sources, events with more than two reconstructed tracklets are selected. False identification of a cluster due to crosstalk on the MAPMT cathode may lead to an additional tracklet but more than one additional tracklet is most likely caused by crosstalk inside the light guide-SFT connector.

Once again the different level of crosstalk for pions and protons (see fig. 4.42) is noticeable. At a threshold of 0.5 p.e. a variation with momentum visible for pions, which is not understood (especially the rise at higher momentum) but it

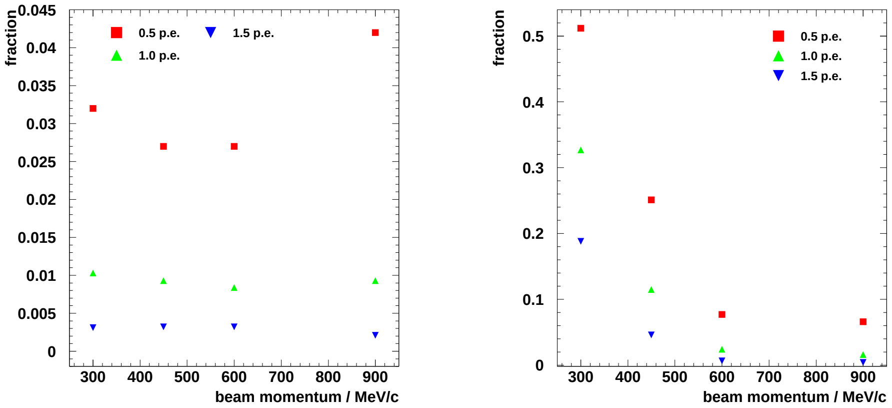

(a) (b)

Figure 4.42: *Fraction of events with tracklet multiplicity ≥ 3 for all beam momenta, extracted with different thresholds, PMT 1 only;*
(a) for pions and (b) for protons.

is similar to the behaviour of the cluster multiplicity, see fig. 4.40. Otherwise for protons a distinct correlation with momentum for all thresholds is seen. At low momenta a substantial fraction of events with large tracklet multiplicities is noticeable for protons, even for a threshold of 1.5 p.e., indicating crosstalk well above this threshold inside the light guide-SFT connector.

In general the distribution of large tracklet multiplicities is related to the cluster multiplicity, pointing to crosstalk originating from the same source. Crosstalk enhancing the cluster multiplicity originates inside the SFT modules between adjacent fibres [33] and also, to some extent, in the light guide-SFT connector [63]. Crosstalk at the mirrored end faces can be neglected.

In general, the level of crosstalk inducing large tracklets (≥ 4 fibres) is highly reduced compared to large tracklet multiplicities (compare fig. 4.43 and 4.42) which is anticipated due to the feeding scheme [63] and the nature of crosstalk between adjacent fibres [33]. Again the characteristic dependence on momentum for protons can be seen (see fig. 4.43) pointing to crosstalk related to the energy deposition of particles traversing the fibres. For pions, since they are MIPs, no such correlation can be seen (cf. fig. 4.43). The level of crosstalk in the threshold regime between 0.5 p.e. and 1.0 p.e. is below 1% for pions and below 3% for protons at 300 MeV/c but decreasing to 1.5% at 900 MeV/c.

Electronic Crosstalk

Some features of the observed crosstalk cannot be explained by optical crosstalk. Therefore a closer look to the front-end electronics is necessary, especially if any influence is correlated with the signal height, since four different CDCs for the MAPMTs were used. For a conservative estimate of this kind of crosstalk, the

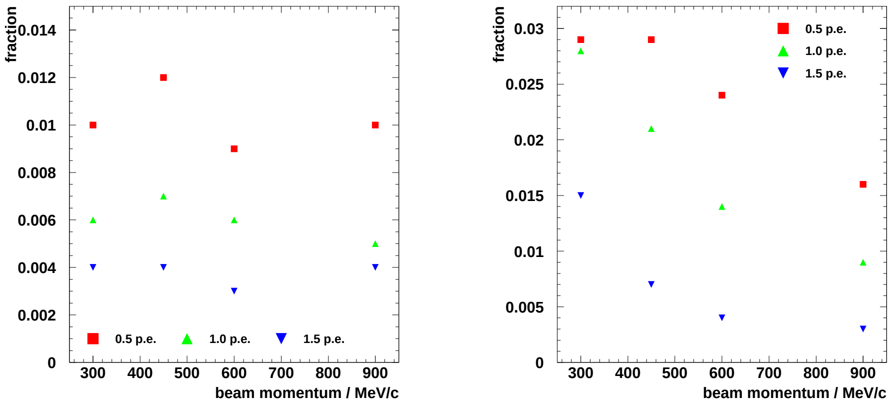

(a) (b)

Figure 4.43: *Fraction of events with large tracklets ($\geq$ 4 fibre channels) for various beam momenta, extracted with different thresholds, PMT 1 only;*
(a) in case of pions and (b) in case of protons.

most restrictive signal threshold, corresponding to 1.5 p.e., is applied in the analysis algorithms.

First of all the distance, given in number of fibres, of the first and second reconstructed tracklet in an SFT module is calculated (see fig. 4.44). Comparing these with distances possible due to the feeding schemes used in the connectors for the light guide [63], one may distinguish optical from electronic crosstalk. In the case of protons, a distinct pattern with several peaks can be observed for MAPMT 1 and MAPMT 2 whereas the remaining two MAPMTs do not exhibit such a pattern, indicating a relationship to the different CDC employed for each MAPMT. Analysing these peaks further it was found, that they are unrelated to the beam profile across a SFT module. Therefore the fibre channels were transformed into readout channels and the tracklet distance was again calculated. A peak at a distance of 16 channels was observed (see fig. 4.45) corresponding to the readout sequence of the GASSIPLEX chip on the PFM [21, 61]. This behaviour of the PFM for large input signals is also described in [66].

The correlation of readout channels clearly demonstrates that there is electronic crosstalk inside the PFM, leading to so-called ”ghost tracklets”. This behaviour has to be understood to enhance the tracking capabilities of the final SFT.

From tab. 4.10 it can be seen that this kind of crosstalk accounts for approximately 50% of all crosstalk events for MAPMT 1 and MAPMT 2. When suppressing the readout sequence crosstalk (RSC), the distinct patterns in the tracklet distance distributions disappear (see fig. 4.46) and the crosstalk levels of all four MAPMTs are comparable. The effect of RSC was observed for signals above 20 p.e., corresponding to a total charge of approx. $2.5 \cdot 10^3$ fC in the case of PMT 1 [41, 67].

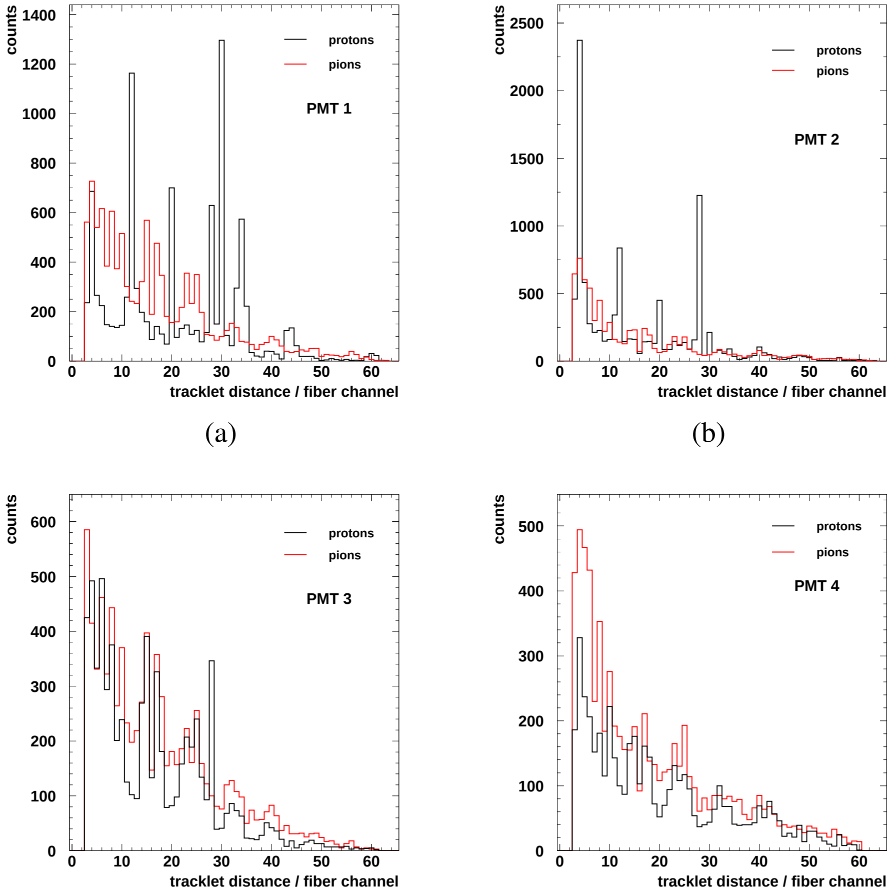

(a) (b)

(c) (d)

Figure 4.44: *Tracklet distance in fibre channel for a beam momentum of* 300 *MeV/c and applying a threshold of* 1.5 *p.e.;*
(a) SFT module 1, (b) SFT module 2, (c) SFT module 3 and (d) SFT module 4.

Table 4.10: *Preprocessing-Frontend Module (PFM) Readout-Sequence Crosstalk (RSC) contribution to total crosstalk for protons at* 300 *MeV/c.*

PMT	events	readout channel distance						RSC total	
		16		32		48		events	frac
1	9986	4315	0.432	34	0.003	542	0.054	4891	0.490
2	10280	4740	0.461	34	0.003	3	0.000	4777	0.465
3	6877	523	0.076	37	0.005	20	0.003	580	0.084
4	4711	26	0.006	73	0.015	11	0.002	110	0.023

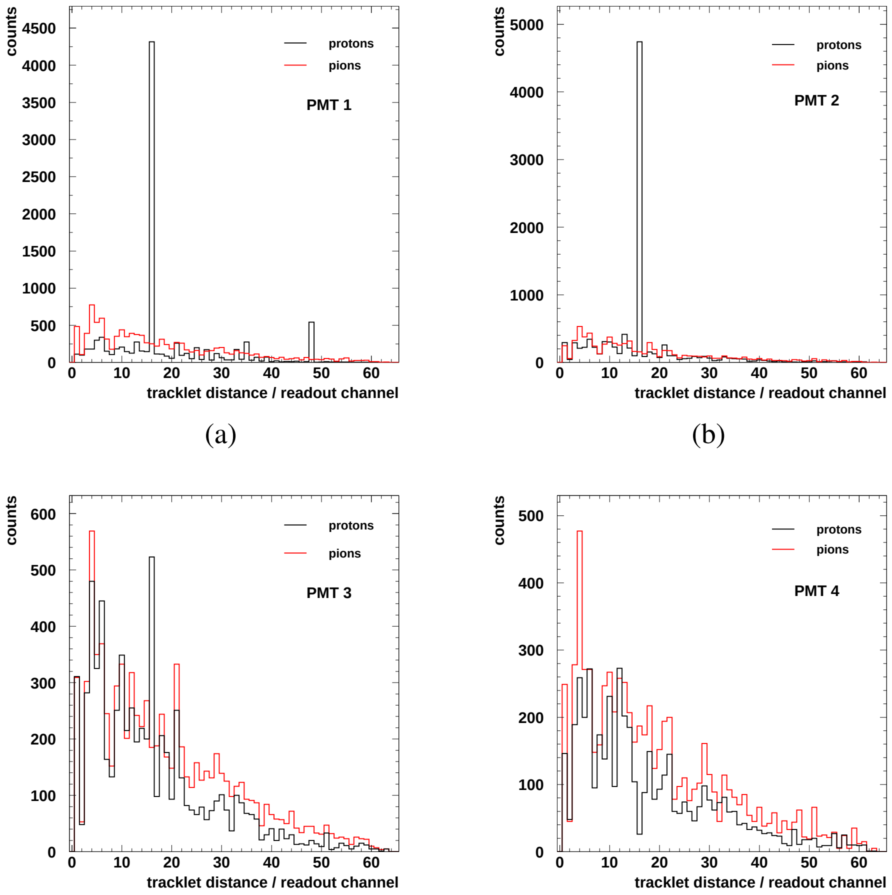

(a) (b)

(c) (d)

Figure 4.45: *Tracklet distance in readout channel for a beam momentum of* 300 *MeV/c, applying a threshold of* 1.5 *p.e.;*
(a) SFT module 1, (b) SFT module 2, (c) SFT module 3 and (d) SFT module 4.

Of further interest is, of course, the signal height contained in the ghost tracklets created by RSC. Therefore all events with ghost tracklets, which contain a readout distance of 16, 32 or 48 channels, are selected. A comparison of the signal height in RSC ghost tracklets to all secondary tracklets is shown in fig. 4.47. From these distributions it can be deduced that only raising the threshold cannot cure this problem, since the signal height of most of the RSC ghost tracklets is well above 2 p.e. and the mean ghost tracklet signal is in the same order as the pion signal.

From the afore mentioned characteristics of RSC, it is obvious, that the RSC depends on the charge fed into the PFM. Therefore the RSC contribution should vanish for higher beam momenta. This behaviour will be demonstrated for the leading RSC contribution, taking into account only crosstalk events with a readout channel distance of 16 channels subsequently called RSC_{16}.

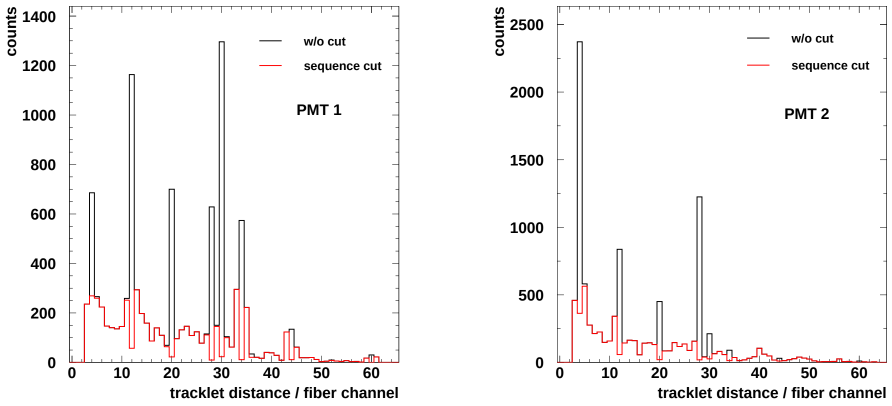

(a) (b)

Figure 4.46: *Comparing tracklet distance distributions with and without Readout-Sequence Crosstalk (RSC) cut for protons at* 300 *MeV/c;*
(a) MAPMT 1 and (b) MAPMT 2.

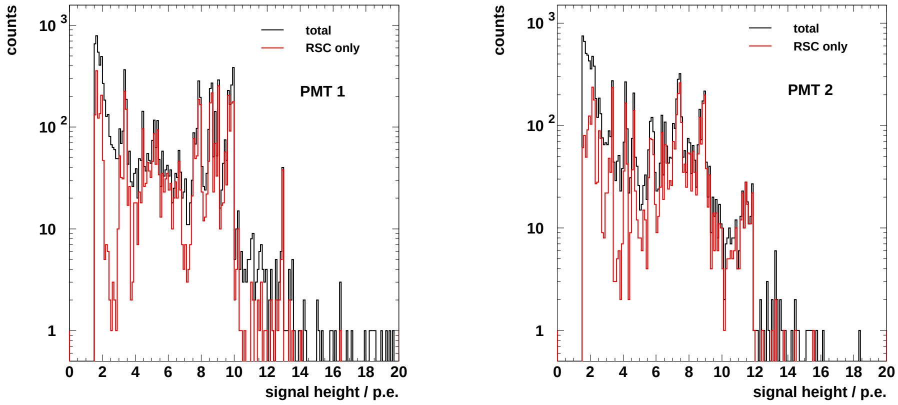

(a) (b)

Figure 4.47: *Energy content of ghost tracklets created by Readout-Sequence Crosstalk (RSC) compared to all secondary tracklets for protons at* 300 *MeV/c;*
(a) for MAPMT 1 and (b) MAPMT 2.

RSC_{16} contributions decrease rapidly for beam momenta above 300 MeV/c (cf. tab. 4.11) and all distinct features in the tracklet distance distributions disappear above 450 MeV/c (see fig. 4.48 a). It is interesting to note that for MAPMT 1 at 450 MeV/c a peak appears at a readout distance of 47 channels, having no correlations in other crosstalk distributions and cannot be attributed to optical crosstalk.

As a cross check, the same distributions for pions at various momenta are compared for MAPMT 1 (see fig. 4.48 b). They exhibit the same behaviour for all momenta as previously expected.

Table 4.11: *Dependence of dominating Readout-Sequence Crosstalk (RSC_{16}) contribution to total crosstalk for protons on beam momentum.*

PMT	P_{beam} [MeV/c]	crosstalk	RSC_{16} contribution events	fraction
1	300	9986	4315	0.432
	450	1902	239	0.126
	600	12908	350	0.027
	900	10746	237	0.022
2	300	10280	4740	0.461
	450	1127	71	0.063
	600	8135	167	0.021
	900	5157	132	0.026

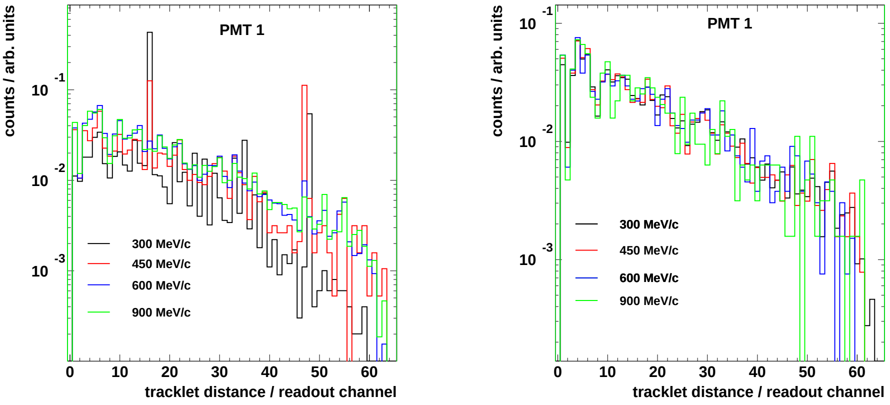

(a) (b)

Figure 4.48: *Momentum dependence of tracklet distance distributions, PMT 1 only; (a) for protons and (b) pions.*

4.2.4 Results from Test Experiment

After the determination of a proper threshold, suppressing noise and optical crosstalk contributions, and identifying electronic crosstalk, important parameters of the SFT prototype modules can be extracted: determination of the energy response and connected with this the detection efficiency; furthermore PID and tracking capabilities. In the following section the extraction of these parameters is described and the results are presented.

Energy Response

For further analysis, a threshold corresponding to 1.0 p.e. is chosen, in agreement with sec. 4.2.3. The energy deposited by particles traversing scintillating fibres, in this case charged pions and protons, depends on their momentum and is described by the Bethe-Bloch formula [28]:

$$-\frac{dE}{dx} = 2\pi\, N_a\, r_e^2\, m_e c^2 \rho \frac{Z}{A}\frac{z^2}{\beta^2}\left[\ln\left(\frac{2\, m_e \gamma^2 \nu^2\, W_{max}}{I^2}\right) - 2\,\beta^2\right] \quad . \tag{4.11}$$

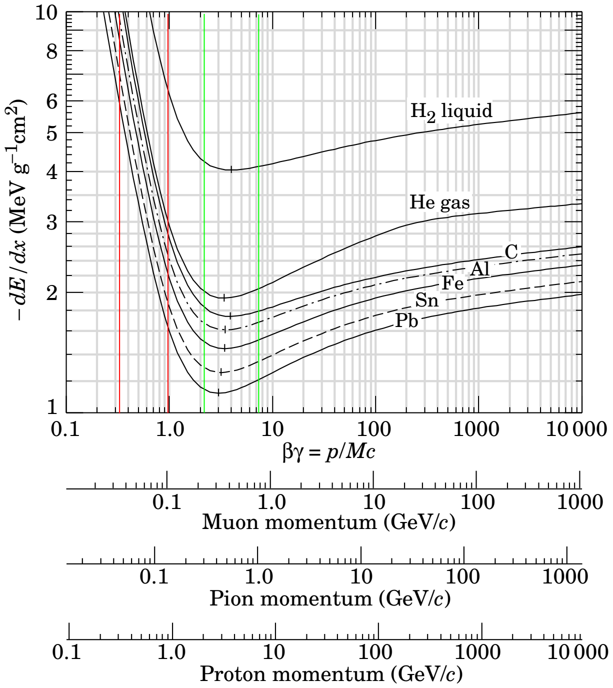

Figure 4.49: *Mean energy loss of charged particles for various materials [29]. Momentum range covered in this test experiment reaches from* 0.3 *GeV/c to* 0.9 *GeV/c. The energy loss in scintillating fibres is comparable to carbon.*

Pions in this momentum range can be regarded as MIPs with a constant energy loss, whereas protons show a steep decrease of deposited energy towards higher momenta, cf. fig. 4.49. This different behaviour can be used in understanding the SFT module response.

As Pions in the selected momentum regime can be regarded as MIP, their mean energy deposition inside the SFT test modules should be more or less independent on the beam momentum and the position of the SFT module in the test experiment setup, i.e. the amount of material traversed before entering the SFT test module. Therefore, the pion response is an ideal tool to study the differences of each SFT module.

The energy response of a SFT test module is shown in fig. 4.50. In this distribution, a tail to higher energies is clearly visible. This behaviour is described by Landau's Theory for thin absorbers [28]. Therefore the Mean Energy Loss (MEL), which is described by the Bethe-Bloch formula, cf. eq. 4.11, corresponds not to the peak position in this distribution but is shifted to higher energies.

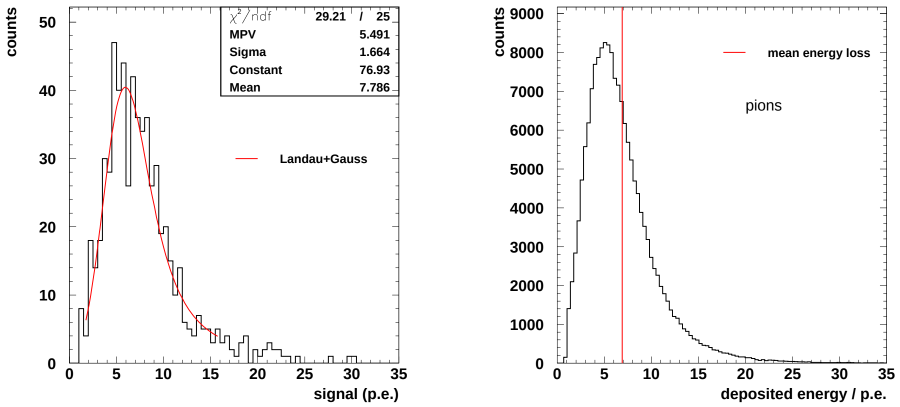

(a) (b)

Figure 4.50: *(a) Energy response of a single fibre of Scintillating Fibre Tracker (SFT) prototype module 1 to pions with a momentum of* $600\,$*MeV/c. The fibre response can be described by a Landau distribution convoluted with a Gaussian distribution.*
(b) Energy response of SFT test module 1 to pions with a momentum of $300\,$*MeV/c. Response is averaged over all 64 channels of a SFT module. The Mean Energy Loss (MEL), marked by the red line, corresponds to* $6.9\,$*p.e., cf. tab. 4.12.*

The MEL for all SFT test modules for all momentum settings is shown in tab. 4.12. In addition, the particle velocity

$$\beta = \frac{p}{E} \quad , \tag{4.12}$$

with p (E) being the particle momentum (energy), is calculated for all 4 momentum settings.

A strong correlation of the extracted MEL to the SFT test module position is observed. This can not be explained by a variation of $\frac{dE}{dx}$ due to energy loss but originates solely in the readout electronics of the SFT modules. This indicates the impact of the employed readout electronics. This issue will be discussed in more detail later in this section. Nevertheless, according to tab. 4.12, the electronics proved to be stable during the complete test experiment within 5%.

In addition to the average SFT module response, the single fibre response was extracted. Since the trigger scintillator acceptance does not coincide with the SFT module width but is smaller, not all channels yield a signal. The normalised fibre response is shown in fig. 4.51 for both the lowest and highest momentum setting. A variation up to a factor of 2 between the fibres of a SFT module is observed, being

Table 4.12: *Particle velocity and Mean Energy Loss (MEL) of all 4 SFT test modules for pions of various momenta. The MEL is averaged over all channels of the corresponding MAPMT.*

P_{beam} MeV/c	Velocity β	Mean energy loss [p.e.] SFT 1	SFT 2	SFT 3	SFT 4
300	0.9062	6.809	6.297	5.338	5.224
450	0.9549	6.991	6.260	5.809	5.644
600	0.9738	6.968	6.356	5.225	5.052
900	0.9881	6.891	6.540	5.492	5.092
Average		6.915 ± 0.082	6.36 ± 0.12	5.47 ± 0.25	5.25 ± 0.27

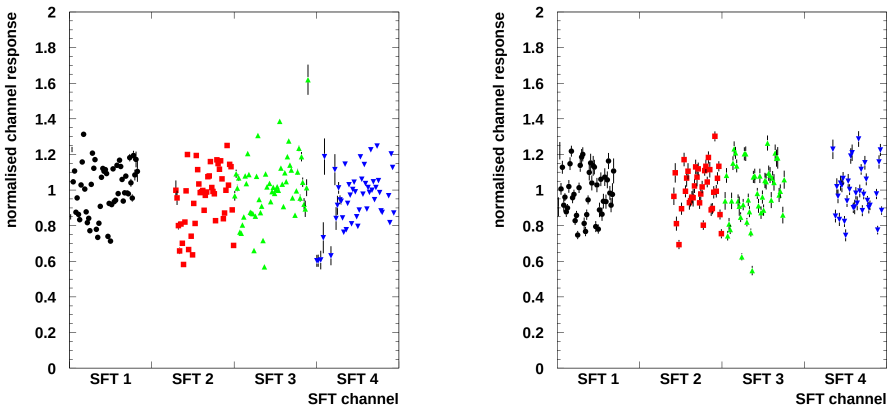

(a) (b)

Figure 4.51: *Channel by channel variation of the energy response of each SFT module for pions. The single channel response is normalised with respect to the corresponding average module response;*
beam momentum of (a) 300 *MeV/c and (b)* 900 *MeV/c.*

much larger than the uncertainties of the MAPMT calibration. The spread of single fibre responses is similar in all 4 SFT modules. No distinctive pattern, which could be attributed to geometrical features of a module, e.g. difference between upper and lower fibre layer, is observed.

Unlike pions, protons in this energy regime cannot be regarded as MIPs. Therefore their MEL depends on the momentum. According to the Bethe-Bloch equation [28] the MEL should fall off $\sim \frac{1}{\beta^2}$. In addition, for slow protons (i.e. below 450 MeV/c) the range is comparable to the penetrated detector length including the trigger scintillators, i.e. a modification of $\frac{dE}{dx}$ towards the end point is expected, leading to a larger energy deposition in the last SFT module compared to the previous ones. This behaviour is known as a Bragg curve. And in fact, a rise of the MEL of protons of a momentum of 300 MeV/c, which corresponds to a range of 1.9 cm in polystyrene (see tab. 4.13), is observed for the last SFT module compared to the other 3 SFT modules in front (cf. tab. 4.14).

Table 4.13: *Kinetic energy and range of protons in plastic scintillator for various momenta. Range inside plastic scintillator material (polystyrene, $\rho = 1.06\frac{g}{cm^3}$) calculated using [65].*

P_{beam} [MeV/c]	E_{kin} [MeV]	Range [cm]
300	46.9	1.9
450	102.5	7.74
600	175.6	19.95
900	362.0	67.42

As for pions, the MEL for each SFT module and each momentum setting is shown in tab. 4.14, as well as the proton velocity according to eq. 4.12. For each SFT module the anticipated decrease of the MEL with increasing particle momentum can be noticed. From fig. 4.52 it can be seen that this drop is corresponding to a $\frac{1}{\beta^2}$-dependence, as expected, for momenta above 300 MeV/c. For protons of a momentum of 300 MeV/c a distinct deviation from a linear behaviour can already be noticed for SFT modules 3 and 4, the most rearward modules in the setup (cf. fig. 4.23).

Table 4.14: *Mean Energy Loss (MEL) of protons for all 4 SFT test modules for various momenta. The MEL is averaged over all channels of the corresponding MAPMT. Errors take only statistical fluctuations into account.*

P_{beam}	Velocity	Mean energy loss [p.e.]			
$[MeV/c]$	β	SFT 1	SFT 2	SFT 3	SFT 4
300	0.3046	50.79 ± 0.06	45.41 ± 0.05	39.38 ± 0.07	43.10 ± 0.09
450	0.4325	26.60 ± 0.08	22.74 ± 0.08	19.31 ± 0.06	17.11 ± 0.06
600	0.5388	17.24 ± 0.02	15.10 ± 0.02	12.26 ± 0.01	11.74 ± 0.01
900	0.6923	11.30 ± 0.02	10.13 ± 0.01	8.50 ± 0.01	7.87 ± 0.01

Obviously the shape of the energy response changes with decreasing momentum from a Gaussian to a Landau distribution with a substantial tail to larger energy depositions (see fig. 4.52).

Apart from the rise due to the Bragg curve behaviour, again a systematic decrease of the MEL with SFT module position is observed. As in the case of pions, this attitude is ascribed to the readout electronics.

For protons a similar spread of single fibre responses is observed as in the case of pions, indicating that this spread is independent of the deposited energy.

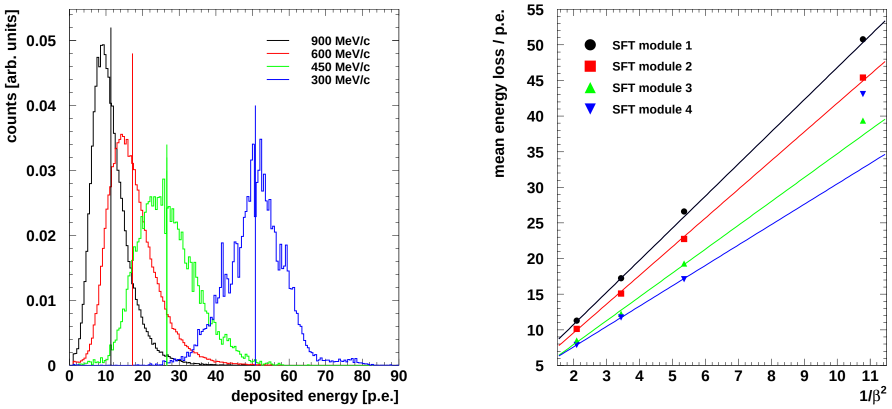

(a) (b)

Figure 4.52: *Energy response of Scintillating Fibre Tracker (SFT) prototype module to protons:*
(a) Energy response of SFT test module 1 to protons for all momentum settings (marked by a different colour). Response is averaged over all 64 channels of this SFT module. The Mean Energy Loss (MEL) is marked by a vertical line in the corresponding colour for each momentum setting, values are given in tab. 4.14;
(b) Mean energy loss of protons as function of $\frac{1}{\beta^2}$. *From the Bethe-Bloch equation [28] a linear correspondence is expected. Deviations from a linear behaviour for SFT modules 3 and 4, respectively, can be explained by a larger* $\frac{dE}{dx}$ *due to the limited range for slow protons, see tab. 4.13.*

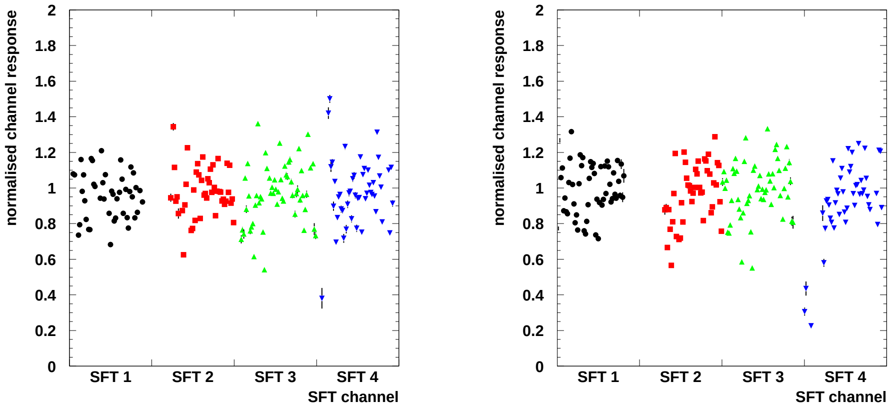

(a) (b)

Figure 4.53: *Channel by channel variation of the energy response of each SFT module for protons. The single channel response is normalised with respect to the corresponding average module response;*
beam momentum of (a) 300 *MeV/c and (b)* 900 *MeV/c.*

Again no distinctive pattern related to geometrical features of a SFT module or the employed feeding scheme can be noticed.

The difference of fibre responses has of course to be taken into account and corrected for in case of PID and space point reconstruction necessary for tracking later on.

Analysis of the energy response of the four SFT test modules revealed an unexpected behaviour, especially for pions, see tab. 4.12 and 4.14. The gradual decrease of the MEL (see fig. 4.54) observed for pions as well as for protons at all momenta suggests a relation with the different employed CDC. The mean gain G_{mean} is comparable for the first three MAPMTs given their HV and CDC combination, which is understandable since the increased voltage nearly cancels the effect of a larger CDC capacitance. But for MAPMT 4, a distinct drop of G_{mean} is observed (cf. tab. 4.7). It is already known that the PFM response is not linear for small signals [66]. This might explain the signal decrease in case of MAPMT 4 (see fig. 4.54). However, the signal height obviously depends on the SFT module, so that there must be some other mechanism attenuating the signal of MAPMT 2 and 3. The MAPMT calibration uncertainty is unlikely to cause this decrease, since all 64 channels of a certain MAPMT need to be systematically miscalibrated to explain this behaviour. There are several other options to explain the signal decrease.

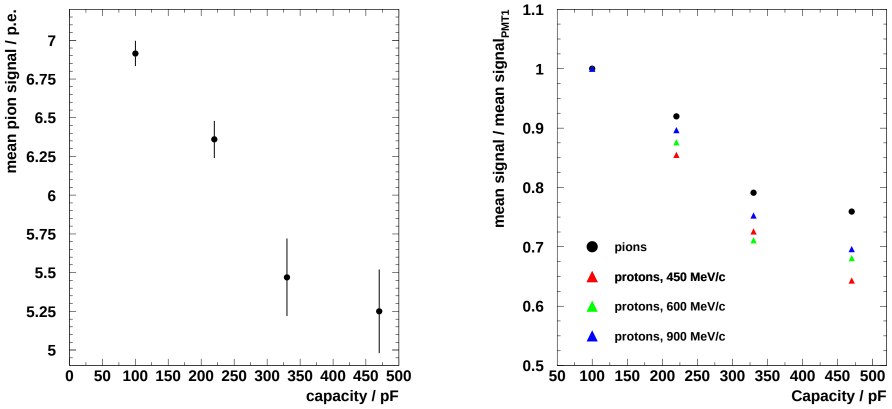

(a) (b)

Figure 4.54: *Influence of Charge Divider Circuit (CDC) on Minimum Ionising Particle (MIP) signal:*

(a) Dependance of mean pion signal on capacity used in CDC on the Photo-Multiplier Board (PMB);

(b) Relative signal decrease with capacity used in CDC on the PMB.

First of all the SFT modules itself or the LG are possibly not uniform in their characteristics, i.e. light yield, transmission losses at the connectors or absorption length. But it seems rather unlikely that the SFT modules and LG were setup by coincidence such that one yields a systematic drop. Moreover, SFT module 1 and 3 are of the same production batch as well as SFT module 2 and 4. The LG attached to SFT modules 1, 2 and 4 were produced in Giessen whereas the LG of SFT module 3 was built by INFN Bari [67].

Secondly, the readout electronics and their power supply might be the reason. The non-uniformity of the PFM was found to be unlikely to be the reason. Another cause might be the LV. It is known from laboratory tests [58] that drifts in the LV lead to pedestal variations. During this test experiment such LV drifts were observed [67], but commonly for all SFT modules. Nevertheless there is a systematic order in the LV distribution, namely the LV is first fed into MAPMT 1 and then subsequently to the remaining MAPMTs, which in turn might lead to a systematic drop of the voltage levels on the PFM [61]. Since the LV was not monitored regularly and for each PFM separately, no evidence for this assumption can be given.

Last not least the trigger timing on the PFM might not be stable. This then might lead to a signal reduction, as the signal height depends strongly on the trigger timing [66].

Comparison with Simulation

To compare the experimental results, a GEANT [68] simulation with a simplified geometry was used. Only three scintillating fibres were simulated without any additional detectors present in the GSI test experiment set-up. The intrinsic fibre setup was accurately simulated, i.e. the fibre core is surrounded by cladding and different material mixtures for core and cladding were used. The geometry is shown in fig. 4.55, the beam enters the fibres perpendicular to their axis from above.

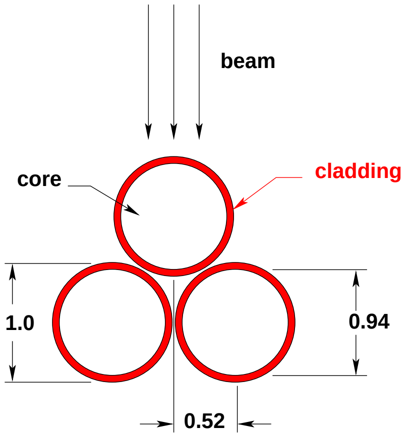

Figure 4.55: Simplified GEANT geometry for the GSI test experiment simulation.

Since no details about the beam quality during the GSI test experiment are known, monoenergetic pions and protons of the same central momentum settings used at GSI are generated. Their impact parameter is varied over one fibre diameter to get the same results as the Tracklet Algorithm (TA) reconstructs from test experiment data to check the space point-reconstruction capabilities of the SFT test modules. The deposited energy is stored for each of the three fibres individually to compare these values to the experimental results and validate the performance of the Sophisticated Cluster Algorithm (SCA). The simulation does not include any assumptions on the light transport nor optical crosstalk and electronic noise, thus yielding the *perfect* detector response. This *perfect* detector response is correlated to the central values of the experimentally determined response functions, but does not allow to estimate crosstalk levels.

To be able to compare the energy response obtained by the simulation to test beam data, one needs to emulate some routines of the GSI analysis software.

For the single fibre response this means to take into account only the fibre with the largest energy deposition in a SFT module, which will be referred to from now on as "the leading fibre". The mean energy loss extracted from simulations for pions and protons is given in tab. 4.15. As expected, for pions this value is constant, whereas for protons a large variation is seen. For further comparisons between simulation and test experiment data, an averaged value for pions will be used.

Table 4.15: *Mean Energy Loss (MEL) in leading fibre, extracted using a GEANT simulation, for pions and protons of various momenta. Average MEL for pions:* $\Delta E_{pion} = (0.193 \pm 0.011) MeV$.

P$_{beam}$ $[MeV/c]$	Mean energy loss [MeV] pions	 protons
300	0.202 ± 0.002	1.217 ± 0.001
450	0.194 ± 0.002	0.670 ± 0.001
600	0.199 ± 0.003	0.457 ± 0.001
900	0.177 ± 0.005	0.303 ± 0.001

The energy response of leading fibres is shown for experimental data (see fig. 4.56 a) and simulation (see fig. 4.56 b). The shape is in reasonable agreement, taking into account a broadening of the experimental results due to the limited photon statistics and the finite resolution of the readout electronics. In addition, the transition from Landau to Gaussian shaped response functions for slow protons is also present in the simulation results. Moreover the extracted MEL from test experiment data are compared to simulation results, shown in fig. 4.57. For SFT modules 1 and 2 a linear dependence is observed. For the last two modules deviations from linear behaviour are seen for slow protons only, which again can be explained by variations of $\frac{dE}{dx}$ due to energy loss in the trigger scintillators, which are not reproduced by the simulation due to the simplified geometry as explained previously. Therefore only the data for pions and protons above momenta of 450 MeV/c are taken into account for a linear fit of these two SFT modules. This correlation then yields the energy deposition per p.e. (see tab. 4.16). The correlation was alternatively extracted without using pion data, but no discrepancy was found. This linear correlation then suggests, that simulation and test experiment data are in fair agreement.

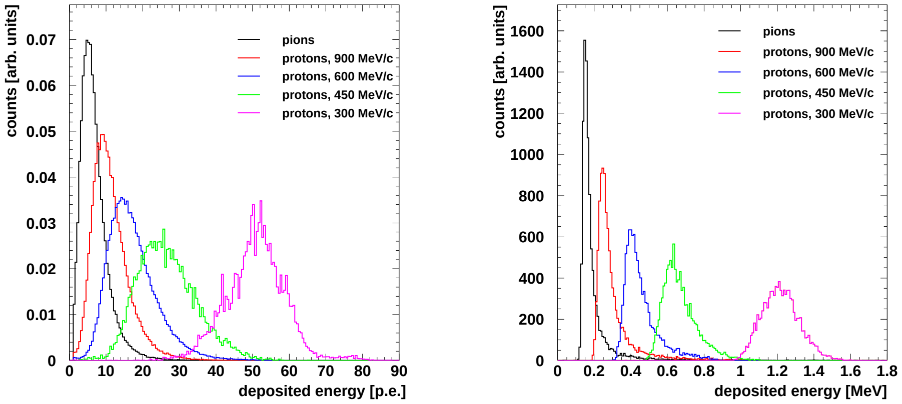

(a) (b)

Figure 4.56: *Comparison of response functions obtained from GSI test experiment and GEANT simulation:*

(a) Energy response of leading fibres for pions and protons of various momenta, extracted from GSI test experiment data. The energy response is averaged over all fibres of Scintillating Fibre Tracker (SFT) prototype module 1;

(b) Energy response of leading fibres for pions and protons of various momenta, extracted from a GEANT simulation emulating the GSI software routines.

Table 4.16: *Correlation between experimental data and GEANT simulation. Note, that for Scintillating Fibre Tracker (SFT) modules 3 and 4 only protons above* 300 *MeV/c and pions are taken into account.*

SFT module	slope $\left[\frac{MeV}{p.e.}\right]$
1	$0.023 \pm 3.2 \cdot 10^{-5}$
2	$0.026 \pm 3.7 \cdot 10^{-5}$
3	$0.033 \pm 1.3 \cdot 10^{-4}$
4	$0.040 \pm 1.5 \cdot 10^{-4}$

Extracting Efficiencies

The scintillator S3 was installed immediately behind the SFT modules for extracting detection efficiencies. Compared to the trigger scintillators S1 and S2, the

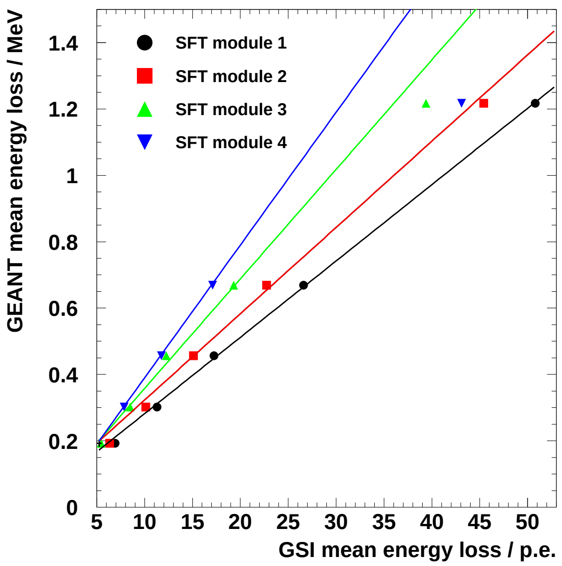

Figure 4.57: *Comparison of the Mean Energy Loss (MEL) extracted from experimental data and the GEANT simulation. For SFT modules 3 and 4 the first 4 data points only are taken into account for fitting due to the non-linear energy deposition of slow protons.*

dimensions of S3 are smaller than a SFT module. Requiring a signal in S3 therefore ensures that a particle passed through the SFT modules. The signal spectrum of S3 for 600 MeV/c particles is shown in fig. 4.58 as well as the imposed threshold for this analysis.

Imposing the condition of a signal in S3 as well as a signal in a single SFT module, one obtains a beam profile, as shown in fig. 4.59, for each SFT module. For SFT modules 2 and 3, dead channels are observed in the centre of the acceptance which, of course, reduces the efficiency. Dead channels are observed for SFT module 4 as well, but only towards the edge which influences the efficiency only slightly. The beam profiles exhibit a similar shape for all momenta, therefore no additional cut on SFT module fibre position was introduced. For protons at 300 MeV/c no beam profile could be obtained with this method, since all protons were stopped inside S3 and thus no trigger was formed.

To extract efficiencies for individual SFT modules hits in the remaining SFT modules are required in addition to the above mentioned conditions to ensure that a particle traversed all SFT modules and to reduce background from multiple scattering. The efficiency ϵ_{SFT} of a single SFT module is then determined as the ratio of events with hits in this particular module and the reference system $N_{ref \wedge SFT}$ compared to all events with hits in the reference system N_{ref}:

$$\epsilon_{SFT} = \frac{N_{ref \wedge SFT}}{N_{ref}} \quad . \tag{4.13}$$

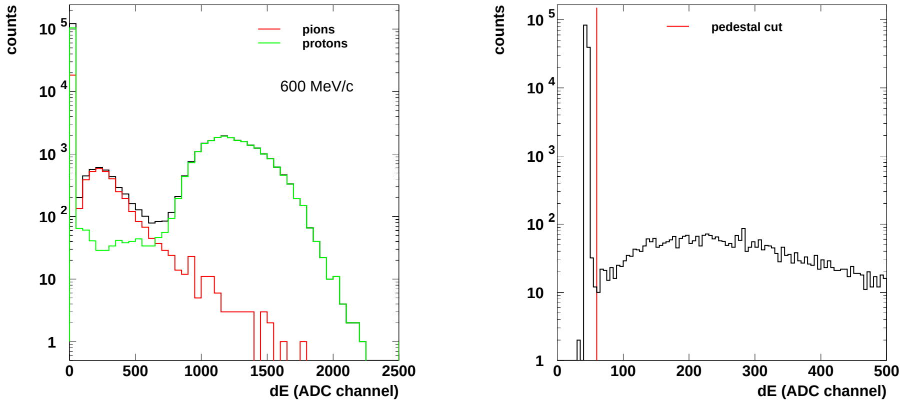

(a) (b)

Figure 4.58: *Response of scintillator S3 which is used for efficiency studies of the prototype modules:*
(a) Energy deposition in scintillator S3 for both particle types at 600 *MeV/c. Information of this scintillator was not used for Particle IDentification (PID);*
(b) pedestal cut applied to S3.

For calculating the error one has to keep in mind that these two quantities are completely correlated, which implies the use of the following equation [69]:

$$\Delta\epsilon_{SFT} = \epsilon_{SFT} \cdot \sqrt{\frac{\sigma^2_{ref\wedge SFT}}{N^2_{ref\wedge SFT}} + \frac{\sigma^2_{ref}}{N^2_{ref}} - \frac{2 \cdot \sigma^2_{ref\wedge SFT}}{N_{ref\wedge SFT}\, N_{ref}}} \tag{4.14}$$

Since the detection efficiency depends on the deposited energy ΔE, any imposed threshold affects the value of ϵ_{SFT}. Therefore three different thresholds — 0.5 p.e., 1.0 p.e. and 1.5p.e. — were applied to study the impact on the efficiency. Furthermore ΔE depends on the particle type and, in case of protons, on the momentum as well.

ϵ_{SFT} is hence extracted according to PID, momentum and threshold. All results can be found in appendix B.1. In the following, only results for SFT modules 1 and 2 are presented as examples. SFT module 1 represents a perfect module whereas SFT module 2 has one dead channel (cf. fig. 4.59) which enables a study of the impact of such defects.

Pions in the momentum regime of this test experiment can be regarded as MIPs, thus marking the lower limit of ΔE to detect with the SFT. Therefore, the detection efficiency for pions ϵ^{pion}_{SFT} is expected to be constant with respect to the beam momentum. For SFT module 1 a small variation with beam momentum is observed but, within error bars, ϵ^{pion}_{SFT} can be regarded as constant. The efficiency is clearly affected by the threshold and drops substantially with larger thresholds, but for the anticipated threshold of 1.0 p.e. ϵ^{pion}_{SFT} is still above 99%. For SFT module 2 the efficiency in general is smaller due to a dead channel. This effect is enhanced at

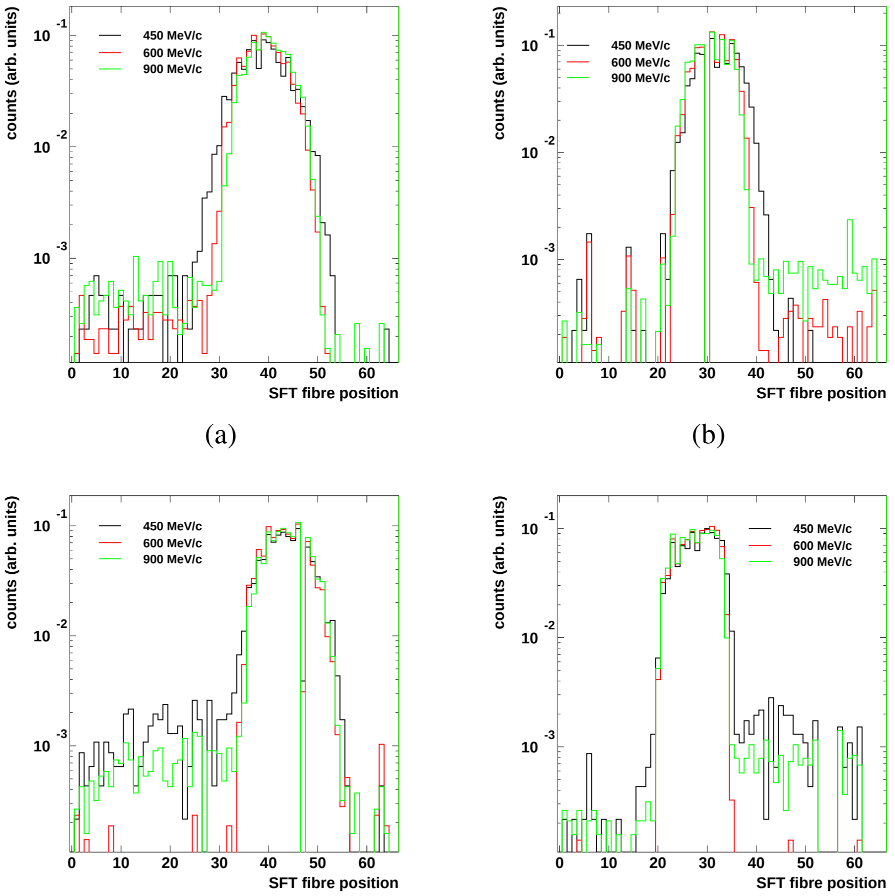

(a) (b)

(c) (d)

Figure 4.59: *Beam profile for protons of various momenta after applying all necessary cuts for Scintillating Fibre Tracker (SFT) 1 (a), SFT 2 (b), SFT 3 (c) and SFT 4 (c). Dead channels are found for SFT 2 and 3. Tails on either side of the central peak are due to multiple scattering and crosstalk.*

larger thresholds, since the effective gap width increases because the path length in one of the adjacent fibres has to be long enough to create a signal above threshold. For a threshold of 1.0 p.e., ϵ_{SFT}^{pion} is in the order of 97%, i.e. 2% less than for a perfect module. The sudden drop of ϵ_{SFT}^{pion} at 900 MeV/c is likely due to problems in the LV but is not completely understood.

For protons, ΔE drops with momentum, but since protons are not MIPs, the detection efficiency ϵ_{SFT}^{proton} is expected to be superior to pions over the entire accessible momentum range. SFT module 1, as example for a perfect SFT module, exhibits a constant detection efficiency well above 99% which is only slightly affected by large thresholds. As already observed for pions, ϵ_{SFT}^{proton} for SFT module 2 is reduced due to a dead channel and exhibits a correlation with beam momen-

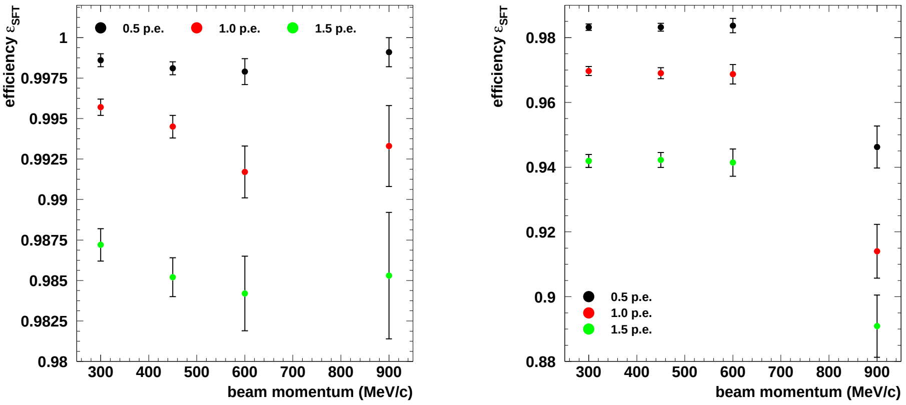

(a) (b)

Figure 4.60: *Detection efficiency ϵ_{SFT} for pions extracted for different thresholds; (a) for SFT module 1 and (b) SFT module 2.*

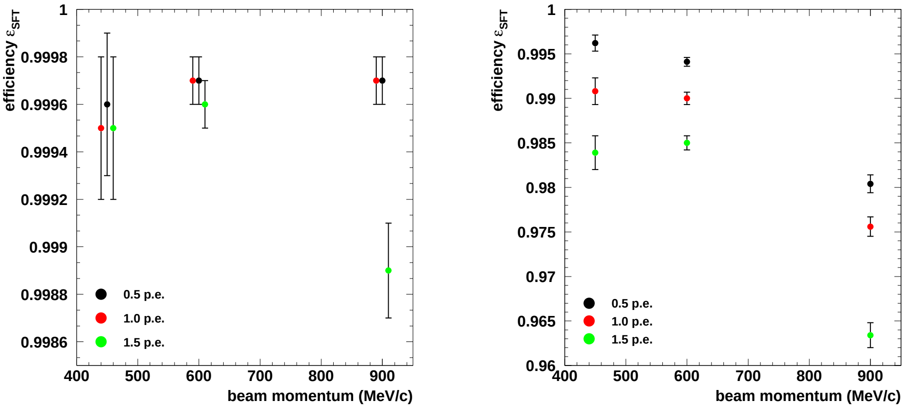

(a) (b)

Figure 4.61: *Detection efficiency ϵ_{SFT} for protons extracted for different thresholds; (a) for SFT module 1 and (b) SFT module 2.*
For better visibility, the data points of SFT module 1 were shifted by 20 MeV/c.

tum. The impact of larger thresholds is increased, leading to a significant reduction of detection efficiency. For the anticipated threshold of 1.0 p.e. this leads to a reduction of about 1%, yielding a detection efficiency ϵ_{SFT}^{proton} of app. 99%. Again a large drop is observed for the highest beam momentum as in the case of pions.

Particle Identification capabilities

The different energy loss ΔE of protons and pions (cf. fig. 4.56 a) will be exploited for PID. In a first step the response function for both particle types and each momentum setting is used to estimate the contamination of a proton sample with pions when using a cut on ΔE only. The threshold is determined by rejecting the low ΔE tail of the proton response function according to the selected proton efficiency. The pion contamination is given by the fraction of pions above this threshold compared to the fraction of both pions and protons above this threshold [60]. The respective ΔE distributions of pions and protons are normalised for this procedure. For this study the proton efficiency was varied between 85% and 98% and the corresponding pion contamination is shown in fig. 4.62. Above a momentum of 600 MeV/c the pion contamination is increasing sharply, complicating a particle distinction noticeably.

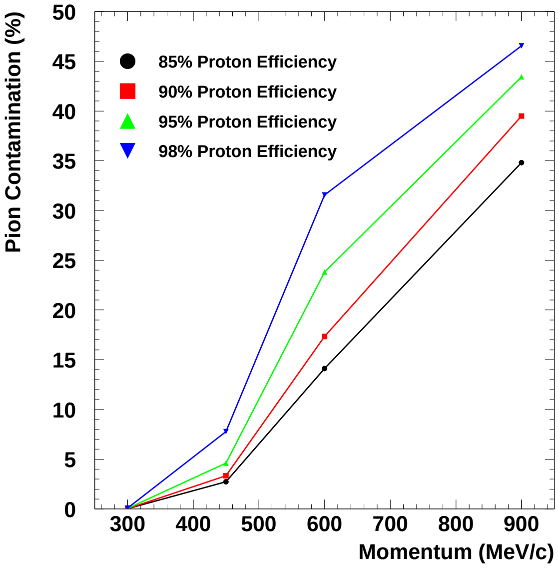

Figure 4.62: *Particle IDentfication (PID) capability of Scintillating Fibre Tracker (SFT) prototype modules. Pion contaminations are derived from energy response functions at different momenta for various proton efficiencies. Lines are drawn to guide the eye.*

In a more detailed study [62] employing a conditional probability scheme like for HERMES PID detectors, these findings were confirmed, determining the pion rejection factor below 600 MeV/c to better than 10. According to the expected momentum distribution for pions, this will be sufficient to achieve the envisaged background suppression.

Tracking capabilities

Another important characteristic to be studied is the spatial resolution of the SFT prototype modules. As there were no independent tracking devices for precise track reconstruction available only preliminary studies could be performed. The two parallel oriented modules are used and correlation of leading tracklet in each module were analysed. For estimating the spatial resolution, a nominal spacing of 0.52 mm for adjacent fibres and a perfect parallel orientation of both modules was assumed. The obtained correlation integrated over all fibre channels is approximated by a Gaussian distribution with a width of $300\,\mu m$, see fig. 4.63. Taking into account that two SFT modules are used in this study, the single module resolution is determined to be $200\,\mu m$ being slightly larger than anticipated but, given the non-ideal conditions, indicating a sufficient resolution to meet the specifications.

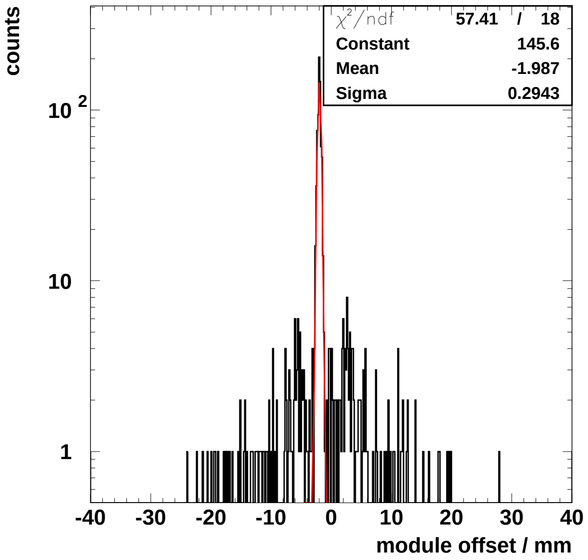

Figure 4.63: *Preliminary result of spatial resolution for two identical prototype modules with 600MeV/c pions impinging. The obtained peak in the spatial correlation of the two modules is described by a Gaussian, yielding a resolution of approximately 300* μm*. The tails on either side of the peak are due to multiple scattering or wrongly reconstructed hits due to crosstalk.*

In terms of Space Point Reconstruction and tracking, not only the detection efficiency is of importance but the reliability of the reconstructed space point as well. Any threshold has to be chosen such, that ϵ_{SFT} is still acceptable but crosstalk effects, which lead to wrongly reconstructed space points, are minimised. Crosstalk sources and thresholds were studied in detail in sec. 4.2.3 and taking these results into account, a threshold equivalent to 1.0 p.e. is chosen. Of course, RSC contributions, see sec. 4.2.3, have to be taken into account as well.

The reconstruction quality is investigated by requiring only one reconstructed hit per module in all but one SFT module and then observe the number of reconstructed hits in this SFT module. Since this condition leads to low statistics, information of scintillator S3 was omitted. Any wrongly reconstructed hit will further on be regarded as contamination. SFT module 1 will serve as an example throughout this section, i.e. SFT modules 2, 3 and 4 act as a reference system in which only one hit per module is permitted. Numbers for all modules can be found in appendix B.2. For SFT modules 1 and 2, RSC suppression is used to obtain the results.

First of all, the size of the reconstructed tracklets in the reference system is investigated. In an ideal case, these tracklets consist of 1 or 2 fibres, but the size can be enhanced by optical crosstalk. For the limiting cases of 300 MeV/c and 900 MeV/c beam momentum respectively, the tracklet size in the reference modules is shown in fig. 4.64. All reference modules exhibit the same behaviour and the tracklet size does not substantially exceed a size of 5 fibres. This in turn means, that the capability of detecting two separate tracklets in the reference system is not spoiled by noise contributions or that a large contribution of merged tracklets is observed respectively.

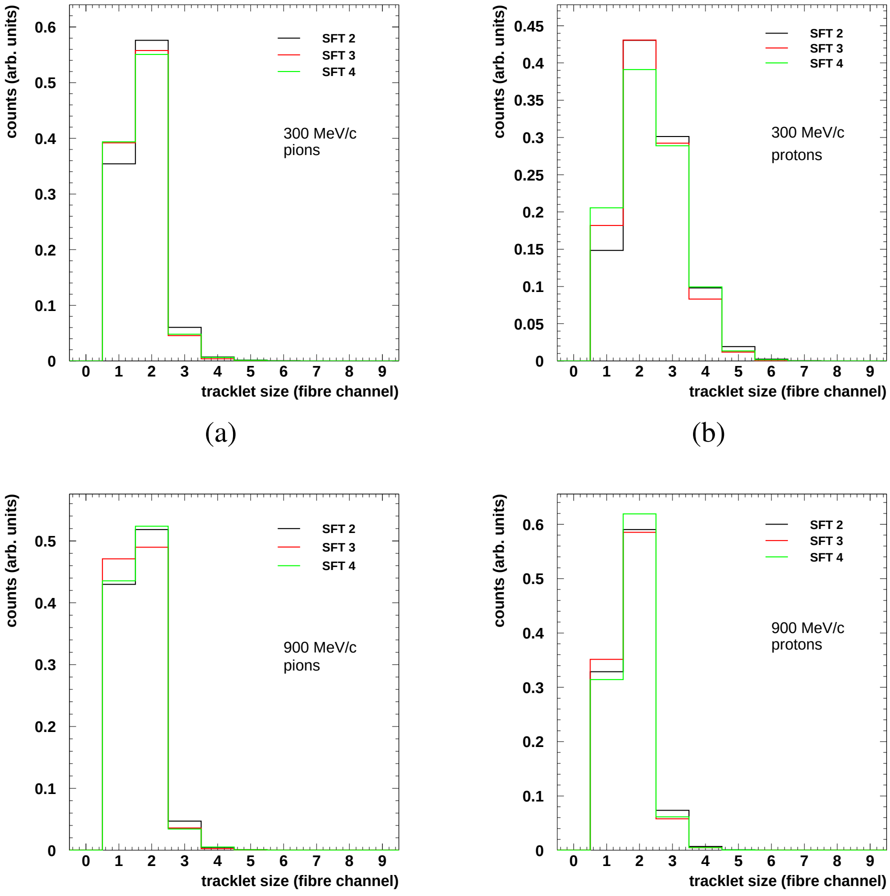

(a) (b)

(c) (d)

Figure 4.64: *Size of reconstructed tracklets in the reference SFT modules:*
(a) for pions and (b) protons of 300MeV/c beam momentum;
(c) for pions and (d) protons of 900MeV/c beam momentum.

The results of the contamination study are shown in fig. 4.65, events with no reconstructed tracklet are rejected. The fraction of events with more than one reconstructed tracklet depends on particle type and beam momentum. For pions at all momenta, a similar behaviour is observed, leading to a contamination of about 10%, events with more than two tracklets are negligible. For protons a strong correlation with beam momentum is observed. The level of contamination ranges from around 15% at high momenta to about 50% at low momenta. A substantial contribution of events with more than 2 tracklets is seen for momenta below 600 MeV/c. At higher beam momenta the results for protons conform to those for pions. It is obvious, that this behaviour is correlated with the signal height, but whether the contamination arises due to optical or electronic crosstalk can not be decided reliably. In any case, not more than 6 reconstructed tracklets were observed.

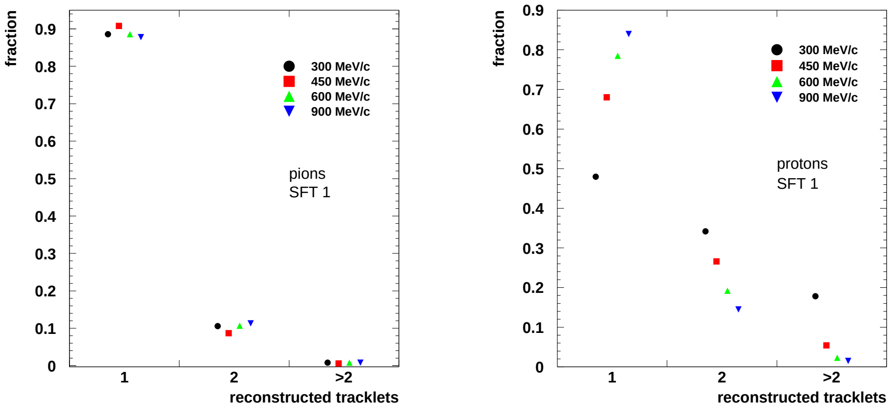

(a) (b)

Figure 4.65: *Number of reconstructed tracklets in SFT module 1, Threshold corresponds to* 1.0 *p.e;*
(a) for pions and (b) protons.

Chapter 5

Hard Exclusive Reactions and Generalised Parton Distributions

A few years ago, the new theoretical framework of Generalised Parton Distributions (GPD) was developed for the description of hard exclusive processes [70, 71]. The GPD formalism implicitly includes parton distribution functions (PDF) and form factors (FF), but also embodies additional non-perturbative aspects of the QCD structure of the nucleon. As an example, the total angular momentum of quarks inside the nucleon

$$J^q = \frac{1}{2}\Delta\Sigma + L^q, \tag{5.1}$$

where $\Delta\Sigma/2$ is the quark spin and L^q the orbital angular momentum contribution, can in principle be accessed through a sum rule from second moments of two GPDs [71]. Two types of hard exclusive reactions are of particular interest in the study of GPDs:

$$\gamma^*(q) + T(p) \rightarrow \gamma(q') + T'(p'), \quad \gamma^*(q) + T(p) \rightarrow M(q') + T'(p'), \tag{5.2}$$

in which a virtual photon γ^* with high energy and large virtuality $-q^2 = Q^2 > 0$ interacts with a hadronic target *T* and produces a real photon γ, see fig. 5.1, or a meson *M*, and a low-mass hadronic state *T'*. The amplitudes of the processes given in eq. 5.2 can be factorised into a hard scattering coefficient which describes the short distance perturbative stage of the interaction and can be calculated in Next-to Leading Order (NLO) QCD, a GPD which contains non-perturbative nucleon structure information and, in case of exclusive meson production, a meson distribution amplitude which describes how the meson is formed from the two partons. In case of the production of a real photon, no additional distribution amplitudes enter the description thus simplifying the theoretical description considerably. Due to the factorisation theorem, which establishes a clear separation of the interaction into a perturbative and a non-perturbative part, the same universal distributions enter the description of various hard reactions. They provide a unified formalism for the description of inclusive deep-inelastic scattering, exclusive meson production, Deeply-Virtual Compton Scattering (DVCS) and electromagnetic form factors. It has to be noted that the factorisation theorems for exclusive reactions holds only for longitudinally polarised virtual photons [72].

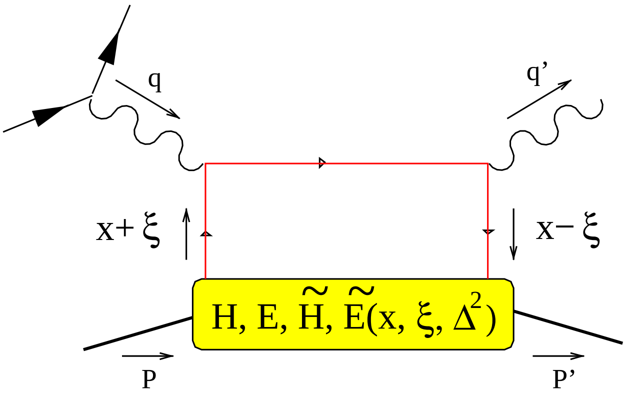

Figure 5.1: *Handbag diagram of the Deeply-Virtual Compton Scattering (DVCS) process. The nucleon stays intact throughout the process. The non-perturbative structure of the nucleon is described by the Generalised Parton Distributions (GPD) H^q, E^q, $\tilde{H}^q$ and $\tilde{E}^q$.*

5.1 Properties of Generalised Parton Distributions

There are four leading twist[1] GPDs for each quark flavour q in the nucleon: the unpolarised distributions H^q and E^q and the polarised distributions $\tilde{H}^q$ and $\tilde{E}^q$. The GPDs H^q and $\tilde{H}^q$ conserve nucleon helicity, while E^q and $\tilde{E}^q$ are associated with a helicity-flip of the nucleon. The polarised GPDs $\tilde{H}^q$ and $\tilde{E}^q$ also involve a spin-flip of the probed quark. These GPDs depend on the longitudinal momentum fractions x and ξ where the initial and final proton move fast, and on the Mandelstam variable

$$t = \left(p - p'\right)^2 = \Delta^2, \tag{5.3}$$

where Δ is the overall momentum transfer. The variable ξ, also called skewedness parameter, is related to x_B, the momentum fraction of the nucleon carried by the struck quark, as

$$\xi \approx \frac{x_B}{2 - x_B} \tag{5.4}$$

in the kinematic limit of large photon virtuality and energy with x_B being fixed. The GPDs describe quark-quark correlations where a quark with momentum fraction $x + \xi$ is removed from the initial nucleon and is put back into the final nucleon with a longitudinal momentum fraction $x - \xi$. The initial and final nucleon states

---

[1] An exact definition of twist can be found in [72]. For practical use it is sufficient to say that effects of twist h never enter hard processes with suppression less than $(M/Q)^{h-2}$, with M being the hadronic mass.

have different momenta *p* and *p'* due to the momentum transfer t. In the forward limit $t \rightarrow 0, \xi \rightarrow 0$

$$\begin{array}{lll} H^q(x,0,0)=q(x), & \tilde{H}^q(x,0,0)=\Delta q(x) & \text{for } x>0, \\ H^q(x,0,0)=-\overline{q}(-x), & \tilde{H}^q(x,0,0)=\Delta\overline{q}(-x) & \text{for } x<0 \end{array} \qquad (5.5)$$

the ordinary quark and quark helicity distributions are obtained. With x defined in the range [-1,+1], the longitudinal momentum fractions $x+\xi$ and $x-\xi$ can be either positive or negative corresponding to quark or anti-quark distributions, respectively. The GPDs E^q and $\tilde{E}^q$ are not accessible in the forward limit [73] but nevertheless carry information on the nucleon structure in the forward limit. The first moments of the GPDs are related for any ξ to the elastic nucleon form factors through model independent sum rules [71, 74]:

$$\begin{array}{ll} \sum_q e_q \int\limits_{-1}^{1} \mathrm{d}x H^q(x,\xi,t)=F_1(t), & \sum_q e_q \int\limits_{-1}^{1} \mathrm{d}x E^q(x,\xi,t)=F_2(t), \\ \sum_q e_q \int\limits_{-1}^{1} \mathrm{d}x \tilde{H}^q(x,\xi,t)=g_A(t), & \sum_q e_q \int\limits_{-1}^{1} \mathrm{d}x \tilde{E}^q(x,\xi,t)=h_A(t), \end{array} \qquad (5.6)$$

where $F_1(t)$ and $F_2(t)$ are the elastic Dirac and Pauli nucleon form factors, and $g_A(t)$ and $h_A(t)$ are the axial-vector and pseudo-scalar form factors.

While form factors and PDFs can be measured in non-exclusive reactions, the total angular momentum J^q carried by quarks inside the nucleon remained unaccessible until recently. Ji's relation [71] connects the second moment of the sum of the unpolarised GPDs in the forward limit to the total angular momentum $J^{q'}$ for a given quark flavour q':

$$J^{q'} = \lim_{t\rightarrow 0} \frac{1}{2} \int\limits_{-1}^{1} \mathrm{d}x x \left[H^{q'}(x,\xi,t) + E^{q'}(x,\xi,t) \right]. \qquad (5.7)$$

A determination of the contributions $J^{q'}$ from all quark flavours q' yields the total angular momentum J^q. In principle, the orbital angular momentum L^q of the partons inside the nucleon can be derived using eq. 5.1 and the information on $\Delta\Sigma$ available from polarised inclusive and semi-inclusive Deep-Inelastic Scattering (DIS). At present, no other way is known to determine L^q.

5.2 Deeply Virtual Compton Scattering

The cleanest exclusive process to study GPDs is DVCS [71], in which a photon γ^* with high virtuality (Q^2) interacts with a quark inside the hadronic target and produces a real photon γ. The hadronic target is left intact. The DVCS process combines the advantages of DIS and Compton scattering. The initial photon is off-shell, thus opening an additional dimensional parameter with respect to real Compton scattering, because the virtuality can be 'tuned' in the given kinematic limits. This reaction is unique, as it carries direct information about the partonic structure of the nucleon.

5.2.1 Kinematics and Asymmetries

In this subsection the extraction of informations on GPDs from DVCS measurements is explained and the necessary observables are introduced assuming an unpolarised proton target. Further details on changes due to nuclear targets will be given in the next subsection.

The electroproduction of real photons

$$e(k) + N(p) \rightarrow e(k') + N(p') + \gamma(q') \tag{5.8}$$

is described in terms of the four-momenta of the incoming and outgoing electron (k, k') and nucleon (p, p'). The four-momentum transfer by the virtual photon is defined by

$$\begin{aligned} q^2 \equiv -Q^2 &= (k-k')^2 \\ &\overset{lab}{=} 4EE'\sin^2\tfrac{\theta}{2}. \end{aligned} \tag{5.9}$$

In the laboratory frame (lab) E and E' denote the initial and final electron energy and θ is the scattering angle of the electron. In a fixed target experiment like HERMESwith the target nucleon at rest, the variable ν, given by

$$\nu = \frac{pq}{M} \overset{lab}{=} E - E', \tag{5.10}$$

turns out to be the energy loss of the scattered electron. The squared invariant mass of the photon-nucleon system is given by

$$W^2 = (p+q)^2 \overset{lab}{=} M^2 + 2M\nu - Q^2, \tag{5.11}$$

with M being the nucleon rest mass. Another important variable used to describe DIS events is the Bjorken variable

$$x_B \equiv \frac{Q^2}{2pq} = \frac{Q^2}{2M\nu}, \tag{5.12}$$

being interpreted as the four-momentum of the nucleon carried by the struck quark. All variables described above (q^2, ν, W^2, x_B) are inclusive, i.e. are fully described by the outgoing lepton kinematics. In order to describe exclusive processes like DVCS, the momentum transfer to the nucleon, given by the Mandelstam invariant

$$t = (p-p')^2 = (q-q')^2, \tag{5.13}$$

which can be calculated either from the initial and final proton or photon four-momenta, has to be included.

The DVCS final state is indistinguishable from that of the Bethe-Heitler (BH) process, see fig. 5.2, where the photon is radiated by the incoming or outgoing lepton. This leads to an interference of the processes on the amplitude level.

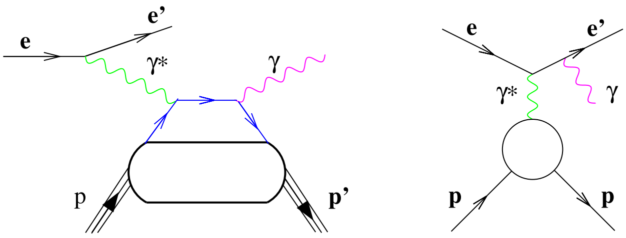

Figure 5.2: *Feynman graphs of Deeply-Virtual Compton Scattering (DVCS) (left panel) and Bethe-Heitler (BH) process (right panel). Both processes lead to the same final state, thus their amplitudes interfere.*

The differential cross section for the *ep* scattering process with unpolarised protons and leptons is given by [77]

$$\frac{d\sigma}{d\phi dt dQ^2 dx_B} = \frac{1}{32\,(2\pi)^4}\frac{x_B y^4}{Q^4}\frac{1}{\sqrt{1+4x_B^2 M^2/Q^2}}\left|\mathcal{T}_{BH}+\mathcal{T}_{DVCS}\right|^2 \quad , \tag{5.14}$$

where y denotes the fractional energy of the virtual photon with respect to the beam energy.

The BH contribution can be calculated in QED including radiative corrections given the knowledge of electromagnetic form factors of the proton. In principle, the BH contribution can be subtracted but at HERMESkinematics the BH contribution dominates by far (fig. 5.3), so that a subtraction of the BH contribution would lead to large uncertainties. In addition, since at HERMESthe complete final state of the reaction cannot be detected unambiguously, the contributions from other processes might be significant. It is thus not yet feasible to measure the DVCS cross section at HERMESwith sufficient precision [10].

Another possibility to gain information on the DVCS contribution at HERMESkinematics is the resulting interference term

$$\mathcal{I} = \mathcal{T}_{BH}^{*}\mathcal{T}_{DVCS} + \mathcal{T}_{BH}\mathcal{T}_{DVCS}^{*} \quad , \tag{5.15}$$

which offers the opportunity to access the real and imaginary part of the DVCS amplitude $\mathcal{T}_{DVCS}$. These can eventually be expressed in terms of the target GPDs. The amplitudes describing the DVCS and BH processes can be expanded into a $1/Q$ power series [73]. All terms of the expansion can be expressed in moments $\langle\sin n\phi\rangle$ and $\langle\cos n\phi\rangle$ [75], with ϕ being the azimuthal angle between the scattering plane and the production plane, see fig. 5.4. The first sine and cosine moments are dominant with a $1/Q$ fall-off, while higher moments are at least suppressed like $1/Q^2$ [77]. The BH-DVCS interference term $\mathcal{I}$ depends then on the charge (e$_l$) and polarisation (P$_l$) of the incident lepton. For the leading moments it is given by [77]

$$\begin{aligned}\mathcal{I} \;&=\; \pm\tfrac{4\sqrt{2}\,M\,e^6}{t\,Q\,x_B}\tfrac{1}{\sqrt{1-x_B}}\cdot\Bigg(\cos\phi\tfrac{1}{\epsilon(\epsilon-1)}Re\mathcal{A} \\ &\qquad -P_l\sin\phi\sqrt{\tfrac{1+\epsilon}{\epsilon}}Im\mathcal{A}\Bigg) \quad ,\end{aligned} \tag{5.16}$$

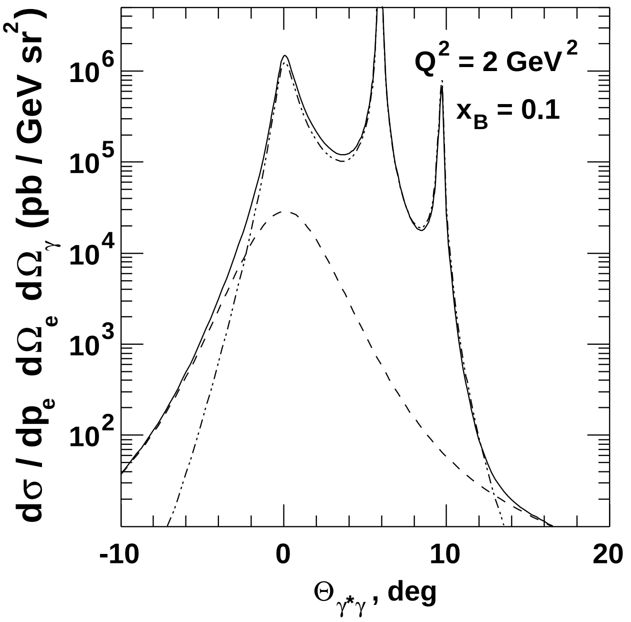

Figure 5.3: *Differential in-plane cross section as a function of the angle $\theta_{\gamma^*\gamma}$ for Deeply-Virtual Compton Scattering (DVCS) (dashed line), Bethe-Heitler (BH) (dashed-dotted line) and total photon production (solid line) in ep interaction in the* HERMES *kinematical regime for fixed values of x_B and Q^2 [10, 76].*

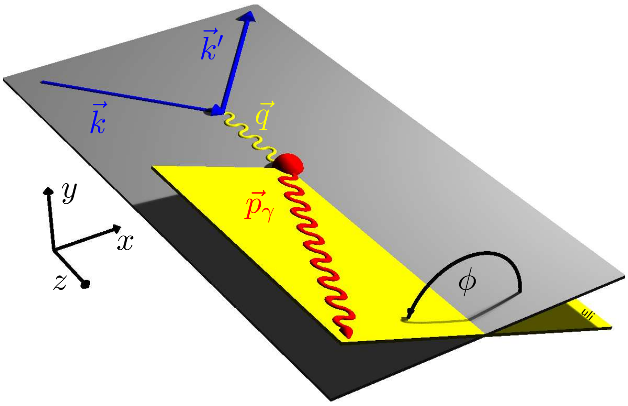

Figure 5.4: *Diagram of the Deeply-Virtual Compton Scattering (DVCS) kinematics. The scattering plane (grey) is defined by the incoming and scattered electron momentum vectors $\vec{k}$ and $\vec{k}'$. The production plane (yellow)is given by the virtual and real photon momentum vectors $\vec{q}$ and $\vec{p}_\gamma$. The angle between scattering and production plane defines azimuthal angle ϕ*

.

with ± denoting the beam charge, with ϵ connected to y via

$$\epsilon = \frac{1-y}{1-y+\frac{y^2}{2}} \quad , \tag{5.17}$$

and $\mathcal{A}$ being a helicity amplitude for which the real and imaginary parts are related to corresponding GPDs. According to eq. 5.16 the real part of $\mathcal{A}$ can be accessed by measuring with lepton beams of either charge, which is uniquely possible at HERA. The corresponding Beam Charge Asymmetry (BCA)

$$A_C(\phi) = \frac{d\sigma(e^+p) - d\sigma(e^-p)}{d\sigma(e^+p) + d\sigma(e^-p)} \sim \cos\phi \times \mathrm{Re}\mathcal{A} \tag{5.18}$$

exhibits a cos ϕ dependence. Preliminary results have been obtained [78] by HERMES which show the expected cos ϕ dependence is significantly different from zero,

$$A_C^{\cos\phi} = 0.063 \pm 0.029(stat.) \pm 0.026(sys.) \quad . \tag{5.19}$$

Furthermore, the imaginary part of $\mathcal{A}$ is accessible via scattering of longitudinally polarised lepton beams of either helicity. The corresponding Beam Spin Asymmetry (BSA)

$$A_{LU} = \frac{d\sigma(\vec{e}p) - d\sigma(\overleftarrow{e}\,p)}{d\sigma(\vec{e}p) + d\sigma(\overleftarrow{e}\,p)} \sim \sin\phi \times \mathrm{Im}\mathcal{A} \tag{5.20}$$

has been extracted by HERMES and the expected sin ϕ behaviour was established with the first moment [16]

$$A_{LU}^{\sin\phi} = -0.23 \pm 0.04(stat.) \pm 0.03(sys.) \tag{5.21}$$

being significantly different from zero.

5.2.2 DVCS on Nuclear Targets

The GPD formalism, introduced for an individual nucleon, can be extended to the whole nucleus. Studying GPDs and their modifications in nuclear matter opens the possibility of accessing spatial distributions of energy, angular momentum and shear forces inside the nucleus [79].

Using nuclei instead of nucleons as target introduces some implications for the description and interpretation of the results. First of all, the number of GPDs necessary to describe the hadronic target depends on the spin of nucleus [80]. For a spin-0 nucleus only 1 GPD (H^A) contributes at leading twist, which renders these nuclei ideal to study GPDs. In case of spin-1/2 nuclei 4 GPDs are necessary, similar to the case for a proton target discussed above. Spin-1 targets, like deuterium, involve already 9 GPDs. A theoretical overview and an approach to model these GPDs is given in [80].

Also the cross sections will change, as the nuclear form factor $F_A^{e.m.}$ modifies the BH contribution whereas the DVCS contribution is influenced by the atomic number A of the nucleus [81]. This imposes then consequences for both BCA and BSA results. In order to quantify the resulting nuclear effects, the ratio of the corresponding asymmetry measured with scalar nuclear and proton targets is introduced [82] in a first step in the limit $t \to 0$, i.e. the coherent DVCS process dominates and the nucleus stays intact. In case of the BSA, this ratio is given by

$$\frac{A_{LU}(\phi)}{A_{LU}^{proton}(\phi)} = \frac{H^p(\xi,\xi,0) - H^p(-\xi,\xi,0) + (A/Z-1)\,(H^n(\xi,\xi,0) - H^n(-\xi,\xi,0))}{H^p(\xi,\xi,0) - H^p(-\xi,\xi,0)}, \tag{5.22}$$

where H^p (H^n) denotes the proton (neutron) GPD H. An immediate consequence of this results is that the BSA for a nuclear target is larger than that for the proton due to the ”‘combinatoric”’ enhancement by the term $(A/Z-1)H^n$. This is also true in case of the BCA. Including now Fermi motion of the nucleons inside the nucleus leads to an additional enhancement of the ratios [82], see fig. 5.5.

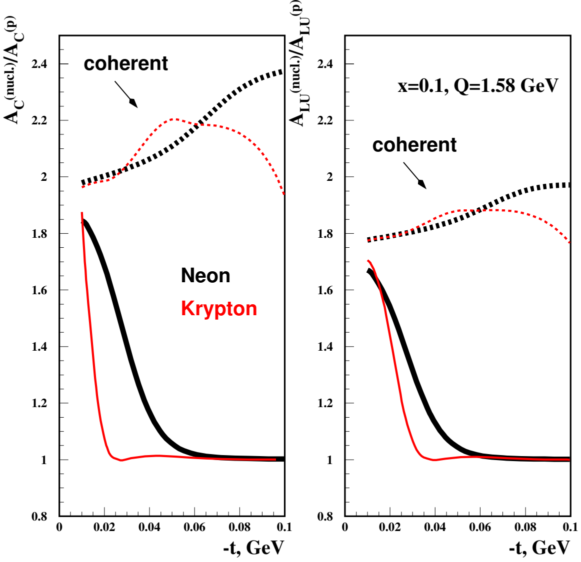

Figure 5.5: *Prediction for the ratio of Beam Charge Asymmetry (BCA) (left panel) and Beam Spin Asymmetry (BSA) (right panel) on nuclei with respect to the proton [82]. The dashed line corresponds to the purely coherent DVCS contribution. The rise of the ratios at large t is due to Fermi motion. The solid lines represents the sum of coherent and incoherent contributions. Including incoherent contributions leads to a steep decrease of the ratios, which is governed by the nuclear form factor.*

Considering then also the incoherent DVCS process where the nucleus breaks apart, the total cross section is modified and thus the above introduced ratios as well. The dominant incoherent part is then proportional to the number of protons times the GPD H of the free proton. This contribution has a slow t-dependence governed by the proton elastic form factor $F_1(t)$. The coherent part, on the other hand, has a much steeper t-dependence which is governed by the nuclear charge form factor $F_A^{e.m.}(t)$. The consequence of this is that, if the experimental set up does not allow for an extraction of the purely coherent DVCS contribution and includes also incoherent contributions, the ratios are predicted to approach unity when integrating over the momentum transfer t [82]. Especially at large values of $|t|$, where the coherent contribution is suppressed by the nuclear form factor, the ratio is significantly reduced, see fig. 5.5.

Chapter 6

Nuclear DVCS Analysis

In this analysis the Beam Spin Asymmetry (BSA) associated with the Deeply-Virtual Compton Scattering (DVCS) process is extracted from a variety of nuclear targets. The DVCS process is distinguished by the scattered DIS lepton and a single real photon without any other particles in the final state. Additional variables necessary to identify and describe the kinematics of the reaction are introduced. In order to guarantee thus the exclusivity of the reaction and obtain a clean sample of DVCS events, several cuts, which will be discussed in the following, have to be imposed on the preprocessed data.

Systematic studies performed to investigate background contributions and a comparison of different extraction methods for the BSA are discussed furthermore. Finally, the extracted BSA moments are compared with respect to the proton data, as discussed in the previous chapter.

6.1 Exclusive Variables

Additional variables necessary to select exclusive events from the recorded raw data are introduced and their calculation explained.

Two angles are important to the DVCS analysis. Firstly, the angle $\theta_{\gamma^*\gamma}$ between the virtual and the real photon, which is is given by

$$\theta_{\gamma^*\gamma} = \arccos\left(\frac{\vec{q}\cdot\vec{q}\,'}{|\vec{q}|\cdot|\vec{q}\,'|}\right), \tag{6.1}$$

with the three-momentum vector $\vec{q}$ of the virtual photon being determined from the incoming and scattered lepton and $\vec{q}\,'$ being the three-momentum vector of the real photon. Secondly, the azimuthal angle ϕ between the scattering and the production plane, which plays a central role in the determination of the asymmetry, is defined as

$$\phi = \arccos\left(\frac{\left(\vec{q}\times\vec{k}'\right)(\vec{q}\times\vec{q}\,')}{\left|\vec{q}\times\vec{k}'\right|\,|\vec{q}\times\vec{q}\,'|}\right)\cdot\frac{\vec{q}\,'\cdot(\vec{q}\times k')}{|\vec{q}\,'\cdot(\vec{q}\times k')|} \quad , \tag{6.2}$$

where $\vec{k}'$ denotes the three-momentum vector of the scattered electron. The BSA associated with the DVCS process manifests itself in the distribution of the azimuthal angle ϕ as discussed in sec. 5.2.

In this analysis, the proton mass m_p is assumed in the calculation of kinematic variables instead of the mass m_N of the target nucleus. In principle, the target mass depends on the kind of process taking place as both coherent and incoherent processes occur in parallel. For the coherent process it is more appropriate to use m_N, as for the incoherent process m_p is the correct choice. However, substituting the nuclear mass m_N in case of the coherent process by the nucleon mass m_p simplifies the analysis, since all cuts applied to kinematical variables can be kept at the same values. Previous studies [86, 87] showed, that using m_p instead of m_N in case of the coherent process does not yield any significant differences and thus the above stated substitution of m_N by m_p is justified. It also enables the use of kinematical cuts derived for the analysis of DVCS on a nucleon [10, 88].

The Mandelstam variable t, describing the momentum transfer to the nuclear target, can be calculated, according to eq. 5.13, using the virtual and real photon four momenta q and q', which yields

$$t = (q - q')^2 = -Q^2 - 2E_\gamma\,(\nu - |\vec{q}|\cos\theta_{\gamma^*\gamma}) \quad , \tag{6.3}$$

where E_γ is the real photon energy determined by the calorimeter. The t resolution, similar to the missing mass M_x, is dominated by the resolution of the measurement of real photons. Due to the limited resolution of the calorimeter, also positive values for t can be obtained which bear no physical meaning. The resolution, however, can be improved under the assumption that for exclusive events the missing mass M_x is equivalent to the nucleon mass m_p. In this case, a *constrained* momentum transfer t_c can be calculated according to

$$t_c = \frac{-Q^2 - 2\nu\left(\nu - \sqrt{\nu^2 + Q^2}\cos\theta_{\gamma^*\gamma}\right)}{1 + \frac{1}{m_N}\left(\nu - \sqrt{\nu^2 + Q^2}\cos\theta_{\gamma^*\gamma}\right)} \quad , \tag{6.4}$$

avoiding the use of E_γ, since the resolution of the spectrometer, which determines the accuracy of the inclusive kinematical variables Q^2 and ν , is superior to the energy resolution of the calorimeter. This method is in principle correct in case of a three-particle final state [87], whereas for semi-inclusive background events t_c is meaningless. Also unphysical values are avoided by this method.

As the HERMES spectrometer is not capable of detecting the complete final state of DIS events, a missing mass technique is employed to determine the exclusive data set. The missing mass of a reaction can be calculated from the four momenta of the initial target nucleon (nucleus) p and the virtual and real photon :

$$\begin{aligned} M_x^2 &= (q + p - q')^2 \\ &= m_p^2 + 2\,m_p(\nu - E_\gamma) + t \quad . \end{aligned} \tag{6.5}$$

Similar to the momentum transfer t the calorimeter resolution may lead to negative values of M_x^2. In this case the missing mass M_x will be defined as

$$M_x^2 < 0 \Rightarrow M_x = -\sqrt{-M_x^2} \quad . \tag{6.6}$$

6.2 Event Selection

The aim of this analysis is to study DVCS processes, which require a scattered lepton and a real photon in the detector acceptance, and extract the associated BSA. Apart from cuts selecting DIS leptons and real photons, several other cuts are necessary to ensure the exclusivity of the reaction, since the full final state is not reconstructed by the HERMES spectrometer. In addition, the status of the detector components has to be taken into account to ensure perfect conditions during data taking. Inefficiencies or malfunctioning of important detector components might otherwise lead to false asymmetries. In the following, all necessary cuts are discussed in detail and the resulting data sets for all nuclear targets are shown.

6.2.1 Data Quality

HERMES data sets are organised in runs and bursts. A run is determined by a data file size of approximately 450 MB, corresponding to 5–30 min of data taking, depending on the beam current and the target density. A run, in turn, is subdivided into bursts. A burst lasts about 10 s and is associated to the so-called *slow-control* data, which gives information about the status of each spectrometer component including the target and is recorded every 10 s. This information is used to create a bit pattern indicating the detector status during a burst.

The usable runs for this analysis are selected according to the target status, requiring unpolarised running of certain gas types given in tab. 6.2. The bit pattern `0x503E13DC` is used to extract all analysable bursts. In addition to this bit pattern further conditions are imposed on each burst to ensure reasonable beam conditions and DAQ status. All selection criteria applied on the burst level are summarised in tab. 6.1.

For data taken in 2004 with Krypton and Xenon gas, several runs had to be discarded [95] due to problems with the tracking chambers, despite passing the above mentioned burst level cuts. All remaining bursts are then analysed with respect to exclusive DVCS processes. The procedure necessary to separate those events are described in the following.

6.2.2 DIS Event selection

A fundamental component of the DVCS analysis is the reconstruction of the scattered DIS lepton, e.g. the kinematics of the virtual photon and subsequently t_c and M_x are derived from it. In addition, the number of recorded DIS events is essential for normalisation purposes.

Table 6.1: *Selection criteria applied to data on burst level. The selected bit pattern summarises the conditions below.*

bit pattern `0x503E13DC`
run was marked as analysable in the logbook
no HV trips in the tracking chambers
no dead blocks in the calorimeter
preshower detector is working properly
TRD is fine during burst
DAQ live time is greater than 0.8
burst is not the first one in a run
beam current is reasonable (5 mA < I < 50 mA)
beam polarisation measurement not more than 300 s ago

additional conditions
live time for trigger 21 is between 0.8 and 1
raw luminosity is between 5 and 3000
beam polarisation is between 30% and 80%

First of all, the event has to be recorded due to the standard DIS trigger 21, which is discussed in detail in sec. 2.2.4. After the triggering particle is identified as lepton by $\mathrm{PID}_2 + \mathrm{PID}_5 > 2$, where PID_2 is derived analogously to PID_3, which is explained in sec. 2.2.3, by

$$\mathrm{PID}_2 = \log_{10}\left(\frac{P^e_{Cal}P^e_{Pre}}{P^h_{Cal}P^h_{Pre}}\right) \quad , \tag{6.7}$$

which corresponds to a 100 times larger probability that the particle is a lepton and not a hadron, cuts due to the detector geometry are applied. PID_5 contains PID information obtained by the TRD. The track has to pass through the magnet opening and traverse the full length of the spectrometer. Moreover, the track may not hit the calorimeter at the edges, as the shower will not be contained inside the calorimeter. The reconstructed x- and y-position of the lepton cluster has therefore to fulfil the following conditions:

$$\begin{aligned} &|x_{cluster}| &< 175\,cm \\ 30\,cm < \; &|y_{cluster}| &< 108\,cm \quad . \end{aligned} \tag{6.8}$$

In order to reduce external background like scattering on collimators, loose cuts on the reconstructed vertex position are imposed:

$$\begin{aligned} -18\,cm < \; &z_{vertex} &< 18\,cm \\ &|t_{vertex}| &< 0.75\,cm \quad . \end{aligned} \tag{6.9}$$

Furthermore, cuts on inclusive kinematical variables are introduced to assure the correct event characteristics. The momentum transfer Q^2 has to be large in order to obtain a hard virtual photon and the invariant mass W of the virtual photon-nucleon system needs to be large enough to avoid the resonance region:

$$\begin{array}{l} Q^2 > 1\, GeV^2 \\ W^2 > 9\, GeV^2 \quad . \end{array} \tag{6.10}$$

In addition the energy ν of the virtual photon may not exceed 22 GeV, which improves the comparability of data sets from different years [88, 10].

6.2.3 Single Photon Events

Only events containing a scattered DIS lepton and without further tracks inside the acceptance are considered in the search for single photon events. Photons cause untracked clusters in the calorimeter, i.e. no charged particle track can be associated by the HERMES Reconstruction (HRC) program. As defined by the DVCS final state, only one reconstructed photon per event is allowed. Furthermore, like in case of leptons, the photon kinematics has to satisfy certain conditions in order to accept the event. The photon has to pass the spectrometer magnet opening, which translates into restrictive cuts on the reconstructed position of the cluster. Additionally, the cluster may not be too close to the edge of the spectrometer for the same reason as the lepton cluster. Therefore, a cut on the cluster position is introduced:

$$\begin{array}{rcl} & |x_{cluster}| & < 125\, cm \\ 33\, cm < & y_{cluster} & < 105\, cm \end{array} \tag{6.11}$$

In addition a cut on the associated signal in the preshower detector of $E_{pre} > 1\,\text{MeV}$ is imposed. The preshower cut helps to reduce background from the proton beam, since such showers enter the calorimeter from the back and do not hit necessarily the preshower detector [88]. On the other hand, this cut enhances the determination of the impact point of the photon on the calorimeter. A signal in the preshower signal ensures, that a traversing photon has been converted into an e^+/e^- pair. Electrons have a much smaller mean free path length compared to photons [28], so that the z-position of the electromagnetic shower is more precisely known.

6.2.4 Exclusive Events

For the selection of exclusive events only events with exactly one reconstructed track corresponding to a DIS lepton and one real photon passing the above introduced cuts are taken into account. The kinematical variables and angles described in sec. 6.1 are calculated for these events and corresponding constraints are established.

The angle $\theta_{\gamma^*\gamma}$ is limited to an upper value of 45 mrad, which corresponds to a complete coverage of the azimuthal angle ϕ within the acceptance of the calorimeter for photons and suppresses background predominantly present at larger values of $\theta_{\gamma^*\gamma}$. A lower cut had to be placed due to smearing effects, which limit the angular resolution, to 2 mrad [91].

For the momentum transfer $|t_c|$ an upper limit of $0.7\,\mathrm{GeV}^2$ is given due to background conditions [88, 10]. Moreover, the factorisation theorem for DVCS requires that $|t| << Q^2$.

Finally, a cut on the missing mass M_x complements the constraints to select exclusive events. The actual boundaries of

$$-1.5\,GeV < M_x < 1.7\,GeV \tag{6.12}$$

were determined by optimising the signal-to-background ratio with respect to semi-inclusive background events [10, 88]. The squared missing mass M_x^2 distribution for a Neon target is shown in fig. 6.1 a. Within the selected M_x region a significant BSA is observed (see fig. 6.1 b) whereas for the higher M_x-region the BSA vanishes, which supports the selection of exclusive events by this method.

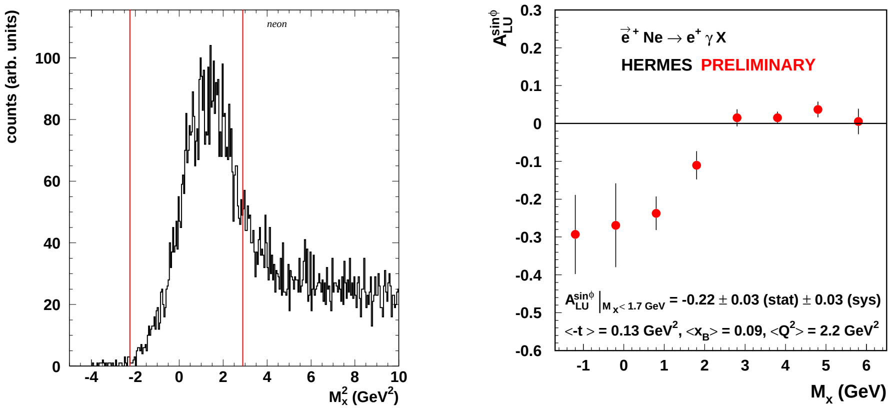

(a) (b)

Figure 6.1: *Missing mass distribution and cuts used for exclusive event selection (Neon target):*
(a) Squared missing mass M_x^2 *distribution, cuts for exclusive event selection are indicated by vertical lines;*
(b) Dependence of $\sin\phi$*-moment of the Beam-Spin Asymmetry (BSA) on missing mass* M_x*. Within the exclusive bin a significant BSA is observed whereas for the higher* M_x*-region the BSA vanishes.*

The remaining events passing all these cuts are then used in the further analysis of the BSA associated with DVCS.

6.2.5 Data Sets

All data sets used throughout this analysis were obtained between 1999 and 2004, using a positron beam. The gathered raw statistics, given in number of DIS events and the corresponding luminosity not taking into account above mentioned constraints for exclusive events, is shown in tab. 6.2. Also of interest is the isotope composition for the individual nuclear targets, since different isotopes may carry a different nuclear spin which is important to the theoretical interpretation. Apart from Xenon all target gases consist mainly of isotopes bearing the same nuclear spin.

Table 6.2: *Data sets for different nuclear targets at* HERMES. *Isotope abundances according to [93]. Corresponding nuclear spin of isotopes is taken from [94]. The number of DIS events and corresponding integrated luminosity not taking exclusive cuts into account are given as well.*

target	DIS [10^6]	luminosity [pb^{-1}]	isotopes	spin
Hydrogen	6.850	132.5		1/2
Deuterium	3.312	80.8		1
Helium	1.454	32.4	^{4}He (99.9%)	0
Nitrogen	1.919	51.4	^{14}N (99.6%)	1
Neon	3.800	85.9	^{20}Ne (90.5%)	0
			^{22}Ne (9.3%)	0
Krypton	2.682	74.9	^{84}Kr (57.0%)	0
			^{86}Kr (17.3%)	0
			^{82}Kr (11.6%)	0
			^{83}Kr (11.5%)	9/2
			^{80}Kr (2.3%)	0
Xenon	1.086	32.5	^{132}Xe (26.9%)	0
			^{129}Xe (26.4%)	1/2
			^{131}Xe (21.2%)	3/2
			^{134}Xe (10.4%)	0
			^{136}Xe (8.9%)	0
			^{130}Xe (4.1%)	0
			^{128}Xe (1.9%)	0

In case of the Krypton data set, two subsets from different running periods (1999, 2004) exist. Prior to merging these subsets, the statistical agreement of distributions for inclusive and exclusive variables — $Q^2, x_B, \theta_{\gamma^*\gamma}, t_c$ (see fig. 6.2 a) and M_x^2 — of both data sets has been confirmed using the Kolmogorov-Smirnov Test (KST), which is especially sensitive to changes in the shape of distributions [96]. Applying the KST also to the ϕ-distribution (see fig. 6.2 b) leads to a negative result which is anticipated as both beam helicity states contribute differently to the subsets.

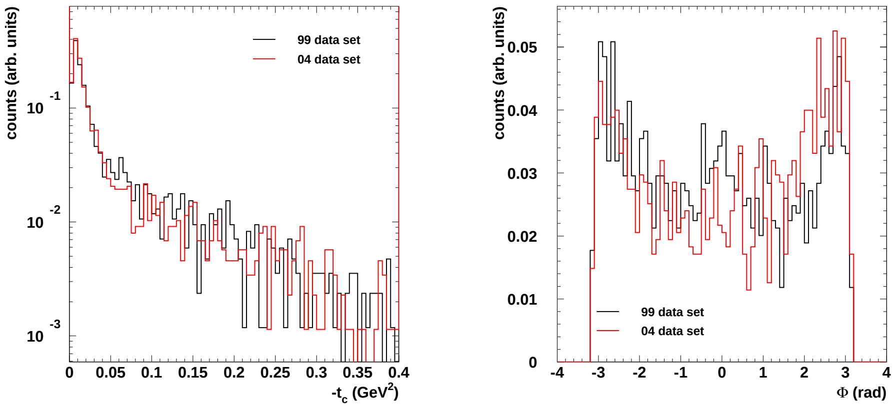

(a) (b)

Figure 6.2: *Comparison of Krypton data sets from 1999 and 2004:*
(a) Distribution of the momentum transfer $-t_c$*, both data sets agree according to the Kolmogorov-Smirnov Test (KST);*
(b) Distribution of the azimuthal angle ϕ*, both data sets disagree since the 1999 data set contains only one beam helicity state.*

Applying all previous discussed constraints for the selection of exclusive events to the data sets presented in tab. 6.2, the exclusive data sets for each target have been obtained. All relevant numbers are given in tab. 6.3 including the number of DIS events per helicity state, as a later normalisation depends on their ratio.

6.3 Data Analysis

After determining the exclusive data set for each target, the BSA associated with the DVCS process has to be extracted. Due to, in terms of helicity, highly unbalanced data sets and limited statistics, binned and unbinned extraction techniques are introduced and will be described in the following. Furthermore, studies aiming to estimate systematic error contributions are presented, before the final results are presented.

6.3.1 Extraction Methods

In case of a binned extraction technique, the range of the azimuthal angle ϕ is subdivided into ten bins, which is the optimum number of bins given the present statistics [86, 90]. The asymmetry A_{LU} is then calculated for each bin in ϕ by

$$A_{LU}(\phi) = \frac{1}{\langle P \rangle} \frac{w^+ N^+(\phi) - w^- N^-(\phi)}{w^+ N^+(\phi) + w^- N^-(\phi)} \quad , \tag{6.13}$$

counting the corresponding exclusive events N^+, N^-, where +(-) denotes a positive (negative) beam helicity, $\langle P \rangle$ the mean polarisation of the beam and the

Table 6.3: *Exclusive data sets used for nuclear DVCS analysis. The number of DIS events is also given per helicity state since a later normalisation depends on their ratio.*

target	DIS [10^6] total	helicity$^+$	helicity$^-$	excl. events
Hydrogen	5.048322	1.860780	3.187542	8229
Deuterium	2.024361	0.842588	1.181773	2254
Helium	1.039724	0.127705	0.867019	1380
Nitrogen	0.956855	0.030878	0.925977	1531
Neon	2.823240	1.326821	1.496419	5052
Krypton	1.721255	1.259982	0.461273	3220
Xenon	0.627903	0.236455	0.391448	1091

weights w^+, w^- are given by

$$w^{+(-)} = \frac{1}{N_{DIS}^{+(-)}} \quad , \tag{6.14}$$

with $N_{DIS}^{\pm}$ being the number of DIS events for each helicity state. This method requires nearly equally populated beam helicity states as otherwise the mean polarisation is ill defined.

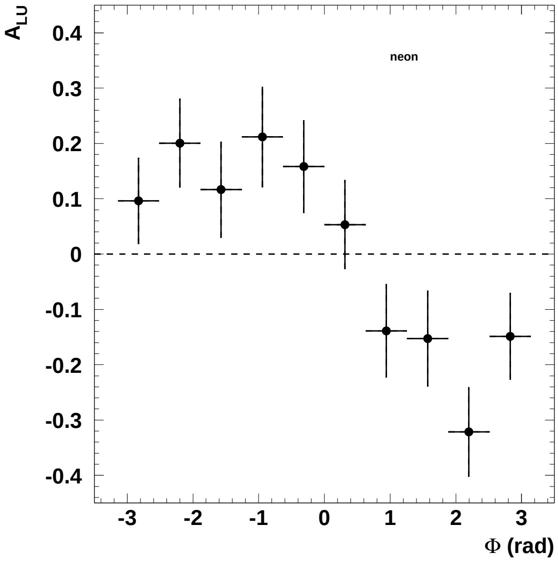

Figure 6.3: *Azimuthal dependence of the Beam-Spin Asymmetry (BSA) extracted using the binned method (shown for the Neon target).*

As some targets do not fulfil this requirement, see tab. 6.3, a modified method, being called the Anti-Symmetrisation (AS) method, is introduced. The AS method is characterised by mapping the region $[-\pi, 0]$ to the region $[0, \pi]$, thereby projecting out the odd part in ϕ and eliminating possible even harmonics stemming from helicity-dependent acceptance effects [86]. The data set is divided according to the beam helicity and the asymmetry A_{LU} is calculated for each helicity state separately, assuming a symmetric detector acceptance for both intervals of ϕ:

$$A_{LU}^{+(-)}(\phi) = \frac{1}{|P^{+(-)}|} \frac{N^{+(-)}(\phi) - N^{+(-)}(-\phi)}{N^{+(-)}(\phi) + N^{+(-)}(-\phi)} \quad . \tag{6.15}$$

Both asymmetries can then be combined according to

$$A_{LU}(\phi) = \frac{N_{DIS}^{+} A_{LU}^{+}(\phi) - N_{DIS}^{-} A_{LU}^{-}(\phi)}{N_{DIS}^{+} + N_{DIS}^{-}} \tag{6.16}$$

with $N_{DIS}^{\pm}$ as defined above serving as normalisation factor (see fig. 6.3). The resulting A_{LU}-distribution is then described by

$$A_{LU}(\phi) = p_0 \sin\phi + p_1 \sin 2\phi \quad , \tag{6.17}$$

using a χ^2-minimisation technique [97] to obtain the best values p_0 and p_1 for the $\sin\phi$ moments. Given the limited statistics available for most nuclear targets, an additional binning in the kinematical variables — t_c, Q^2 and x_B — which is necessary to study the kinematic dependence of the BSA, would lead to bins with few or even no events, thus rendering the above introduced binned extraction method useless.

Therefore, an Anti-Symmetrised Maximum Likelihood (ML) method is introduced, avoiding a binning in the azimuthal angle ϕ. The so-called likelihood function

$$L(a) = \prod_i f(x_i|a) \quad , \tag{6.18}$$

with $f(x_i|a)$ being the normalised probability density function for all measurements x_i given the parameter set a, is formed and maximised in order to obtain the best estimation of a [96]. In case of the exclusive data sample corresponding to the BSA measurement, the probability density function for each helicity state can be written as [91]

$$f^{\pm}(\phi_i|a) \simeq \frac{\epsilon(\phi_i) \cdot \sigma_{UU}(\phi_i) \cdot [1 \pm |P^{\pm}| \, A_{LU}(\phi_i|a)]}{C^{\pm}(a)} \quad , \tag{6.19}$$

$\pm$ denoting the beam helicity state, $P_i^{\pm}$ being the beam polarisation, ϵ corresponds to the detection efficiency, σ_{UU} is the cross section for unpolarised beam and target and $C^{\pm}$ is the normalisation integral necessary to maintain a correct normalisation of $f(\phi_i|a)$. A_{LU} describes the azimuthal dependence of the BSA amplitude, its parametrisation is given in eq. 6.17. Since σ_{UU} and ϵ do not depend on the parameter set a, they may be dropped from the numerator of the likelihood. Again, as described above, the data set is then divided according to the beam helicity. A reduced likelihood for each interval of ϕ per helicity state, indicated by $\pm$, can be obtained by

$$\begin{aligned} L^{\pm}_{[0,\pi]}(a) &= \prod_i \frac{1 \pm |P_i^{\pm}| \cdot A_{LU}(\phi_i|a)}{C^{\pm}_{[0,\pi]}(a)} \\ L^{\pm}_{[-\pi,0]}(a) &= \prod_i \frac{1 \pm |P_i^{\pm}| \cdot A_{LU}(\phi_i|a)}{C^{\pm}_{[-\pi,0]}(a)} \quad . \end{aligned} \tag{6.20}$$

The corresponding normalisation integrals are found to be equal under the assumption of symmetric acceptance and efficiency functions with respect to ϕ and are given by [91]

$$C^{\pm}_{[0,\pi]} = C^{\pm}_{[-\pi,0]} = \frac{\sum_i 1 \pm |P_i^{\pm}| \cdot A_{LU}(\phi_i|a)}{N^{\pm}_{DIS}} \quad . \tag{6.21}$$

The likelihood function for each helicity state can be found by combining the respective likelihood functions of both ϕ-intervals:

$$L^{\pm}(a) = L^{\pm}_{[0,\pi]}(a) \cdot L^{\pm}_{[-\pi,0]}(a) \quad . \tag{6.22}$$

If a data set contains both beam helicity states, they can be combined as well to form the full likelihood function

$$L(a) = L^{+}(a) \cdot L^{-}(a) \quad . \tag{6.23}$$

For large data sets, e.g. Neon, both binned and ML methods yield the same results, see fig.6.4. However, for small data sets the binned method might bias the results, because the χ^2 minimisation assumes normal distributions for the error calculation, which might not be given. Therefore, the ML method will be used throughout this analysis.

6.3.2 Systematic Studies

Since the event selection for this analysis solely depends on trigger 21, inefficiencies of the H0 hodoscope, which have been reported earlier [89], have been studied within the DVCS analysis group [86, 90, 91]. Due to local inefficiencies a false asymmetry may arise. The found inefficiencies, which were found to vary within 1% over the hodoscope area, have a negligible influence on the extracted asymmetries and are therefore neglected in the further analysis.

Due to the finite kinematic resolution, which is limited by the calorimeter, the exclusive sample will not only include contributions from the exclusive coherent reaction on the nucleus and from incoherent production off protons and neutrons in the nucleus but also semi-inclusive processes. MC studies show that 75% of the semi-inclusive background events in the exclusive sample are one-photon hits [88] which stem predominantly from π°decays where one photons escapes detection due to the limited acceptance of the HERMES spectrometer. A possible contribution of π°decays to the measured BSA is therefore studied. The same selection

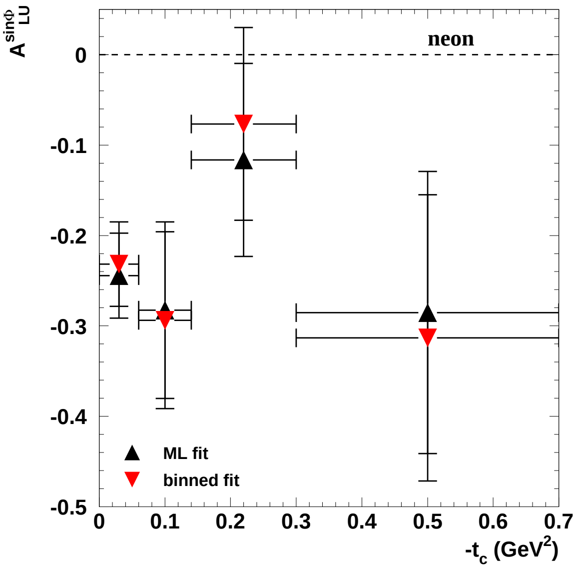

Figure 6.4: *Comparison of Maximum Likelihood (ML) and binned extraction method using the Neon data set. Both methods yield comparable results and error bars, which is expected due to the large number of exclusive events (see tab. 6.3). In the following analysis the ML method will be used.*

cuts were applied as for the DVCS analysis, but up to 10 trackless clusters instead of only one were allowed. π°selection is then achieved by reconstructing the invariant mass M_{inv} of all possible combinations of two out of all detected photons and requiring

$$0.1\,GeV < M_{inv} < 0.17\,GeV \quad . \tag{6.24}$$

In addition, the missing mass constrained was abandoned and a cut on

$$z_{\pi^\circ} = \frac{E_{\pi^\circ}}{\nu} > 0.8 \tag{6.25}$$

is introduced, thereby increasing the available statistics. The resulting asymmetry is extracted for the more energetic photon out of the π°decay. Since no strong kinematical dependence of the asymmetry is observed [10, 90], the integrated value is taken for correction. The asymmetry itself is extracted using the ML method, all results are given in tab. 6.4. The contribution

$$\delta_{\pi^\circ} = \left|\frac{1}{1-\eta}A_{meas} - \frac{\eta}{1-\eta}A_{\pi^\circ}^{max}\right| - |A_{meas}| \tag{6.26}$$

of the π°asymmetry to the systematic error is evaluated by taking into account the fraction η of semi-inclusive processes present in the exclusive data sample [90]. η is estimated by using Monte Carlo (MC) studies [90, 91]. A_{meas} is the extracted

Table 6.4: *Extracted values of the π°asymmetry using the Maximum Likelihood (ML) method. For Xenon no asymmetry could be extracted due to the limited available statistics.*

target	events	z_{π°	$\mathrm{A}_{LU}^{\sin\phi}$	$\mathrm{A}_{LU}^{\sin 2\phi}$
Hydrogen	1205	0.892±0.002	-0.085±0.072	0.046±0.077
Deuterium	1553	0.884±0.003	0.162±0.071	-0.104±0.074
Helium	260	0.883±0.070	0.10±0.16	-0.13±0.17
Nitrogen	189	0.886±0.065	0.02±0.23	-0.04±0.24
Neon	559	0.884±0.069	-0.05±0.11	-0.05±0.11
Krypton	242	0.887±0.004	-0.03±0.21	0.03±0.22
Xenon	71	0.886±0.075	–	–

asymmetry for a given target and $A_{\pi^\circ}^{max}$ denotes the maximum asymmetry for the pion background (see tab. 6.4) taking into account the errors as well.

Further studies on the impact of misalignment and miscalibration have been performed [91, 92], which are not part of this work and are therefore omitted and only their results will be given. The systematic error is calculated from the contributions of π°asymmetry, misalignment and miscalibration. Since for the Xenon target no value for the π°asymmetry is available the value of the Krypton target is taken instead as an estimate. The systematic errors for each target are given in appendix C.1.

6.4 Results

According to theoretical predictions, see chap. 5.2.2, an enhancement of the Beam Spin Asymmetry (BSA) is expected for heavy nuclear targets in case of coherent processes. Since the complete final state is not reconstructed by the HERMES spectrometer, a distinction of coherent and incoherent processes is not possible. However, at small momentum transfer $|t_c|$ coherent processes on the nucleus dominate since the electromagnetic form factor of the nucleus is large compared to hydrogen. This leads to an enhancement of the yield of exclusive events at small $|t_c|$ for heavy nuclei compared to a hydrogen target, see fig. 6.5.

The available statistics (cf. tab 6.3) allows only for a coarse binning of the $-t_c$ region. The $-t_c$-range is subdivided into four bins and the BSA is extracted for each bin accordingly. The results for each target and bin are given in tab. 6.5 as well as the mean value of $-t_c$ and the statistical and systematical errors.

The extracted values for the $\sin\phi$-moment of the BSA with respect to $-t_c$ is shown for light (see fig. 6.6) and heavy nuclei (see fig. 6.7). The inner error bars denote the statistical error whereas the outer error bars denote the total error including systematic contributions. The statistical error is the dominant source. For all targets, significant $\sin\phi$-moments for the BSA are obtained.

A matter of particular interest is the dependence of the coherent part of the

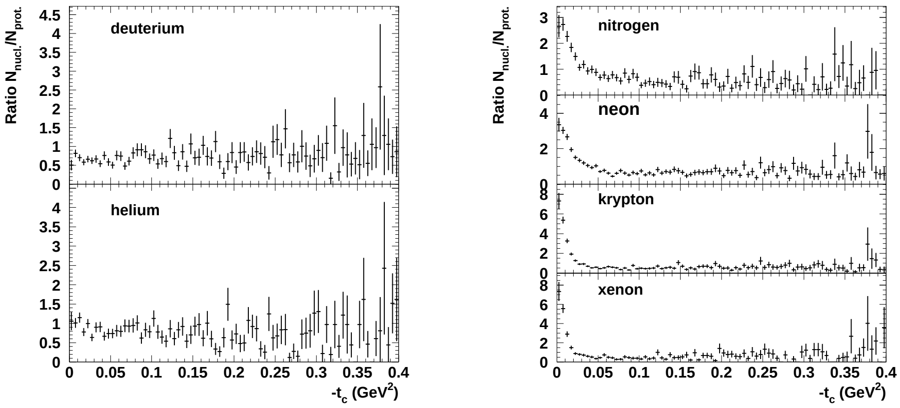

(a) (b)

Figure 6.5: *Ratio of yields of exclusive events for nuclear targets compared to hydrogen target as a function of the momentum transfer t_c. The yields are nomalised with respect to the corresponding number of DIS events (N_{DIS}):*

(a) for light nuclei (D, He) no enhancement at small t_c is observed;

(b) for heavy nuclei (N, Ne, Kr and Xe) a mass dependent enhancement is observed.

BSA on the nuclear number A. Therefore, the $\sin\phi$-moments of the first bin — containing a large fraction of coherent processes in case of nuclear targets (see tab. 6.5) — for each target are compared, see fig. 6.8. There is no significant shift of the $\sin\phi$-moment visible. A systematic increase for heavy targets compared to hydrogen can be observed. For the remaining t_c-bins (see fig. 6.9) no such shift is recognised, being consistent with theoretical predictions that, at larger values of $-t_c$, incoherent processes prevail which yield a BSA comparable to hydrogen.

A quantitative theoretical interpretation of the observed nuclear BSAs requires a detailed understanding of the incoherent cross section contributions and incoherent asymmetries at small $|t_c|$ values, so that the coherent contribution can be extracted. This requires further theoretical model calculations. The future recoil data from HERMES will deliver more precise data for hydrogen at small $|t_c|$, so that then the nuclear data can be compared to proton data at comparable small $\langle|t_c|\rangle$ and model predictions can be tested.

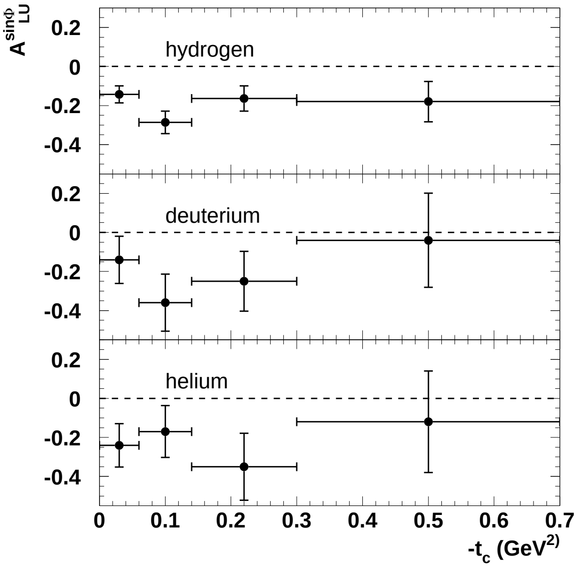

Figure 6.6: $\sin\phi$*-moment of the Beam-Spin Asymmetry (BSA) for light nuclei (H, D and He) for each* $-t_c$*-bin. The error bars denote the total error including systematic contributions (The statistical contribution to the the total error dominates).*

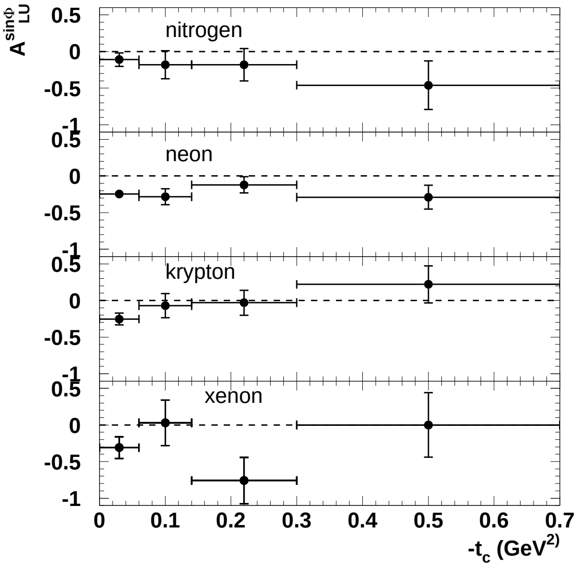

Figure 6.7: $\sin\phi$*-moment of the Beam-Spin Asymmetry (BSA) for heavy nuclei (N, Ne, Kr and Xe) for each* $-t_c$*-bin. The error bars denote the total error including systematic contributions (The statistical contribution to the the total error dominates).*

Table 6.5: *$\sin\phi$-moments $A_{LU}^{\sin\phi}$ of the Beam-Spin Asymmetry (BSA) for all nuclear targets. The range for each bin in $-t_c$ is given as well as the mean value $\langle -t_c\rangle$. In addition, the fraction of coherent processes $\eta_{coh.}$ per bin, which are extracted from Monte Carlo simulations [91], is stated. Statistical ($\delta_{stat.}$) and systematical ($\delta_{sys.}$) contributions to the total error are given separately. Corrections due to the finite $\theta_{\gamma^*\gamma}$ resolution are not included.*

target	$-t_c$	$\langle -t_c\rangle$	$\eta_{coh.}$	$\mathrm{A}_{LU}^{\sin\phi}$	$\delta_{stat.}$	$\delta_{sys.}$
hydrogen	0.00 – 0.06	0.029	–	-0.143	0.043	0.006
	0.06 – 0.14	0.095	–	-0.286	0.055	0.018
	0.14 – 0.30	0.204	–	-0.164	0.064	0.011
	0.30 – 0.70	0.419	–	-0.18	0.10	0.026
deuterium	0.00 – 0.06	0.029	0.436	-0.14	0.12	0.011
	0.06 – 0.14	0.097	0.133	-0.36	0.14	0.042
	0.14 – 0.30	0.201	0.044	-0.25	0.15	0.028
	0.30 – 0.70	0.403	0.039	-0.04	0.24	0.015
helium	0.00 – 0.06	0.027	0.558	-0.24	0.11	0.014
	0.06 – 0.14	0.093	0.245	-0.17	0.13	0.026
	0.14 – 0.30	0.202	0.081	-0.35	0.17	0.024
	0.30 – 0.70	0.420	0.066	-0.12	0.26	0.014
nitrogen	0.00 – 0.06	0.022	0.769	-0.111	0.091	0.006
	0.06 – 0.14	0.091	0.134	-0.18	0.18	0.060
	0.14 – 0.30	0.200	0.167	-0.18	0.22	0.020
	0.30 – 0.70	0.417	0.22	-0.46	0.32	0.090
neon	0.00 – 0.06	0.022	0.732	-0.244	0.047	0.023
	0.06 – 0.14	0.096	0.113	-0.283	0.098	0.048
	0.14 – 0.30	0.206	0.111	-0.12	0.11	0.018
	0.30 – 0.70	0.424	0.313	-0.29	0.16	0.033
krypton	0.00 – 0.06	0.016	0.771	-0.253	0.069	0.039
	0.06 – 0.14	0.094	0.172	-0.07	0.16	0.035
	0.14 – 0.30	0.205	0.191	-0.03	0.17	0.021
	0.30 – 0.70	0.425	0.502	0.22	0.25	0.027
xenon	0.00 – 0.06	0.016	0.775	-0.31	0.14	0.045
	0.06 – 0.14	0.097	0.178	0.03	0.31	0.039
	0.14 – 0.30	0.206	0.264	-0.76	0.30	0.095
	0.30 – 0.70	0.399	0.549	-0.00	0.44	0.019

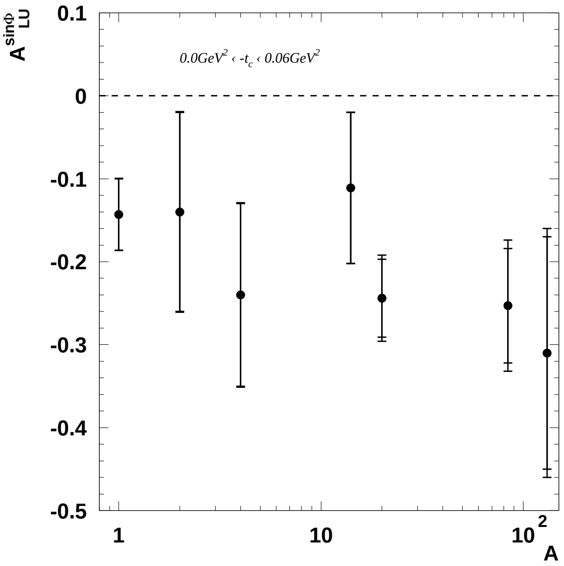

Figure 6.8: *A-dependence of* $\sin\phi$*-moment of the Beam-Spin Asymmetry (BSA) in the first* $-t_c$*-bin (0.00 – 0.06GeV*^{2}*), which contains mostly coherent processes for heavy targets (N, Ne, Kr and Xe), see tab. 6.5. The inner error bars denote the statistical error whereas the outer error bars denote the total error including systematic contributions.*

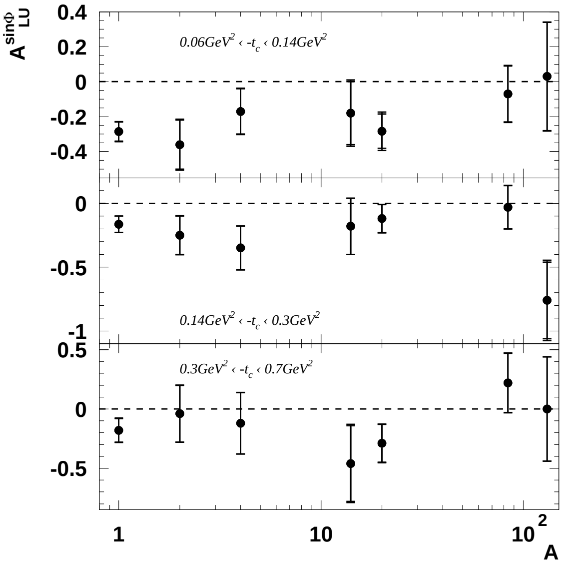

Figure 6.9: *A-dependence of* $\sin\phi$*-moment of the Beam-Spin Asymmetry (BSA) in the remaining* $-t_c$*-bins, which contain mostly incoherent processes for heavy targets (N, Ne, Kr and Xe), see tab. 6.5. The error bars denote the total error including systematic contributions (The statistical contribution to the the total error dominates).*

Chapter 7

Conclusions

The beam-spin azimuthal asymmetry associated with the Deeply-Virtual Compton Scattering-Bethe Heitler (DVCS-BH) interference has been measured for the first time for a variety of nuclear targets. HERMES offers, due to its storage cell for gaseous targets and the longitudinally polarised electron beam of HERA, an unique possibility to measure DVCS on nuclei. The DVCS process offers the cleanest access to Generalised Parton Distributions (GPD) and the modifications of GPDs in nuclear matter open the possibility of linking nuclear and partonic degrees of freedom by accessing spatial distributions of energy, angular momentum and shear forces inside the nucleus [79].

Significant $\sin\phi$-moments of the beam-spin azimuthal asymmetry are extracted for a variety of nuclei — H, D, He, Ne, Kr and Xe — and a systematic enhancement of the beam-spin azimuthal asymmetry with respect to the nuclear number A is observed. However, a comparison of the coherent $\sin\phi$-moments of heavy nuclei to hydrogen proves to be difficult for several reasons: Firstly, no purely coherent sample is available for nuclei and the fraction of coherent processes depends on the target. Secondly, only scarce data is available for hydrogen at the same kinematics as for the coherent tail of the nuclear targets at very low momentum transfer $|t_c|$.

The final data taking period of HERMES will be dedicated to the study of exclusive reactions like DVCS. A dedicated Recoil Detector, surrounding the target area and thus allowing to detect recoiling nucleons which are outside the acceptance of the main HERMES spectrometer, was proposed therefore. By detecting the recoiling nucleon, thus reconstructing the complete final state, the exclusivity of the reaction taking place can be ensured directly. Furthermore, the Recoil Detector will enhance the resolution of t_c and enabling access to the very low t_c-region also for a hydrogen target.

Design and construction of a Scintillating Fibre Tracker (SFT) for the HERMES Recoil Detector constitute the central part of this thesis. The SFT has to provide momentum reconstruction in an intermediate momentum regime (250 – 1400 MeV/c) and Particle IDentification (PID) for protons and charged pions below 650 MeV/c. The requirements for achieving these aims are presented and a corresponding design is developed, taking into account the limited space available in the target area of HERMES and the environmental conditions, e.g. magnetic fields.

Among the design goals was the ambitious task to build the SFT as a self-supporting structure in order to minimise the material budget introduced in the particle path, thus reducing the deterioration of momentum reconstruction due to multiple scattering. Suitable adhesives had to be found, on the one hand not corroding the fibre cladding and on the other hand yielding sufficient stability. A modular assembly was chosen for production reliability reasons. The whole assembly chain was successfully tested with dummy modules with respect to applicability and precision.

A test experiment at a secondary beam line, delivering protons and charged pions, was conducted with prototype modules to study the basic characteristics of the chosen design. Sophisticated software algorithms to accommodate optical crosstalk within the set-up were developed and their results are checked by Monte Carlo (MC) simulations. Furthermore, the energy response for protons and charged pions, being important for PID, was extracted and compared to MC simulations as well. Eventually, the spatial resolution of two prototype modules was studied. Concluding the results from the test experiment, the chosen SFT design successfully met all imposed requirements.

Finally, the completed SFT was surveyed in a dedicated test experiment at DESY Hamburg. The deviation of individual fibres was found to be less than $150\,\mu m$ which will be taken into account in tracking algorithms to achieve optimal momentum reconstruction. The SFT was then integrated into the Recoil Detector set-up by using a dedicated installation tool to avoid damage of the detector during this procedure. The Recoil Detector is currently being commissioned and will improve the study of exclusive reactions in the final data taking period of HERMES.

Appendix A

Construction Drawings

A.1 Optical Readout

Construction Drawings

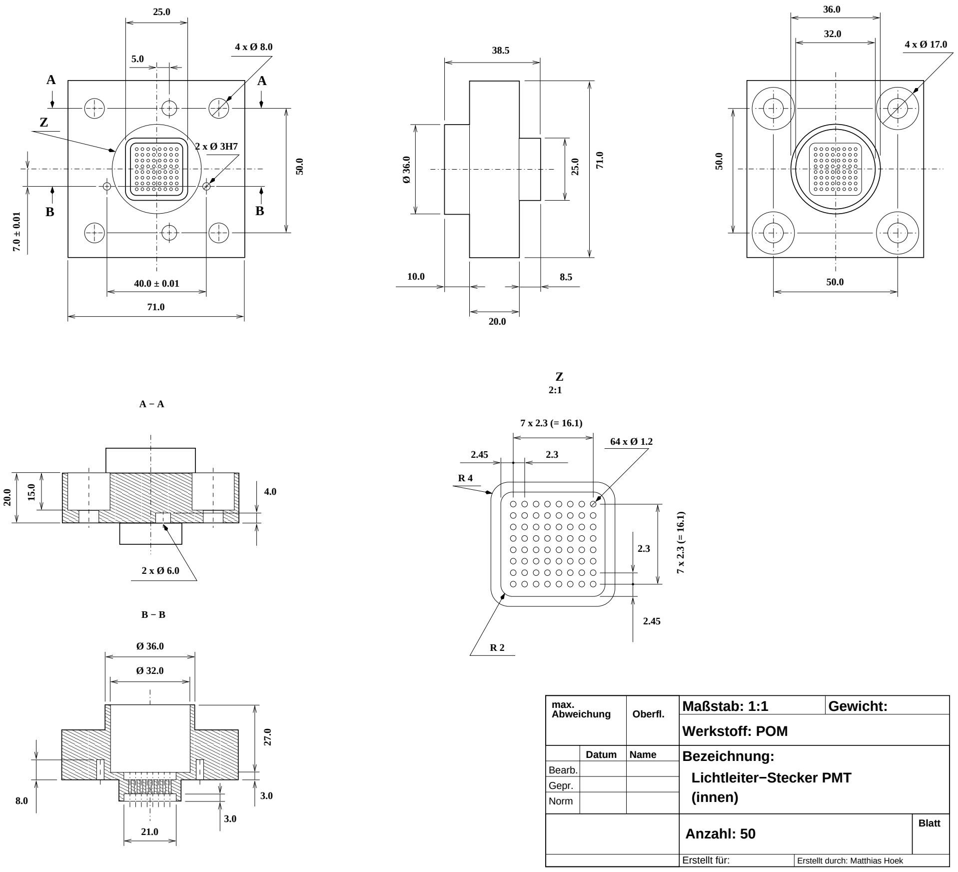

***Figure A.1:** Light Guide (LG) to MAPMT connector for inner type modules.*

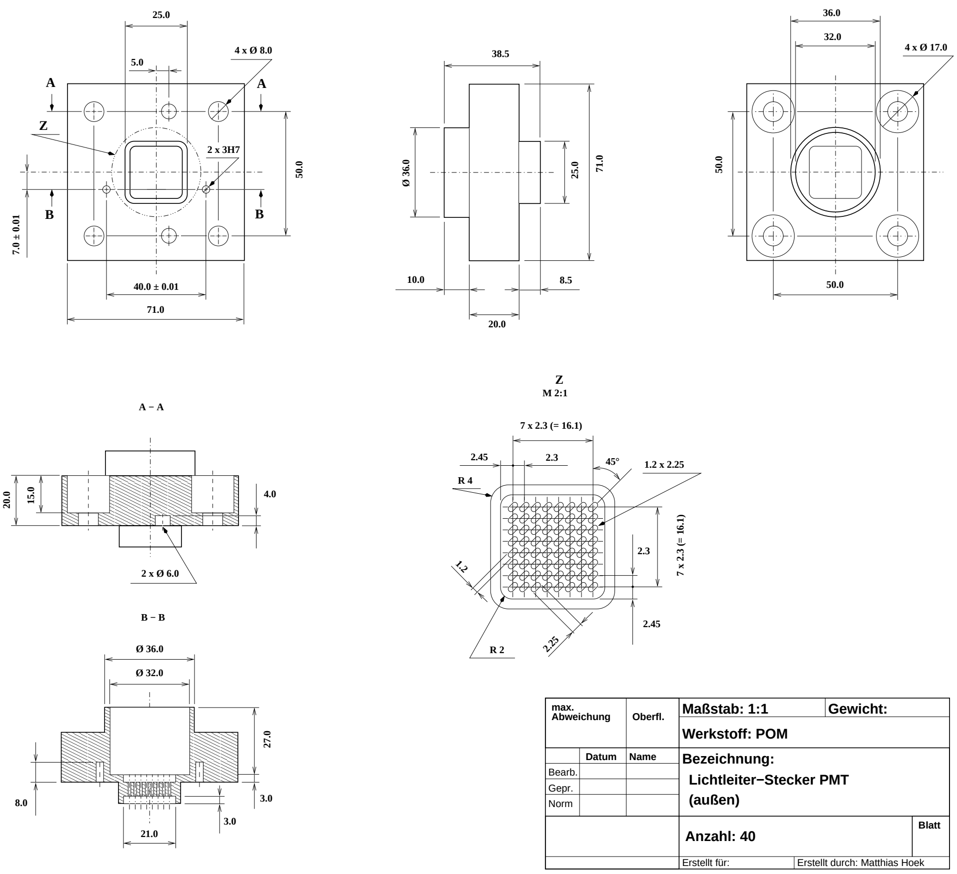

max. Abweichung
Oberfl.
Maßstab: 1:1
Gewicht:
Werkstoff: POM

	Datum	Name
Bearb.		
Gepr.		
Norm		

Bezeichnung:
Lichtleiter−Stecker PMT
(außen)

Anzahl: 40
Blatt

Erstellt für:
Erstellt durch: Matthias Hoek

Figure A.2: *Light Guide (LG) to MAPMT connector for outer type modules.*

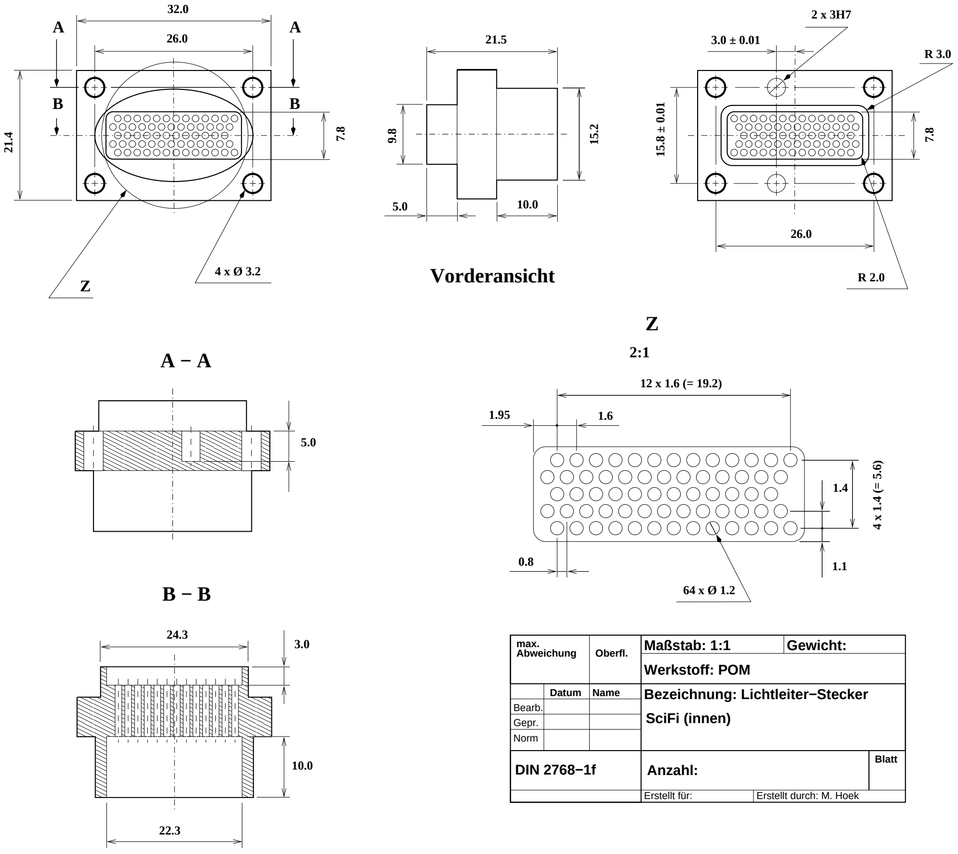

Figure A.3: *Light Guide (LG) to SFT connector for inner type modules.*

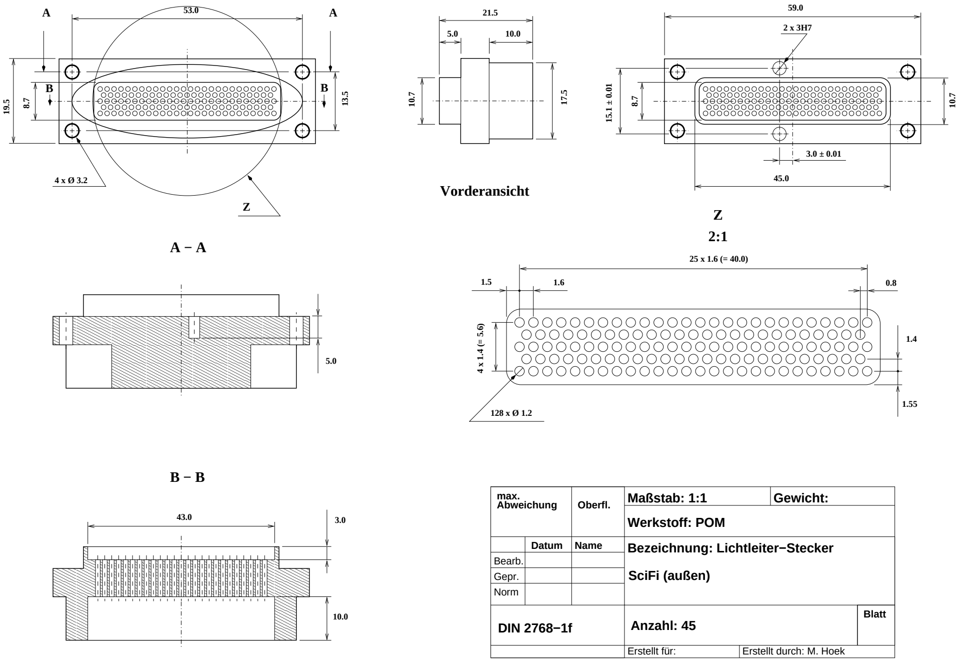

max. Abweichung
Oberfl.
Maßstab: 1:1
Gewicht:
Werkstoff: POM
Datum
Name
Bezeichnung: Lichtleiter−Stecker
SciFi (außen)
Bearb.
Gepr.
Norm
DIN 2768−1f
Anzahl: 45
Blatt
Erstellt für:
Erstellt durch: M. Hoek

Figure A.4: *Light Guide (LG) to SFT connector for outer type modules.*

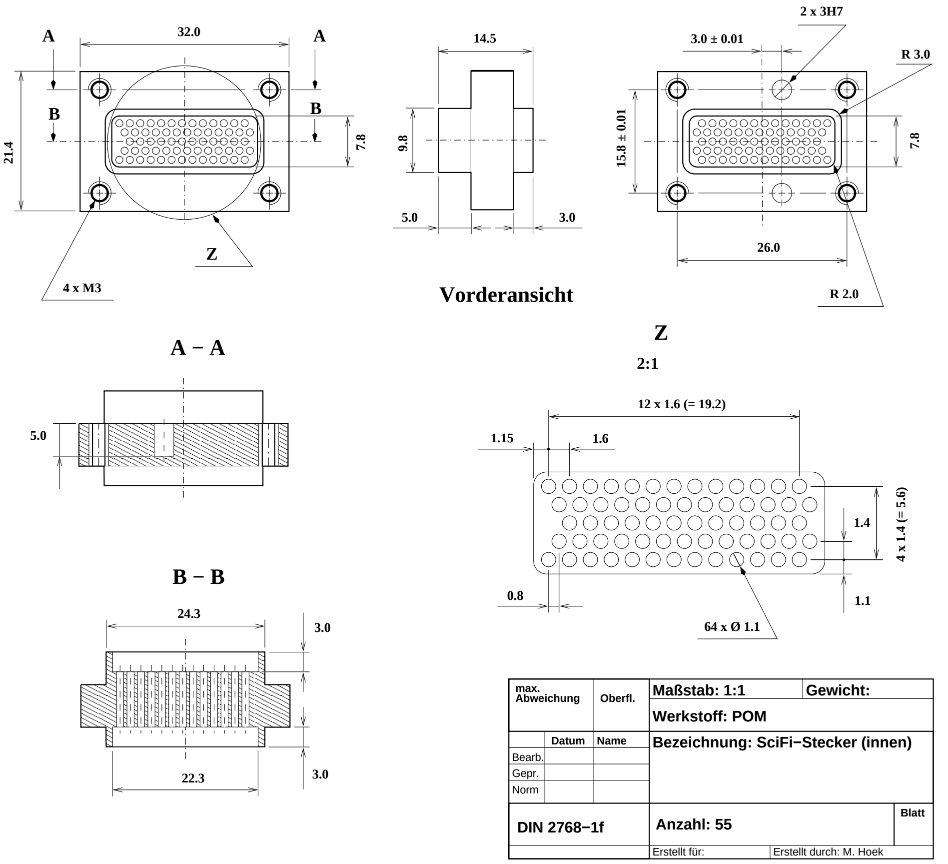

max. Abweichung	Oberfl.	Maßstab: 1:1	Gewicht:
		Werkstoff: POM	
	Datum	Name	Bezeichnung: SciFi−Stecker (innen)
Bearb.			
Gepr.			
Norm			
DIN 2768−1f		Anzahl: 55	Blatt
		Erstellt für:	Erstellt durch: M. Hoek

Figure A.5: *SFT module connector for inner type modules.*

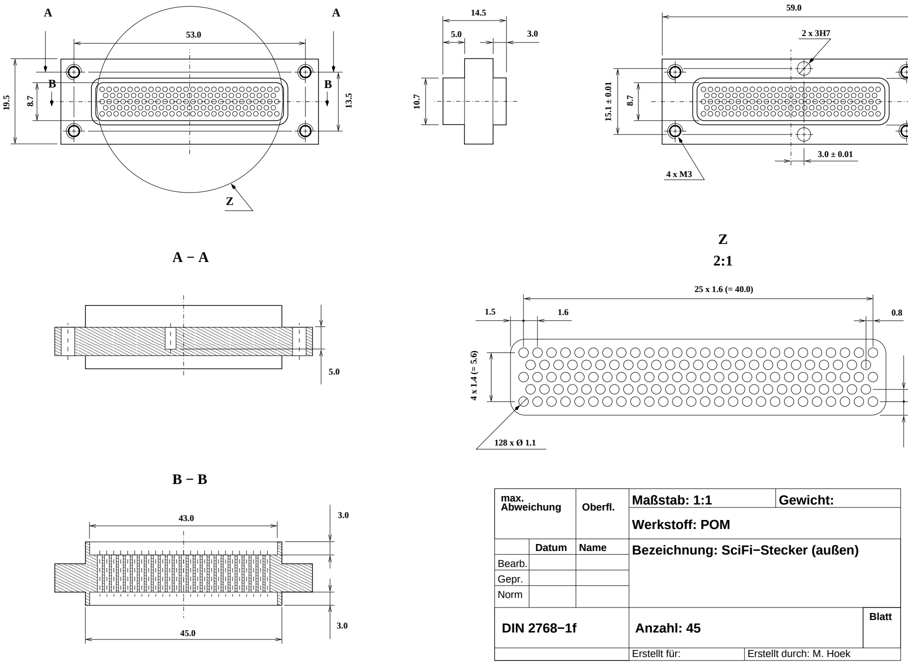

max. Abweichung	Oberfl.	Maßstab: 1:1	Gewicht:
		Werkstoff: POM	
	Datum	Name	Bezeichnung: SciFi−Stecker (außen)
Bearb.			
Gepr.			
Norm			
DIN 2768−1f		Anzahl: 45	Blatt
		Erstellt für:	Erstellt durch: M. Hoek

Figure A.6: *SFT module connector for outer type modules.*

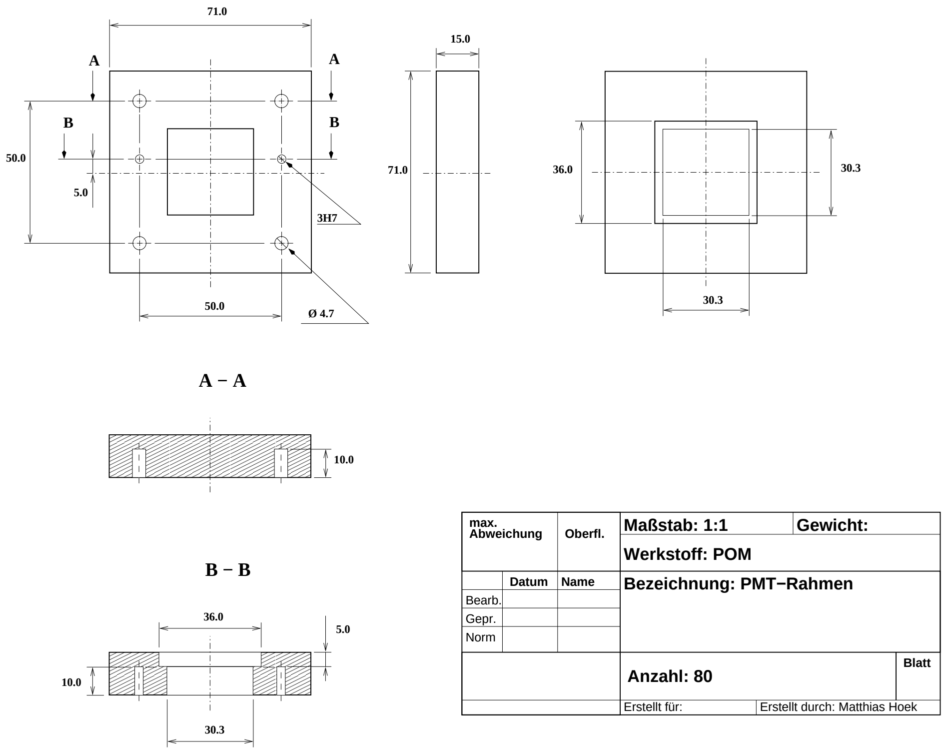

max. Abweichung	Oberfl.	Maßstab: 1:1	Gewicht:
		Werkstoff: POM	
	Datum	Name	Bezeichnung: PMT−Rahmen
Bearb.			
Gepr.			
Norm			
		Anzahl: 80	Blatt
		Erstellt für:	Erstellt durch: Matthias Hoek

Figure A.7: *MAPMT frame with precision alignment pins.*

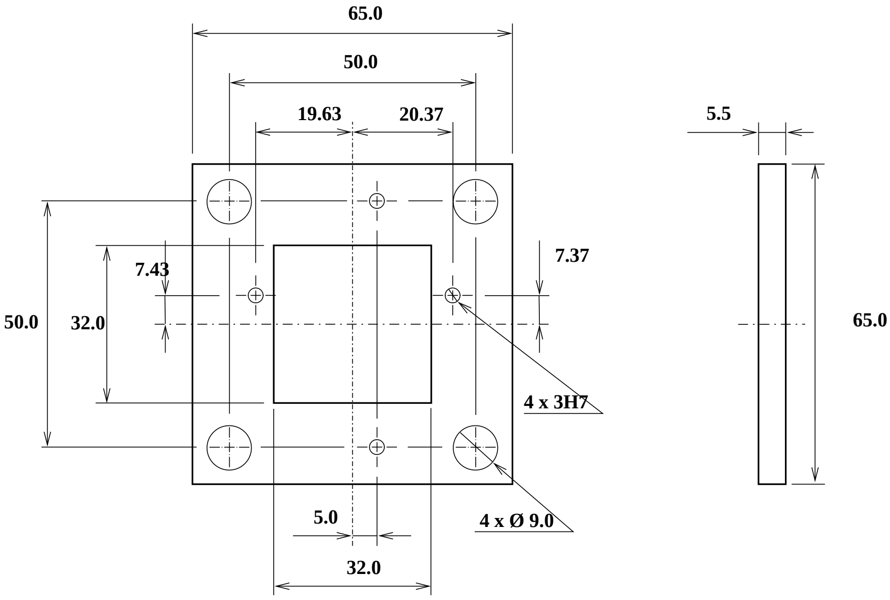

max. Abweichung		Oberfl.	Maßstab: 1:1	Gewicht:
			Werkstoff: Messing	
	Datum	Name	Bezeichnung: PMT−Adapter (PMT 2)	
Bearb.				
Gepr.				
Norm				
			Anzahl: 1	Blatt
			Erstellt für:	Erstellt durch: M. Hoek

Figure A.8: *Brass plate for aligning the Light Guide (LG) connector with respect to the MAPMT cathode.*

Mapping Schemes

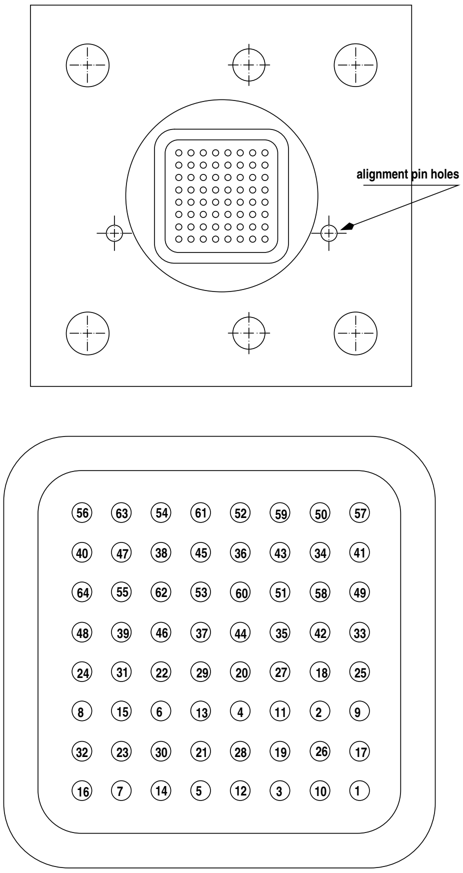

56	63	54	61	52	59	50	57
40	47	38	45	36	43	34	41
64	55	62	53	60	51	58	49
48	39	46	37	44	35	42	33
24	31	22	29	20	27	18	25
8	15	6	13	4	11	2	9
32	23	30	21	28	19	26	17
16	7	14	5	12	3	10	1

Figure A.9: *Mapping scheme for inner type Light Guide (LG) to MAPMT connector.*

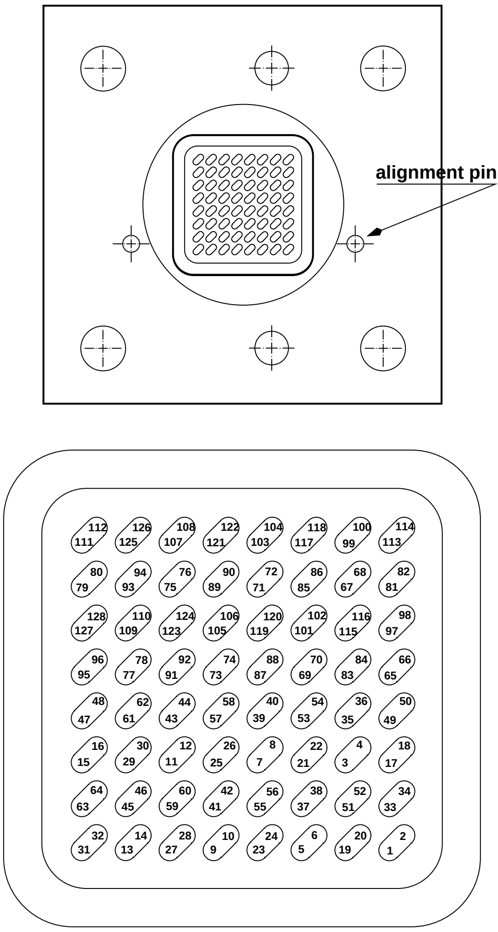

Figure A.10: *Mapping scheme for outer type Light Guide (LG) to MAPMT connector.*

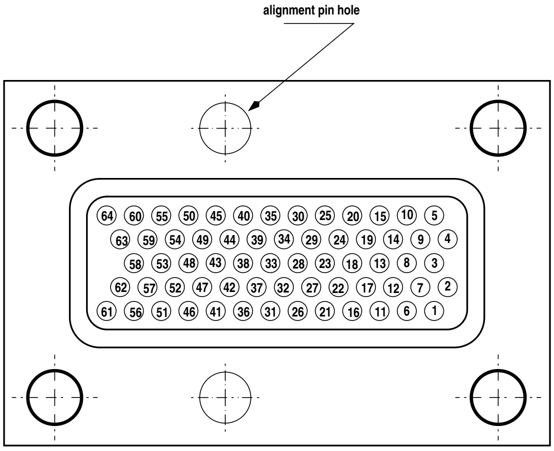

Figure A.11: *Mapping scheme for inner type Light Guide (LG) to SFT connector.*

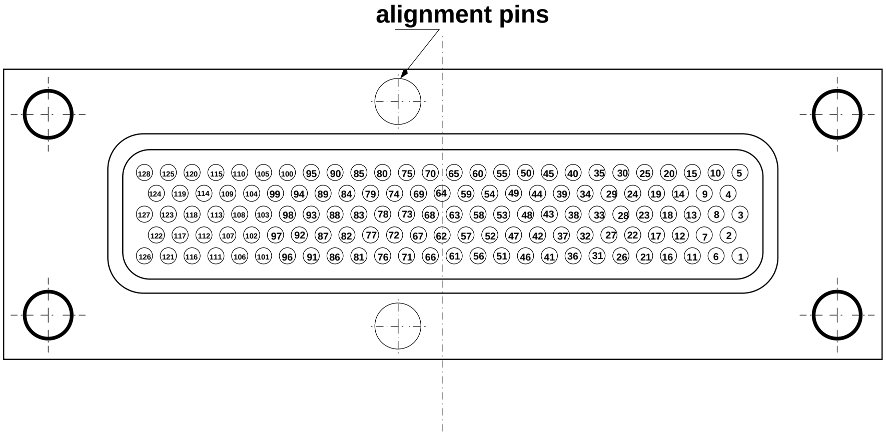

Figure A.12: *Mapping scheme for outer type Light Guide (LG) to SFT connector.*

A.2 Recoil Setup

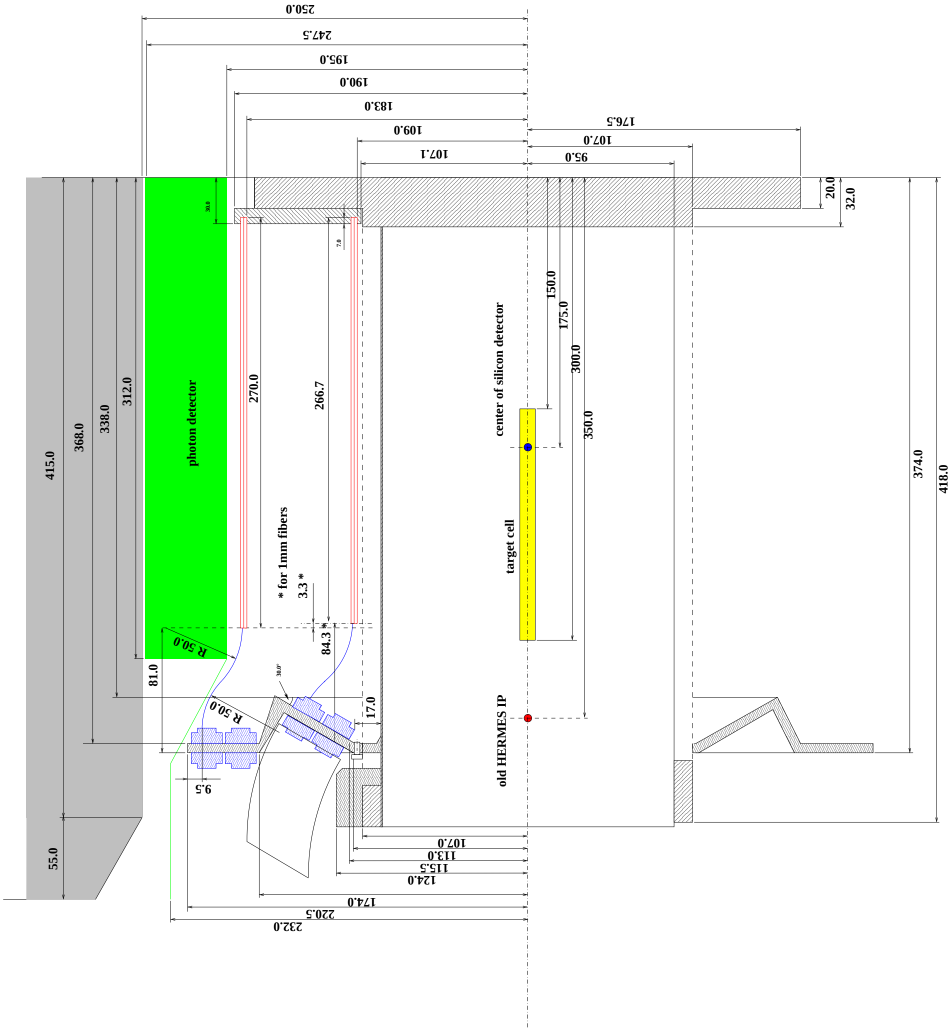

Figure A.13: *Recoil Detector assembly side view.*

Appendix B

Test Experiment Analysis

B.1 Efficiency Analysis

Pion Efficiencies

Table B.1: *Detection efficiency* ϵ_{SFT}^{pion} *of all SFT prototype modules for charged pions. The central pion momentum is varied in four discrete steps between* 300 – 900 *MeV/c. The threshold applied in the analysis is increased from* 0.5 *p.e. to* 1.5 *p.e. in* 0.5 *p.e.-steps.*

threshold (p.e.)	momentum (MeV/c)	SFT module	efficiency ϵ_{SFT}^{pion}
0.5	300	1	0.9986 ± 0.0004
		2	0.9832 ± 0.0010
		3	0.9833 ± 0.0010
		4	0.9872 ± 0.0009
	450	1	0.9981 ± 0.0004
		2	0.9832 ± 0.0012
		3	0.9867 ± 0.0011
		4	0.9894 ± 0.0010
	600	1	0.9979 ± 0.0008
		2	0.9837 ± 0.0022
		3	0.9860 ± 0.0020
		4	0.9953 ± 0.0012
	900	1	0.9991 ± 0.0009
		2	0.9462 ± 0.0065
		3	0.9392 ± 0.0069
		4	0.9956 ± 0.0019
1.0	300	1	0.9957 ± 0.0005
		2	0.9697 ± 0.0014
		3	0.9699 ± 0.0014

threshold (p.e.)	momentum (MeV/c)	SFT module	efficiency ϵ_{SFT}^{pion}
1.0	300	4	0.9718 ± 0.0013
	450	1	0.9945 ± 0.0007
		2	0.9690 ± 0.0017
		3	0.9739 ± 0.0015
		4	0.9755 ± 0.0015
	600	1	0.9917 ± 0.0016
		2	0.9687 ± 0.0030
		3	0.9710 ± 0.0029
		4	0.9838 ± 0.0022
	900	1	0.9933 ± 0.0025
		2	0.9140 ± 0.0083
		3	0.9108 ± 0.0085
		4	0.9699 ± 0.0052
1.5	300	1	0.9872 ± 0.0010
		2	0.9419 ± 0.0020
		3	0.9455 ± 0.0019
		4	0.9461 ± 0.0019
	450	1	0.9852 ± 0.0012
		2	0.9422 ± 0.0023
		3	0.9542 ± 0.0021
		4	0.9520 ± 0.0021
	600	1	0.9842 ± 0.0023
		2	0.9414 ± 0.0042
		3	0.9430 ± 0.0042
		4	0.9550 ± 0.0037
	900	1	0.9853 ± 0.0039
		2	0.8909 ± 0.0096
		3	0.8976 ± 0.0094
		4	0.9380 ± 0.0076

Proton Efficiencies

Table B.3: *Detection efficiency* ϵ_{SFT}^{proton} *of all SFT prototype modules for protons. The central proton momentum is varied in four discrete steps between* $450-900$ *MeV/c. The threshold applied in the analysis is increased from* 0.5 *p.e. to* 1.5 *p.e. in* 0.5 *p.e.-steps.*

threshold (p.e.)	momentum (MeV/c)	SFT module	efficiency ϵ_{SFT}^{proton}
0.5	450	1	0.9996 ± 0.0003
		2	0.9962 ± 0.0009
		3	0.9986 ± 0.0006
		4	0.9934 ± 0.0012

threshold (p.e.)	momentum (MeV/c)	SFT module	efficiency ϵ_{SFT}^{proton}
0.5	600	1	0.9997 ± 0.0001
		2	0.9941 ± 0.0005
		3	0.9975 ± 0.0003
		4	1.0000 ± 0.0000
	900	1	0.9997 ± 0.0001
		2	0.9804 ± 0.0010
		3	0.9849 ± 0.0009
		4	0.9958 ± 0.0005
1.0	450	1	0.9995 ± 0.0003
		2	0.9908 ± 0.0015
		3	0.9943 ± 0.0012
		4	0.9920 ± 0.0014
	600	1	0.9997 ± 0.0001
		2	0.9900 ± 0.0007
		3	0.9929 ± 0.0006
		4	0.9999 ± 0.0001
	900	1	0.9997 ± 0.0001
		2	0.9756 ± 0.0011
		3	0.9797 ± 0.0010
		4	0.9947 ± 0.0005
1.5	450	1	0.9995 ± 0.0003
		2	0.9839 ± 0.0019
		3	0.9914 ± 0.0014
		4	0.9909 ± 0.0015
	600	1	0.9996 ± 0.0001
		2	0.9850 ± 0.0008
		3	0.9880 ± 0.0008
		4	0.9999 ± 0.0000
	900	1	0.9989 ± 0.0002
		2	0.9634 ± 0.0014
		3	0.9700 ± 0.0013
		4	0.9914 ± 0.0007

B.2 Tracklet Contamination

Pions

Table B.5: *Tracklet contamination of all SFT prototype modules for charged pions. The central pion momentum is varied in four discrete steps between* 300 – 900 *MeV/c. The threshold applied in the analysis is increased from* 0.5 *p.e. to* 1.5 *p.e. in* 0.5 *p.e.-steps. The fraction of events with 1, 2 and more than 2 reconstructed tracklets per module is given as well as the maximum number of reconstructed tracklets per module.*

SFT module	momentum (MeV/c)	no of tracklets 1	2	>2	max. no of tracklets
1	300	0.886	0.106	0.008	5
	450	0.904	0.090	0.006	4
	600	0.886	0.107	0.008	5
	900	0.878	0.113	0.008	4
2	300	0.908	0.087	0.006	5
	450	0.917	0.078	0.005	5
	600	0.907	0.086	0.005	4
	900	0.926	0.070	0.004	4
3	300	0.897	0.095	0.007	4
	450	0.906	0.087	0.007	5
	600	0.904	0.090	0.006	4
	900	0.909	0.085	0.006	5
4	300	0.904	0.085	0.011	6
	450	0.844	0.136	0.019	6
	600	0.921	0.074	0.005	4
	900	0.919	0.073	0.008	5

Protons

Table B.7: *Tracklet contamination of all SFT prototype modules for protons. The central proton momentum is varied in four discrete steps between* 300 – 900 *MeV/c. The threshold applied in the analysis is increased from* 0.5 *p.e. to* 1.5 *p.e. in* 0.5 *p.e.-steps. The fraction of events with 1, 2 and more than 2 reconstructed tracklets per module is given as well as the maximum number of reconstructed tracklets per module.*

SFT module	momentum (MeV/c)	no of tracklets 1	2	>2	max. no of tracklets
1	300	0.480	0.342	0.178	6
	450	0.680	0.266	0.054	5
	600	0.785	0.192	0.023	5
	900	0.840	0.145	0.015	5

SFT module	momentum (MeV/c)	no of tracklets 1	2	>2	max. no of tracklets
2	300	0.576	0.328	0.096	4
	450	0.795	0.181	0.024	4
	600	0.837	0.150	0.013	5
	900	0.902	0.092	0.006	5
3	300	0.560	0.328	0.112	6
	450	0.764	0.206	0.031	5
	600	0.825	0.159	0.016	5
	900	0.888	0.104	0.008	5
4	300	0.671	0.263	0.065	5
	450	0.629	0.288	0.083	5
	600	0.868	0.122	0.009	6
	900	0.906	0.086	0.007	6

Appendix C

DVCS analysis

C.1 Systematic Errors

Table C.1: *Systematic error contributions to the* $\sin\phi$*-moment of the Beam-Spin Asymmetry (BSA).* $\delta_{miscalib.}$ *denotes contributions due to calorimeter miscalibration by 1%,* $\delta_{misalign}$ *contributions due to beam and spectrometer misalignment and* δ_{π° *contributions due to semi-inclusive* π°*background. Values for* $\delta_{miscalib.}$*,* $\delta_{misalign}$ *and the semi-inclusive background fraction* η *are obtained by Monte Carlo simulations.*

target	$-t_c$	η	$\delta_{miscalib.}$	$\delta_{misalign}$	δ_{π°
hydrogen	0.00 – 0.06	0.03	0.0007	0.0041	0.004
	0.06 – 0.14	0.057	0.0005	0.0047	0.017
	0.14 – 0.30	0.054	0.0019	0.0061	0.0086
	0.30 – 0.70	0.036	0.0053	0.0248	0.0062
deuterium	0.00 – 0.06	0.029	0.0003	0.0007	0.011
	0.06 – 0.14	0.062	0.0025	0.0155	0.039
	0.14 – 0.30	0.053	0.0023	0.0069	0.027
	0.30 – 0.70	0.042	0.0012	0.0087	0.012
helium	0.00 – 0.06	0.022	0.0006	0.0057	0.013
	0.06 – 0.14	0.058	0.0006	0.0028	0.026
	0.14 – 0.30	0.031	0.0092	0.0101	0.020
	0.30 – 0.70	0.030	0.0026	0.0063	0.012
nitrogen	0.00 – 0.06	0.009	0.0007	0.0046	0.0033
	0.06 – 0.14	0.123	0.0011	0.0063	0.060
	0.14 – 0.30	0.044	0.0028	0.0015	0.020
	0.30 – 0.70	0.057	0.0123	0.0784	0.043
neon	0.00 – 0.06	0.071	0.0007	0.0037	0.023
	0.06 – 0.14	0.11	0.0031	0.0223	0.042
	0.14 – 0.30	0.086	0.0017	0.0044	0.017

target	$-t_c$	η	$\delta_{miscalib.}$	$\delta_{misalign}$	δ_{π°
neon	0.30 – 0.70	0.047	0.0049	0.0279	0.017
krypton	0.00 – 0.06	0.082	0.0002	0.0012	0.039
	0.06 – 0.14	0.122	0.0027	0.0014	0.035
	0.14 – 0.30	0.092	0.0002	0.0016	0.021
	0.30 – 0.70	0.042	0.0051	0.0239	0.011
xenon	0.00 – 0.06	0.078	0.0026	0.0187	0.041
	0.06 – 0.14	0.123	0.0064	0.0002	0.038
	0.14 – 0.30	0.088	0.0104	0.0265	0.091
	0.30 – 0.70	0.025	0.0007	0.0181	0.0062

Bibliography

[1] A.A. Sokolov and I.M. Ternov, Sov. Phys. Doklady **8** (1964) 1203.

[2] K. Rith, *Spin Asymmetries in Deep-Inelastic Electron-Nucleon Scattering – Selected* HERMES *Results*, Prog. Part. Nucl. Physics **49** (2002) 245–324.

[3] M. Beckmann *et al.*, *The Longitudinal Polarimeter at HERA*, Nucl. Instrum. Meth. A **479** (2002) 334.

[4] D.P. Barber *et al.*, *High spin polarization at the HERA electron storage ring*, Nucl. Instrum. Meth. A **338** (1994) 166–184.

[5] K. Ackerstaff *et al.* [HERMES Collaboration], *The* HERMES *spectrometer*, Nucl. Instrum. Meth. A **417** (1998) 230 [arXiv:hep-ex/9806008].

[6] A. Nass et al., *The* HERMES *Polarized Atomic Beam Source*, Nucl. Instrum. Meth. A **505** (2003) 633.

[7] C. Baumgarten *et al.*, *An atomic beam polarimeter to measure the nuclear polarization in the* HERMES *gaseous polarized hydrogen and deuterium target*, Nucl. Instrum. Meth. A **482** (2002) 606.

[8] C. Baumgarten *et al.*, *A Gas Analyzer for the Internal Polarized Target of the* HERMES *Experiment at HERA*, Nucl. Instrum. Meth. A **508** (2003) 265.

[9] W. Wander, *Rekonstruktion hochenergetischer Streuereignisse im* HERMES-*Experiment*, Ph.D. thesis, Universität Nürnberg-Erlangen, 1996.

[10] F. Ellinghaus, *Beam-Charge and Beam-Spin Azimuthal Asymmetries in Deeply-Virtual Compton Scattering*, Ph.D. thesis, Humboldt-Universität Berlin, 2004 .

[11] N. Akopov *et al.*, *The* HERMES *Dual-Radiator Ring Imaging Čerenkov Detector*, Nucl. Instrum. Meth. A **479** (2002) 511.

[12] R.K. Bock and A. Vasilescu, *The Particle Detector BriefBook*, Springer-Verlag Berlin Heidelberg New York, 1998.

[13] H. Avakian *et al.*, *Performance of F101 radiation resistant lead glass shower counters*, Nucl. Instrum. Meth. A **378** (1996) 155–161.

[14] H. Avakian et al., *Performance of the electromagnetic calorimeter of the* HERMES *experiment*, Nucl. Instrum. Meth. A **417** (1998) 69–78.

[15] J. Ely, *Measurement of the single spin azimuthal asymmetry in the predominantly exclusive electroproduction of photons from the proton*, Ph.D. thesis, University of Colorado, 2002.

[16] A. Airapetian *et al.* [HERMES Collaboration], *Measurement of the beam spin azimuthal asymmetry associated with deeply-virtual Compton scattering*, Phys. Rev. Lett. **87** (2001) 182001 [arXiv:hep-ex/0106068].

[17] The HERMES Collaboration, *The* HERMES *Recoil Detector Technical Design Report*, HERMES Internal Note 02-003, 2002.

[18] B. Seitz, *The* HERMES *recoil detector: a combined silicon strip and scintillating fibre detector for tracking and particle identification*, Nucl. Instrum. Meth. A **535** (2004) 538–541.

[19] J.J.M. Steijger, *The* HERMES *silicon project*, Nucl. Instrum. Meth. A **447** (2000), 55–60.

[20] J.J.M. Steijger, *First experience with the* HERMES *silicon detector*, Nucl. Instrum. Meth. A **461** (2001), 247–259.

[21] A. Kastenmüller *et al.*, *Fast detector readout for the HADES-RICH*, Nucl. Instrum. Meth. A **433** (1999) 438–443.

[22] private comunications, G.P. Capitani, INFN Frascati.

[23] R.E. Ansorage *et al.*, *Performance of a scintillating fibre detector for the UA2 upgrade*, Nucl. Instrum. Meth. A **265** (1988) 33.

[24] G. Wilquet *et al.*, *The CHORUS scintillating fiber tracker and opto-electronic readout system*, Nucl. Instrum. Meth. A **412** (1998) 19–37.

[25] E.R. Ramberg, *Scintillating Fiber Ribbon Development for the DØ Upgrade*, Proceedings SCIFI 97, edited by Alan D. Bross, Randal C. Ruchti, Mitchell R. Wayne, Woodbury, N.Y., American Inst. Phys., 1998 (AIP Conference Proceedings, Vol. 450).

[26] C. Grupen, *Teilchendetektoren*, BI Wissenschaftsverlag, Mannheim, Leipzig, Wien, Zürich, 1993.

[27] J.C. Cooper, *Construction and Mechanical Qualification of Scintillating Fiber Doublet Ribbons*, Proceedings SCIFI 93, edited by A.D. Bross, R.C. Ruchti, M.R. Wayne. River Edge, N.J., World Scientific, 1995.

[28] W. R. Leo, *Techniques for Nuclear and Particle Physics Experiments*, Second Revised Edition, Springer-Verlag, 1994.

[29] S. Eidelman *et al.*, *Review of Particle Physics*, Phys. Lett. B **592** (2004) 1.

[30] Ph. Rebourgeard *et al.*, *Fabrication and measurements of plastic scintillating fibers*, Nucl. Instrum. Meth. A **427** (1999) 543–567.

[31] Catalogue, Kuraray.

[32] F. Hinterberger *et al.*, *A helical scintillating fiber hodoscope*, Nucl. Instrum. Meth. A **431** (1999) 428–436.

[33] H. Leutz, *Scintillating fibres*, Nucl. Instrum. Meth. A **364** (1995) 422–448.

[34] C.M. Hawkes *et al.*, *Decay time and light yield measurements for plastic scintillating fibers*, Nucl. Instrum. Meth. A **292** (1990) 329–336.

[35] D. Meschede, *Gerthsen Physik*, 21. Auflage, Springer Verlag, Berlin Heidelberg New York, 2002.

[36] E.C. Aschenauer *et al.*, *Development of scintillating fiber detector technology for high rate particle tracking*, arXiv:hep-ex/970001, 1997.

[37] C.D'Ambrosio *et al.*, *Photon Counting with a hybrid photomultiplier tube (HPMT)*, Nucl. Instrum. Meth. A **338** (1994) 389–397.

[38] M. Chung *et al.*, *Effects Of Light On Scintillating Fibers Containing 3-Hydroxyflavone*, Proceedings SCIFI 93, edited by A.D. Bross, R.C. Ruchti, M.R. Wayne. River Edge, N.J., World Scientific, 1995.

[39] private communications, Kuraray.

[40] Y. Yoshizawa *et al.*, *The Development and the Study of R5900-00-M64 for Scintillating / Optical Fiber Read Out*, IEEE Transactions on Nuclear Science, Vol **48**, No. 1, 1998, 877 – 881.

[41] Multi-anode Photomultiplier Tube Assembly H7546 data sheet, Hamamatsu, Sept. 2000.

[42] L. Rubáček, *Search for the Pentaquark States in Lepton-Nucleon Scattering at* HERMES, Ph.D. thesis, Universität Gießen, April 2006.

[43] private communications, Hamamatsu Germany.

[44] M. Chung *et al.*, *Study of Light Transmission Through Optical Fiber-to-Fiber Connector Assemblies*, Proceedings SCIFI 97, edited by Alan D. Bross, Randal C. Ruchti, Mitchell R. Wayne, Woodbury, N.Y., American Inst. Phys., 1998 (AIP Conference Proceedings, Vol. 450).

[45] M. Chung *et al.*, *Development of a Multichannel Fiber-To-Fiber Optical Connector for the DØ Upgrade Tracker*, IEEE Transactions on Nuclear Science, Vol **43**, No. 3, 1996, 1153–1156.

[46] N.A. Amos *et al.*, *Optical attenuation length measurement of scintillating fibers*, Nucl. Instrum. Meth. A **297** (1990) 396–403.

[47] J. Streit-Lehmann, *Entwicklung und Bau einer Lichtquelle für das Gain Monotoring System eines* HERMES*-Detektors aus szintillierenden Fasern*, Diploma Thesis, Universität Gießen, March 2006.

[48] R. Nahnhauer *et al.*, *Testrun results from prototype detectors for high rate particle tracking*, Nucl. Instrum. Meth. A **424** (1999) 459–469.

[49] K. Hara *et al.*, *Radiation hardness and mechanical durability of Kuraray optical fibers*, Nucl. Instrum. Meth. A **411** (1998) 31–40.

[50] K. Hara *et al.*, *Development of fiber-to-fiber connectors for scintillating tile/fiber calorimeters*, Nucl. Instrum. Meth. A **357** (1995) 71–77.

[51] private communications, H. Sommer, Siemens-VDO.

[52] private communications, R. Nahnhauer, DESY Zeuthen.

[53] private communications, J. Hauschildt, DESY Hamburg.

[54] C. Caccamise *et al.*, *Instructions for making fiber ribbons for the D-Zero detector upgrade*, D-Zero Note #1532, 1992.

[55] private communications, R. Perez, Universität Gießen.

[56] R. Perez *et al.*, Alignment of the SciFi Detector at the DESY22 electron test-beam, not published.

[57] J. Diaz *et al.*, *Design and commissioning of the GSI pion beam*, Nucl. Instrum. Meth. A **478** (2002) 511–526.

[58] private communications, S. Lu, Universität Gießen.

[59] I. Chirikov-Zorin *et al.*, *Method for precise analysis of metal package photomultiplier single photoelectron spectra*, Nucl. Instrum. Meth. A **456** (2001) 310–324.

[60] private communications, M. Hartig, Universität Gießen.

[61] private communications, L. Rubáček, Universität Gießen.

[62] W. Sommer, *Identifikation von Pionen und Protonen mit einem Detektor aus szintillierenden Fasern*, Diploma Thesis, Universität Gießen, 2003.

[63] M. Hoek, *Assembly of Lightguides for the* HERMES *Recoil Detector*, January 2004, not published.

[64] M. Hoek *et al.*, *Performance of the Recoil Scintillating Fibre Tracker in a Test Beam at GSI*, HERMES Internal Note 05-013, 2005.

[65] M.J. Berger, J.S. Coursey, M.A. Zucker, *ESTAR, PSTAR and ASTAR: Computer Programs for Calculating Stopping-Power and Range Tables for Electrons, Protons, and Helium Ions (version 1.2.2) (2000).* [Online] Available: http://physics.nist.gov/Star [2004, November 2]. National Institute of Standards and Technology, Gaithersburg, MD.

[66] M. Hartig, *A charge injection system for PFM readout tests*, August 2004, not published.

[67] GSI test beam logbook, pp. 73, 2003.

[68] GEANT3.21 Detector Description and Simulation Tool, CERN Program Library Long Writeup W5013, Geneva 1993.

[69] L. De Nardo, *On the Propagation of Statistical Errors*, HERMES Internal Note 02-008, 2002.

[70] D. Müller *et al.*, *Wave Functions, Evolution Equations and Evolution Kernels from Light-Ray Operators of QCD*, Fortschr. Phys. **42**, 101 (1994).

[71] X. Ji, *Gauge-Invariant Decomposition of Nucleon Spin*, Phys. Rev. Lett. **78**, 610 (1997).

[72] R.L. Jaffe, *Spin, Twist and Hadron Structure in Deep Inelastic Processes*, arXiv:hep-ph/9602236, 1996.

[73] M. Diehl, *Generalized Parton Distributions*, Habilitation Thesis, DESY Hamburg, 2003 [arXiv:hep-ph/0307382].

[74] X. Ji, *Deeply virtual Compton scattering*, Phys. Rev D **55** (1997) 7114.

[75] A. Belitsky *et al.*, *Theory of deeply virtual Compton scattering on the nucleon*, Nucl. Phys. B **629**, 323 (2002).

[76] V.A. Korotkov *et al.*, *Future measurements of deeply virtual Compton scattering*, Eur. Phys. J. C **23** (2002) 455.

[77] M. Diehl *et al.*, *Testing the handbag contribution to exclusive virtual Compton scattering*, arXiv:hep-ph/9706344, 1997.

[78] A. Airapetian *et al.* [HERMES Collaboration], *The Beam-Charge Azimuthal Asymmetry and Deeply Virtual Compton Scattering*, arXiv:hep-ex/0605108, submitted to Phys. Rev. Lett.

[79] M. Polyakov, *Generalized parton distributions and strong forces inside nucleons and nuclei*, Phys. Lett. B **555**, 57–62 (2003).

[80] A. Kirchner and D. Müller, *Deeply virtual Compton scattering off nuclei*, Eur. Phys. J. C **32** (2004) 347–375.

[81] A. Freund and M. Strikman, *DVCS on nuclei: Observability and Consequences*, arXiv:hep-ph/0309065, 2003.

[82] V. Guzey and M. Strikman, *DVCS on spinless nuclear targets in impulse approximation*, arXiv:hep-ph/0301216, 2003.

[83] M. Diehl, *Exploring skewed parton distributions with polarized targets*, arXiv:hep-ph/0010200, 2000.

[84] A. Airapetian *et al.* [HERMES Collaboration], *Single-spin azimuthal asymmetry in exclusive electroproduction of* π^+ *mesons*, Phys. Lett. B **535** (2002) 85.

[85] R. Shanidze [HERMES Collaboration], *Exclusive Vector Meson Production and DVCS at* HERMES, Eur. Phys. J. C **33** (2004) 503 – 505.

[86] S. Haan, *Deeply Virtual Compton Scattering on Neon*, Diploma Thesis, Universität Leipzig, 2005.

[87] B. Krauss *et al.*, *Beam Charge Asymmetry from Deeply Virtual Compton Scattering on the Deuteron*, HERMES Release Report, June 2004.

[88] B. Krauss, *Deeply Virtual Compton Scattering and the* HERMES*-Recoil-Detector*, Ph.D. thesis, Universität Nürnberg-Erlangen, 2005.

[89] L. De Nardo, *Trigger Efficiencies For 98 And 99 Data*, HERMES Internal Note 01-005, 2001.

[90] DVCS group, *Longitudinal Target Spin Asymmetry from DVCS Process on Longitudinally Polarized Proton and Deuterium Targets*, HERMES Release Report, April 2005.

[91] H. Guler *et al.*, *Nuclear DVCS*, HERMES Release Report, July 2006.

[92] private communications, H. Guler, DESY Zeuthen.

[93] P. de Bievre and P.D.P. Taylor, Int. J. Mass Spectrom. Ion Phys. **123** (1993) 149.

[94] I. Mills, T. Cvitas, K. Homann, N. Kallay, and K. Kuchitsu, *Quantities, Units and Symbols in Physical Chemistry*, Blackwell Scientific Publications, Oxford, UK, 1988.

[95] P. Di Nezza, email communication on nuclear-list, 11. April 2005.

[96] V. Blobel, *Statistische und numerische Methoden der Datenanalyse*, Teubner Verlag, Stuttgart, Leipzig, 1998.

[97] MINUIT Minimization package Reference Manual Version 94.1, CERN Program Library Long Writeup D506, Geneva 1994.

List of Figures

List of Tables

Acknowledgements

This work would have been impossible without the support and contributions of many people.

In the first place, I would like to express my gratitude to my advisor Prof. Dr. Michael Düren for creating an interesting and stimulating atmosphere during my studies in his group.

I am also indebted to Björn Seitz for his advice and innumerable discussions concerning the Recoil Detector and this thesis. Not to mention Matthias Hartig who coordinated the test experiment at GSI and helped me get along with analysis of the SFT data. He also improved the morale in difficult times (Bier-Pulser).

I would like to thank all my colleagues in our group at the University of Gießen. Especially I want to thank Lukáš Rubáček, my friend and office mate for his invaluable support, introducing me into the world of Linux (Probably only few results would have been presented in this work otherwise) and improving the beer culture of our office. To my shame I have to admit that the only Czech word I learned in this period is ”na zdraví”.

I would also like to express my thanks to the secretaries of our institute, Marianne Brunotte and Anita Rühl who both helped me in my struggles with the university's administrations. Moreover, I am much obliged to Rainer Novotny, Werner Döring and Jürgen Schneider for discussing physics and computer issues even if their time was scarce. Without the people of our mechanical workshop not even the slightest piece of detector hardware would have been possible. I am therefore much obliged to Rainer Weiss and Rolf Engel and the team of the workshop for trying to realise my constructions and doing so in time.

Thanks also to the members of the HERMES collaboration. It was an enlightening and valuable experience to participate in an international collaboration and do physics. Special thanks to Hayg Guler who was my source of wisdom for the details of the DVCS analysis. Rolf Nahnhauer and his colleagues from DESY Zeuthen, who introduced me into the secrets of fibre detector technology.

To Morgan Murray I am specially indebted for proof-reading my thesis and trying to make reading this thesis a next-to-pleasing activity.

There was, of course, more than only physics in this period for which I am very glad. I would like to thank Jörg Jacobi and Daniel Pfisterer with whom I share the fate of having studied physics and decided to run for a Ph.D. I would like to thank Björn and Julia and their families, because they became more than just colleagues.

Finally, I want to express my gratitude to my family which supported me throughout my studies and with whom I shared many pleasures and also some strokes.

Last but not least, I want to thank Kerstin, who was not only girlfriend and fiancee but is now my wife. She also endured the typical spleens of physicists which did not scare her off and was always a great help in hard times. Thanks for your patience and love!